EMA 569 - Refueling Spacecraft

Aidan Butula, Will Driessen, Jack Hilt, Nikolaj Hindsbo, Scott Nelson

May 1, 2023

Executive Summary

The goal of SpacExxon is to create a spacecraft that supplies satellites in low-earth orbit with hydrazine fuel to extend their missions and help prevent collisions and space debris. A 1000 kilogram propellant mass will be the target deliverable such that a single launch can refuel ten satellites with 100 kilograms of hydrazine propellant. The spacecraft will utilize the SpaceX Starship launch vehicle to reach low-earth orbit. Research on comparable spacecraft and missions as well as standards and specifications was completed. Preliminary design specifications for the spacecraft were determined and then a mission profile was constructed.

Initial orbital mechanics calculations were conducted for the spacecraft to determine fuel requirements. This was done while choosing all of the subsystems and components of the spacecraft to get an approximate size and weight of the spacecraft. The orbital mechanics calculations include Hohmann transfer, plane change, and a test mission. The test mission consisted of a Hohmann transfer with an optimally split plane change and mass analysis. The subsystems of the spacecraft include propulsion, tank, guidance, navigation, and control, thermal systems, and power systems. It was then decided that the refueling apparatus would be a robotic arm with a Rapidly Attachable Fluid Transfer Interface (RAFTI) service valve by Orbit Fab.

A preliminary computer-aided design (CAD) was then created for the spacecraft's structure before performing structural and Finite Element Analysis (FEA) to assess the structural integrity of the design. The preliminary CAD provided an initial design that can be used to determine the general layout and geometry of the spacecraft. The preliminary CAD included the structure of the spacecraft, a custom-designed tank, solar panels, a propulsion system, a payload adapter, and other components. Structural analysis was then completed with FEA for launch accelerations, propulsion impulse, and random vibration. A plumbing schematic was also created, and calculations were completed for the thermodynamic states plumbing system.

From the preliminary CAD and structural analysis, the design needed to be iterated. A final iteration CAD was created based on the results of FEA. Final CAD also included components of the spacecraft that had not been modeled yet, and considered factors such as manufacturability, and the assembly of the spacecraft. Part numbers and drawings of various assemblies and parts of the final design were also created. Structural and orbital mechanics calculations were then iterated for the new design.

Although much work has been put into the design concept of SpacExxon to this point, there is much possibility for future work still to be completed for the project. Though this report attempts to describe the design of the components, subsystems, mission, and more, there is still heavy iteration and redesign to be completed in order to be confident in a mission proposal to a true launch provider such as SpaceX. Iteration for the subsystem design of the satellite would need to occur in parallel with the orbital calculations to get an accurate and reliable final design and mission profile.

Contents

List of Figures

List of Tables

Table of Variables

Variable	Description	Units
Δv	Change in Velocity	m/s
Δi	Change in Inclination Angle	rad
ΔP	Change in Pressure	Pa
I_{sp}	Specific Impulse	s
μ	Gravitational Constant (Earth)	m/s^2
r	Radial Distance	m
a	Semimajor Axis	m
v_c	Circular Velocity	m/s
v_p	Velocity at Perigee	m/s
v_a	Velocity at Apogee	m/s
α	Optimal Transfer Angle	rad
m	Mass	kg
g	Gravitational Acceleration	m/s^2
ρ	Density	kg/m^3
V	Volume	m^3
σ	Stress	Pa
σ_y	Yield Stress	Pa
σ_{max}	Maximum Stress	Pa
τ	Shear Stress	Pa
q	Radial Pressure	Pa
R	Radius of tank	m
t	Thickness of Tank Wall	m
$\omega_{x,y,z}$	Body Fixed Angular Velocities	deg/s
$I_{xx,yy,zz}$	Mass Moment of inertia	m
θ	Nutation Angle	deg
ψ	Precession Angle	deg
ϕ	Spin Angle	deg
$\beta_{0,1,2,3}$	Quaternions	-
H_f	Pressure Head Loss	Pa
Q	Volumetric Flow	m^3/s
SG	Specific Gravity Constant	-
C_v	Coefficient of Flow	-
hp	Horsepower	hp
T	Torque	N-m
T_f	Frictional Torque	lb-in
n	Shaft Speed	m/s
μ_f	Coefficient of Friction	-
F_r	Radial Bearing Load	lbs_f
d_{bb}	Bearing Bore	in

1 Mission Statement

Spacecraft have continually been designed with propulsion systems that require fuel for orbital transfers, attitude adjustments, and mission upkeep. These spacecraft, such as satellites, probes, and cargo vehicles, are often created as singular missions that do not have a sustainable way to refuel the spacecraft and extend the length of the mission. Without spacecraft refueling, missions often end in an atmospheric blaze. SpacExxon proposes a spacecraft that supplies satellites in low-earth orbit with hydrazine to extend their mission, providing extended value to companies utilizing the fuel provided by our company's product.

1.1 Problem Significance

As of May 2022, there were a total of 5,465 operating satellites [1]. That number alone may seem large, but estimates indicate that there may be more than 100,000 satellites in orbit by 2030 [1]. More satellites in orbit pose worries of collision and the constant cost of sending up satellites into space are often cited. Additionally, chemicals released from satellites burning in the atmosphere could damage the ozone layer. For perspective, it is estimated that the death of the first generation of 3,500 SpaceX Starlink satellites will cause 2.2 tons of satellites to deorbit daily - and there are over 40,000 Starlink satellites planned in the future [2] [3]. This is compared to 60 tons of meteorite materials coming into Earth every day. However, meteorites are mostly made of oxygen, magnesium, and silicon - which does not pose a problem to the ozone layer. However, satellites are mostly aluminum, which will chemically react with ozone to form aluminum oxide and could slowly deplete the supply of ozone in the atmosphere [2].

In Low Earth Orbit (LEO), the average lifespan of a satellite is only 7-10 years [4]. As a satellite runs out of fuel to run on, it uses the remainder of its fuel to slow down and launch itself into the atmosphere. Instead, if a satellite could be refueled, this could allow them to extend their mission lifetime - saving money and time. In late 2022, the United States Space Force (USSF) awarded Orbit Fab, an in-space refueling company, a $13.3 million contract to refuel USSF military satellites in Geostationary Orbit (GEO). According to Orbit Fab's CEO, Daniel Faber, the typical cost of a kilogram of fuel in space is currently $1 million. However, that cost can be reduced to a couple of hundred thousand dollars with the correct infrastructure and fuel hub execution. This is exactly the mission the group is looking to undertake this semester. The goal is to examine and dream up a network of fuel hubs and refueling shuttles in LEO to extend the lifetime of satellites in an economically and environmentally favorable fashion.

2 Comparable Spacecraft and Missions

As briefly mentioned, Earth orbit is gaining steam with its vision of satellite refueling hubs with refueling shuttles in LEO and GEO. As of February 2023, Orbit Fab has launched its fueling port to the ISS filled with water as a proof-of-concept [5]. Their current goal is to refuel a military satellite in GEO starting in 2025. Investors of Orbit Fab include Northrop Grumman, Lockheed Martin, the ISS, and the USSF. Long-term, Orbit Fab plans to refuel commercial and military satellites with services in LEO and GEO.

SpaceX is taking a different approach to refueling their Starships on their mission to Mars and the Moon. This has attracted the attention of NASA, who awarded SpaceX $53 million for an orbital Starship refueling test. Instead of using designated depots, the approach would include sending two Starships into space where the two would dock and "demonstrate the transfer of ten metric tons of liquid oxygen propellant between one Starship and another" [6]. SpaceX has stated that their Starship's re-usability and orbital refueling make transporting large crews and cargo to the Moon and Mars economically possible [6].

Evidently, there are two strategies. For larger crew and cargo missions beyond GEO, the near future of space refueling appears to be spacecraft-to-spacecraft refueling. For satellites and missions in LEO and GEO, the future dreamed up by Orbit Fab including dedicated depots of fuel and fuel shuttles, is on the horizon.

3 Preliminary Design Specifications

To determine the success of the mission, relevant specifications are listed in this section. These specifications include performance parameters, environmental considerations, sizing, and other general requirements that the spacecraft must pass to complete a minimum viable product. Considerations for a larger market and global impact are also discussed.

3.1 Performance

The performance specifications of SpacExxon depend on the mass of a chosen propellant that can be delivered to a chosen orbit, and the methods allowing for docking with other spacecraft. As the primary customer of SpacExxon will be satellites, hydrazine, a common LEO satellite monopropellant, will be used as the deliverable propellant. From preliminary research, a 1000-kilogram propellant mass will be the target deliverable such that a single launch can refuel ten satellites with 100 kilograms of hydrazine propellant, determined in Section 6.1.

This refueling will be done by connectors designed for small satellites and large satellites alike. Companies will integrate the 12U connector into their spacecraft, combining it with their fuel tank, such that the refueling spacecraft can interface with a known connector when docking with another spacecraft.

3.2 Environment

Spacecraft are subject to extreme conditions in multiple regimes due to large gradients in acoustic, vibration, thermal, and acceleration loads; this requires rigorous analysis for payloads on launch vehicles and in orbit. The loads for SpaceX Starship can be found in [7].

Depending on the selection for the launch vehicle the launch environment will change (See Section 6.3).

Though the launch environment will change based on the launch vehicle, the surroundings in orbit will be constant. Proper radiation and micro-meteorite shielding will be necessary for every propellant tank and instrument aboard SpacExxon. Since radiation can disrupt the operation of sensitive electronic devices, radiation shielding of a high molecular density should be chosen to enclose the electronics. To protect against micro-meteorites, Whipple shielding should be used over sensitive spaces [8].

When orbiting the earth, spacecraft endure large temperature fluctuations every 45 minutes, generally, from -65 to 125° C [9]. To protect against failure, tight interfaces must be analyzed for residual stresses and fatigue from thermal strain.

3.3 Maintenance

Ideally, similar to Orbit Fab, the spacecraft would be designed for a one-time launch and not require any maintenance for the duration of its mission and through its ten-entailed refueling mission quota. If any maintenance is required after the initial launch of the fueling satellite, which could be required due to an uncountable amount of issues that space settings can provide, another mission to make repairs would be required. This falls out of the scope of the main mission and therefore would require a different planned mission not to be detailed in this report.

A mating system to the refueling spacecraft would be required by whichever vehicle may require fuel. This idea is done similarly by Orbit Fab and is known as the Rapidly Attachable Fluid Transfer Interface (RAFTI) service valve. These two docking ports will need to be docked together either by this group's spacecraft, the fuel-receiving spacecraft, or by an intermediary spacecraft for fluid transfer between the two vehicles; as created by Orbit Fab with their Tanker-001 Tenzing transfer vehicle, launched on June 30, 2021. One of many planned to be used for LEO and GEO fuel transfer [5]. A rendering of Orbit Fab's RAFTI valve can be seen in Figure 1.

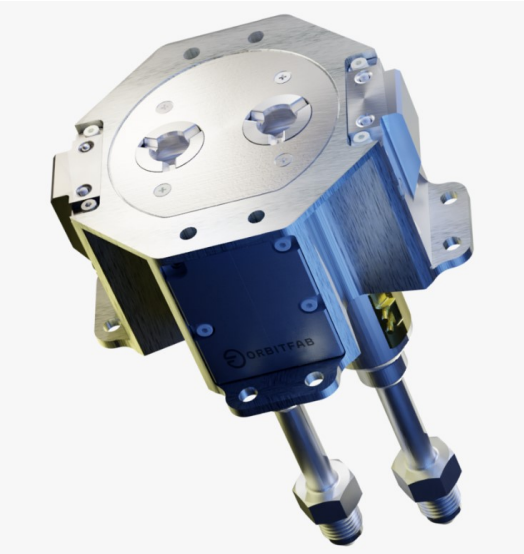

Figure 1: Orbit Fab RAFTI service valve [5].

3.4 Sizing and Weight

The weight of the actual spacecraft may need to be specified in a more applicable form, such as mass, which is not dependent on Earth's gravity, yet can be accounted for in the same form as "weight" concerns. As will be discussed later in the report in Section 6.3, the main constraint that limits the spacecraft design is the amount of mass that the designated launch vehicle could actually bring into orbit. The main concerns are not how large the spacecraft will ultimately be, but how large the overall mass is. This will determine the number of launches required to assemble the modular system if that is the route that is required and settled on.

The compactness of the system is also significant, though it can be assumed that the group will aim to keep the project as dense as possible to make sure this concern is not the limiting factor. No data exists that has been released by Orbit Fab on the sizing and overall mass of their refueling port [5].

3.5 Materials

When determining the varying materials that should be used when manufacturing a spacecraft, the main concern is what will the overall structure components comprise. When looking at varying materials used in the past by almost every satellite in orbit today, as stated by RealClear Science, Aluminum and Titanium would be the most practical materials to use when making a durable space structure [10]. Aluminum offers great strength and durability at a lightweight, and low price. Titanium is another similar material when compared with Aluminum, but it has even greater strength and durability. Though due to its increased scarcity, titanium is much more expensive and therefore used less frequently in spacecraft design.

For the satellite's fuel storage, as stated by Science Madness, "Type 304L and 347 Stainless Steel containers are generally used for storing hydrazine" [11]. Though for hydrazine storage in orbit, as is necessary for all satellites, Titanium is the most commonly used material for hydrazine pressure vessels, specifically Ti6AlV [12]. These tanks would be held internally on the satellite and protected by the designated materials discussed. This would be a dense portion of the spacecraft and likely need to be optimized to minimize the amount of steel being brought up into orbit to make room for other essential pieces of equipment. In Figure 2, a photo of a 177-liter titanium hydrazine storage pressure vessel manufactured by Ariane Group can be seen.

Other materials that will make up smaller portions of the satellite will be solar panels, which are made of primarily silicon, glass, and silver. The reflective wrap that is commonly seen covering satellites and other spacecraft is typically some adaption of Multi-Layer Insulation (MLI) used to prevent radiation and other negative heat transfer effects from the harsh environment of space [13]. Some type of aerospace-grade wiring, typically copper covered in a polymer insulating layer will be used for the internal wiring needs. The computer chips will also be made of primary silicon for their semiconductor abilities, copper-silver alloys, and phosphorus for their conductive properties.

Figure 2: 177 liter Ti6AlV hydrazine tank [12].

3.6 Lifespan

Based on Orbit Fab's mission to deliver 100 kilograms of fuel per refueling mission[5], the SpacExxon design hopes to achieve the same for at least ten refueling missions per depot. For the preliminary design, the mission would ideally last until all 1000 kilograms of propellant are used to refuel ten spacecraft. The required frequency of refuels will be determined through orbital transfer calculations and the chosen propulsion system for SpacExxon. It is likely that SpacExxon will refuel a small range from LEO to MEO, but these orbit transfers will waste the propellant attempting to be sold. Additionally, setting up the depot would likely also waste fuel. This means that the depot will require more than 1000 kilograms of fuel, and this will be something that will need to be explored.

The average lifespan of a satellite in LEO is only 7-10 years [4]. In GEO, most satellites are designed to last 15 years [14]. Refueling can help expand satellite lifetime. Current satellites tend to be limited by fuel, not material deterioration. LEO satellites tend to use fuel to run hardware and correct orbit. Meanwhile, GEO satellites will use their fuel to run their hardware and use one last boost to go further into space [15].

Hydrazine is extremely stable as a fuel, so it can last indefinitely if the tank is uncompromised. The hydrazine in Block 1 satellites that were produced in the mid-90s still works perfectly [16]. Because material deterioration is not the current limitation of satellites, and fuel tanks have proven to be stable for so long, refueling missions have great potential to expand the lifetime of satellites. If refueling was accounted into the launching of new satellites then perhaps satellite companies could design their satellites to last longer in space and SpacExxon and Orbit Fab can raise the life expectancy of satellites in LEO and GEO.

3.7 Customer and Market

The main clientele and market for a refueling spacecraft would be large space agencies and companies. Some possible clientele includes but is not limited to: the National Aeronautics and Space Administration (NASA), the USSF, and SpaceX. A refueling spacecraft could be utilized by said clientele to both refuel current satellites as well as plan to refuel satellites that are part of future missions. Refueling satellites provides value by allowing for the extension of missions as well as preventing collisions between satellites. Refueling a satellite could allow the satellite to avoid collisions and prevent space debris.

Satellites are refueled for various reasons depending on the type of orbit they are in. LEO is the location of most commercial satellites. SpacExxon decided to focus on LEO for this reason, and because the cost of cargo to LEO is much less than GEO. Refueling commercial satellites with hydrazine may be more cost-effective than putting up a new satellite, thus providing value to the customer. The extent to which SpacExxon wants to explore. Refueling in space should ultimately make sense from an economic and environmental perspective. In GEO, there are many spy satellites as well as weather and communications satellites. These satellites are more expensive and, therefore, there may be more of a demand for a refueling spacecraft in this orbit. Orbit Fab has publicly stated that they will sell 100 kilograms of hydrazine at a rate of $20 million in GEO [5].

3.8 Safety, Public Health, and Environmental Impact

The main concerns for safety, public health, and environmental impact for a refueling spacecraft include preventing space debris, product end-of-life, and the toxicity of hydrazine. Preventing space debris is a main concern and a rationale behind this project. A refueling spacecraft may be able to prevent many collisions between satellites that are no longer able to control their trajectories after running out of fuel. This could help the overall issue of space debris that is currently being faced. However, it must also be considered that the spacecraft itself needs to avoid collisions to prevent becoming space debris itself. The spacecraft will need to have a propulsion system to control and make adjustments to its trajectory to maneuver to other satellites and prevent collisions. The end-of-life of the spacecraft will also need to be considered. Following the completion of its mission, the spacecraft will need to be safely and responsibly brought back down to the surface of the Earth. Doing this will avoid the spacecraft from adding to the space debris issue by colliding with anything after it no longer is in use and any other environmental issues it may cause by crashing back down to Earth. Using a reusable launch vehicle to get the spacecraft into orbit may also yield a positive environmental effect.

Another potential issue for safety, public health, and environmental impact is the toxicity of hydrazine. According to the Environmental Protection Agency (EPA), hydrazine is classified as a probable human carcinogen. Exposure can damage the liver, kidneys, and central nervous system. Hydrazine also has reproductive and developmental effects as well as increased cancer risks. Additionally, hydrazine has been shown to cause health effects to animals when exposed [17]. Preventing human and environmental exposure to hydrazine must be a major concern in this project. Environmental impacts will be vital to the justification of the project as competitors cite the economic and environmental benefits of depots as the main reason for justification.

Companies such as Iridium, a global satellite communications company, have developed

standards for dealing with hydrazine when building their satellites. Some of these procedures include using a Department of Transport (DOT) approved tank called DOT 110 when transporting hydrazine. Then, the fuel is stored in an open-air base to stabilize to ambient temperature. The handling of tanks requires leak detectors and emergency breathing equipment. Then, a team of professionals wearing contained atmospheric Personal Protection Equipment (PPE) to handle the transportation of hydrazine from the tank to their satellites [16]. SpacExxon would have to follow a similar sequence of events to ensure the health of workers and not contaminate surrounding lands.

4 Standards and Specifications

A refueling spacecraft will need to comply with many different standards and specifications in order to successfully complete its mission. The following standards and specifications come from NASA's technical report server. NASA's technical reports contain detailed research and analysis results on various subjects related to aeronautics and space. NASA's technical reports will be a crucial resource throughout this project.

The NASA Exploration and In-Space Services (NExIS) Division has been developing technology for the OSAM-1 (short for On-orbit Servicing, Assembly, and Manufacturing 1) mission to robotically refuel, assemble, and manufacture satellites in orbit. The mission has received approval and will demonstrate never-before-tested technologies for use in future missions. The paper focuses on the Propellant Transfer Subsystem (PTS) within the mission, shown in Figure 3, and covers the development of fluid transfer refueling technology, including the Hose Management Assembly and Propellant Transfer Assembly. The mission has the goal of demonstrating on-orbit refueling in 2024 [18]. This is a mission with similar goals to this project and the information in this report can be utilized in the project.

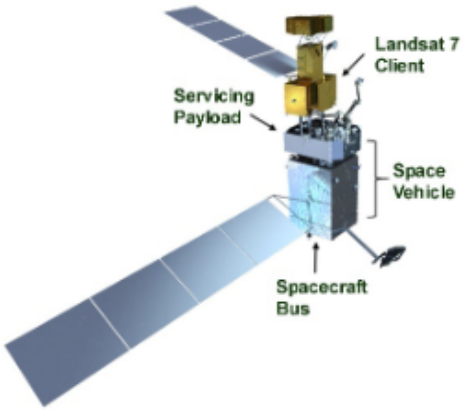

Figure 3: NExIS OSAM-1 Servicing satellite concept conducting propellant transfer [18].

NASA describes a concept for a propellant depot, shown in Figure 4, in a 400 km circular equatorial orbit as proposed to lower the cost of accessing space beyond LEO. The depot will receive tanks of water, convert them to liquid hydrogen and oxygen, and store up to 500 metric tonnes of cryogenic propellants. The stored propellant can support travel to various destinations beyond LEO, including GEO, the Moon, Lagrange points, and Mars.

The tanks are configured to minimize drag, while temperatures are maintained by body-mounted radiators that also provide protection against orbital debris. Power is supplied by rotating solar arrays that track the Sun. The technology could also be applied to larger LEO depots [19]. NASA's mission has the goal of traveling beyond LEO, but the technology of a refueling depot can be applied to this project.

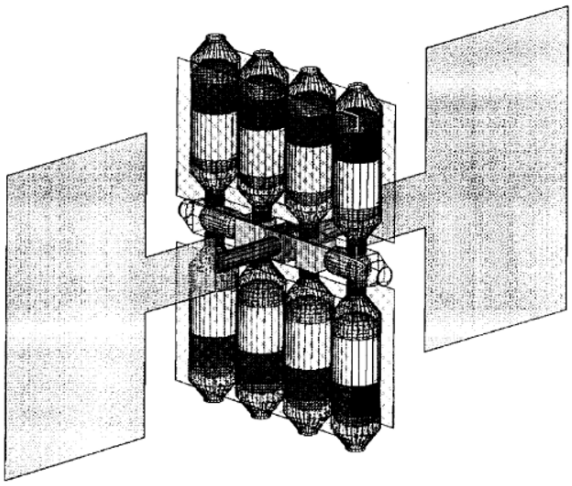

Figure 4: NASA cryogenic propellant production depot for LEO [19].

In another paper, NASA discusses a practical and affordable cryogenic propellant depot solution for human space exploration missions, including the return to the moon and eventual trips to Mars and beyond. The proposed concept uses flight-proven technologies and can be launched with a single Evolved Expendable Launch Vehicle (EELV) medium-class rocket, avoiding the need for orbital assembly. The depot provides storage for cryogenic propellants. Propellant management, flight experience, and key technologies are discussed. Refueling options for the depot and their impact are also discussed [20]. Again, this depot has different goals than that of this project, but the idea of a refueling depot is discussed by NASA several times. The technologies presented in the paper will need to be considered in order to have a successful refueling spacecraft.

NASA patented a magnetic capture docking system, shown in Figure 5. This is a mechanism for attaching a satellite to a vehicle using magnetic forces. The system includes a magnet on the vehicle that creates a magnetic field that interacts with a docking component on the satellite. The magnetic field aligns the satellite and vehicle, and a ball-lock mechanism then mechanically secures the two components together. Rotational guides also ensure that the satellite is properly oriented relative to the vehicle [21]. A similar docking system will be required to be installed on each satellite in order to be refueled by the spacecraft. The docking system described in this patent will need to be reviewed so as not to infringe upon it when designing a docking system for the refueling spacecraft described in this report.

From a NASA patent application, a mechanism is described for docking a spacecraft to a space station using an active docking structure on the spacecraft and a passive docking structure on the station. The passive structure has a docking ring mounted on a tunnel structure attached to the station, while the active structure has a docking ring carried by actuator devices. The devices move the docking ring between positions and respond to signals to absorb impact during docking and secure the spacecraft and station in a final docked

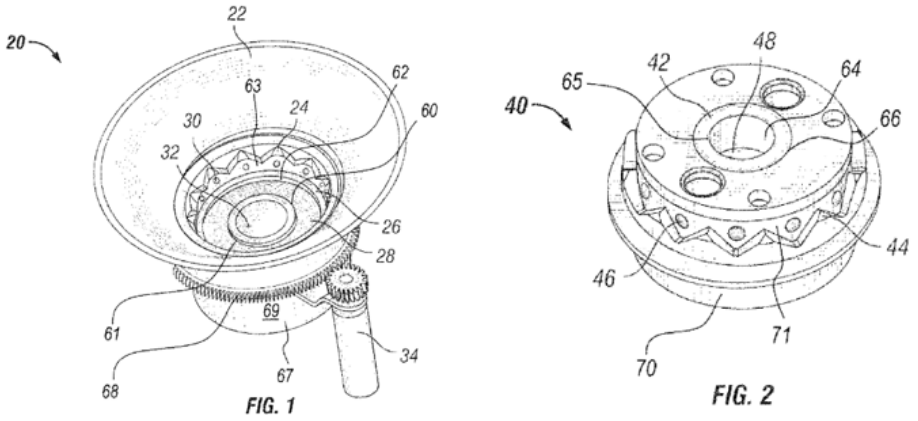

Figure 5: NASA patented magnetic capture docking system [21].

position. The latches couple the rings and establish a connection between the spacecraft and station when the actuator devices retract [22]. Again, a docking system will be an important component of the design of the refueling spacecraft. Extensive research into the docking systems that already exist will be important to the docking component of the design.

5 Mission Profile

5.1 In-plane Orbit Maneuvers

The current mission plan for the spacecraft is to stay in LEO, but be able to transfer from different levels of Earth's orbits in future missions. The satellite will stay in the 300-1000 km range in LEO. This is broad enough to service lots of satellites, but confined enough to have a clear direction of where the satellite is in the atmosphere. LEO is assumed to be the starting point of the spacecraft. A Hohmann transfer orbit will be used to get from LEO to the desired orbit and ultimately to a satellite for refuel. The Hohmann transfer orbit is a two-impulse orbit maneuver, meaning only two changes in velocity are performed when leaving orbit A and arriving at Orbit B. Figure 6 shows an example of a Hohmann transfer orbit going from a lower altitude to a higher altitude.

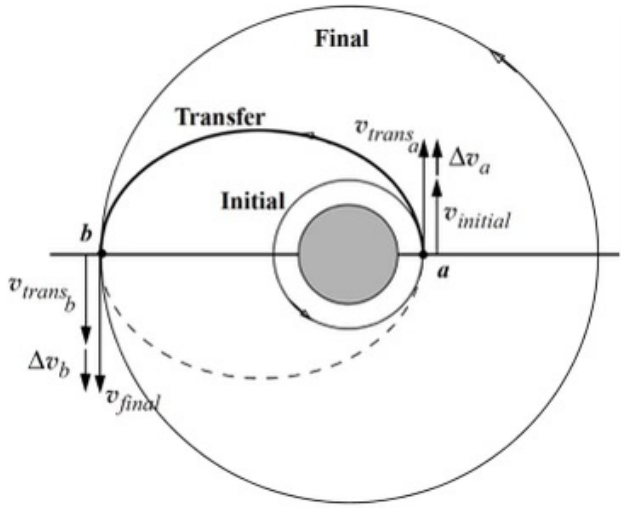

Figure 6: Hohmann transfer orbit [23].

5.2 Hohmann Transfer Significance

The Hohmann transfer orbit is an energy-optimal transfer that is important for the refueling spacecraft due to its propellant mass being an important parameter in the design process. There are a few different ways to prove why Hohmann transfer is the most optimal - including the use of Green's Theorem, graphical construction, or Lagrange multipliers. However, a simple proof from Prof. John E. Prussing, of University of Illinois at Urbana-Champaign, does the trick. This two-impulse maneuver is truly the optimal energy saver. A bi-elliptic maneuver was considered but typically that type of maneuver is reserved for deep-space missions when the destination is around 16 times greater than the starting point [24]. Figure 7 shows the magnitude of the Δv's needed at each altitude. For the Refueling Spacecraft, altitudes will stay in LEO, and will experience very small Δv values.

5.3 Plane Change Maneuvers

To accommodate for satellites in different planes (different inclination angles (i) in reference to the Equator), plane change maneuvers and their Δv values will also be calculated

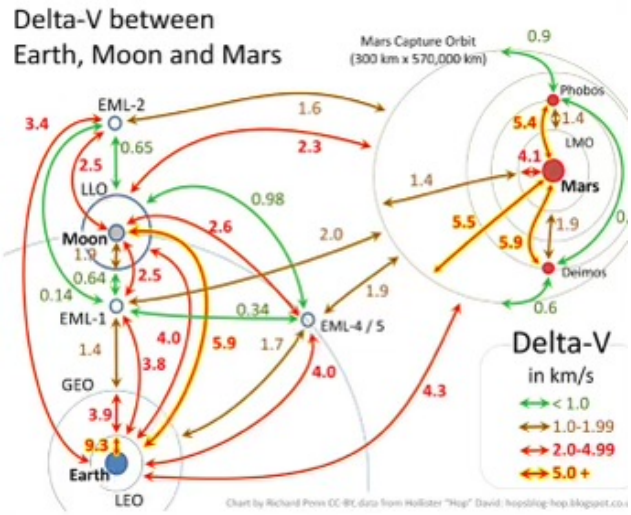

Figure 7: An example of a Δv map including Earth, The Moon, and Mars [23].

at various Δi values. In addition, plane change maneuvers will also be calculated for future three-impulse orbit maneuvers. An illustration of a plane-change orbit maneuver can be seen in Figure 8. These plane changes will be optimally split at each of the three impulses and compared to the in-plane three-impulse maneuver. This will show the range of the refueling spacecraft, and how it is able to go out of its way to serve it's customers.

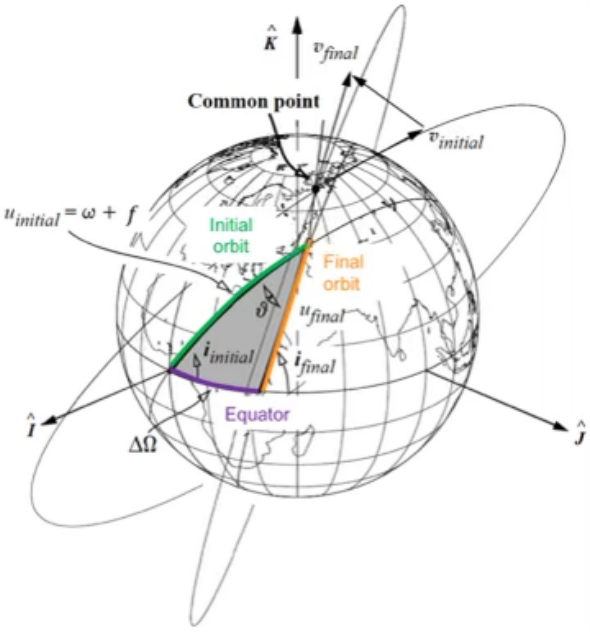

Figure 8: A plane-change orbit maneuver [23].

6 Preliminary Concepts

6.1 Fuel Types

There are many different types of fuel that SpacExxon could hold for distribution. Some of these fuel types are monopropellants, and some are bi-propellants. These bi-propellants require an oxidizer on board and are included in most rockets. Table 1 shows some of the different types of fuels that were considered. Liquid Hydrogen (LH_2) is widely used by NASA for space exploration missions. The satellites that enter/exit LEO would be a great target audience to allow those missions to have higher payload masses due to the lessened focus on propellant mass. Hydrazine (N_2H_4), a monopropellant, is an excellent choice due to how many satellites already use this fuel, but as previously mentioned, it is terrible for the environment [25]. Monomethyl Hydrazine (MMH) is a little different from hydrazine but still is widely used in orbital spacecraft. It is a bi-propellant that is much safer and easier to handle. The Space Shuttle used MMH in its missions [26]. RP-1 is a hydrocarbon fuel similar to kerosene. This bi-propellant is dense and is a great fuel for massive rockets like the Saturn V rocket [27].

Table 1: Fuel Types

Fuel Type	Mono/Bi	Molar Mass $[\frac{kg}{kmol}]$	$I_{sp}[s]$
LH_2	Bi	2	400
N_2H_4	Mono	32	300
MMH	Bi	16	330
RP-1	Bi	175	350

Choosing the fuel type to distribute is an extremely important decision to make. If SpacExxon holds a fuel that is light, but that no companies use, how effective can it really be? If the fuel is too heavy or requires a heavy oxidizer, it may be too inefficient for practical use. These considerations led hydrazine to be the best choice for SpacExxon due to its wide use, independence from an oxidizer, and relatively light molar mass.

6.2 Refueling the Depots

SpacExxon will follow the standards for end-of-life satellites. When satellites reach their end-of-life, the ones in GEO will use their last remaining fuel to be sent even further away from Earth. Meanwhile, LEO satellites will tend to use their remaining fuel to slow down and safely burn up in the atmosphere [15]. That being said, SpacExxon would likely have LEO refueling depots using their last remaining fuel to slow down and fall out of orbit - burning up in the atmosphere. The burning of what was a hydrazine fuel tank in the atmosphere poses a potential problem. Chemicals released by satellites burning in the atmosphere can damage the ozone layer and hydrazine is a carcinogen. This was talked about in subsection 3.8.

6.3 Launch Vehicles

Ultimately, SpacExxon will be delivered into orbit by a launch vehicle. Since the spacecraft will be primarily propellant mass, the decision of the launch vehicle will compare the

diameter of the payload fairing, the maximum payload mass, and the estimated cost per launch. The launch vehicles to be compared are the SpaceX Starship, SpaceX Falcon/Falcon Heavy, and the NASA Space Launch System (SLS) Block 1.

Table 2: Launch vehicle comparison.

Launch Vehicle	Mass to LEO (kg)	Fairing Diameter (m)	Estimated Cost
Starship [7]	100,000	8	$10,000,000
Falcon [28] [29]	22,800	5.2	$67,000,000
Falcon Heavy [28] [29]	63,800	5.2	$97,000,000
SLS Block 1 [30]	95,000	10	$1,000,000,000

Upon review of the 2, it is obvious that the SpaceX Starship and Super-Heavy Booster are the optimal choices to balance cost and mass to LEO. Although this rocket is not on the market and has not had an orbital test flight, it could be used in place of a rocket like the Falcon Heavy, which is currently available for use. The information in Table 2 is summarized in Figure 9.

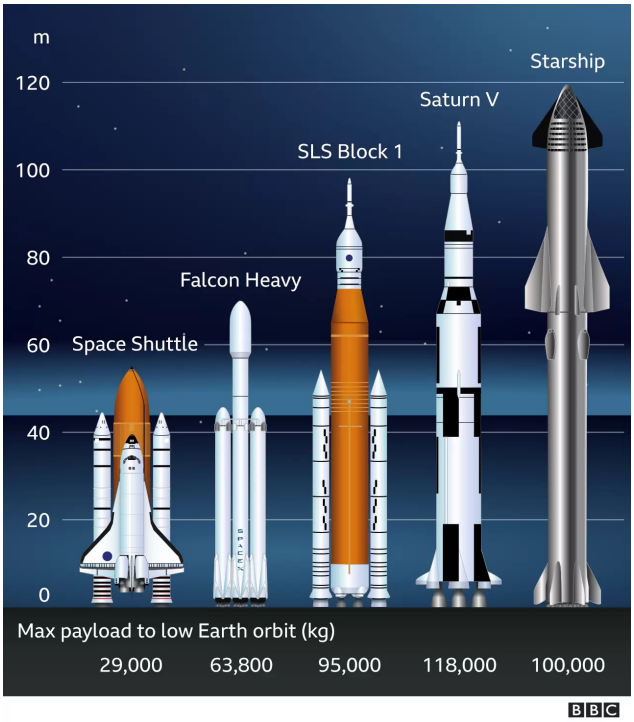

Figure 9: Comparison of high lift launch vehicles based on allowable payload mass to LEO [31].

6.4 Docking

Rendezvous and docking SpacExxon with other satellites is a complicated problem, and there are many solutions. Since the orifice for refueling must be known on both the refueling side and the satellite side, there must be a commercially available port for satellites to integrate into their propulsion systems. After guaranteeing refueling services, SpacExxon must

travel between the satellites to refuel them. To control and orient the refueling apparatus an arm has been chosen. This arm will extend when docking with another spacecraft, and allow for more precise control compared to using direct connection or other refueling drones.

6.5 Guidance, Navigation, and Control

Common systems for spacecraft attitude control include reaction wheels, control moment gyroscopes (CMGs), and Reaction Control System (RCS) thrusters. Magnetorquers are also used to align spacecraft with a planet's magnetic field, but they will not be considered for this analysis. Spacecraft, like the International Space Station (ISS), often use monopropellant RCS thrusters to perform high energy maneuvers, like raising its orbit but also use four CMGs for adjustments in angular velocity [32]. This combination of RCS thrusters and CMGs is a definite necessity for the spacecraft to adjust its attitude.

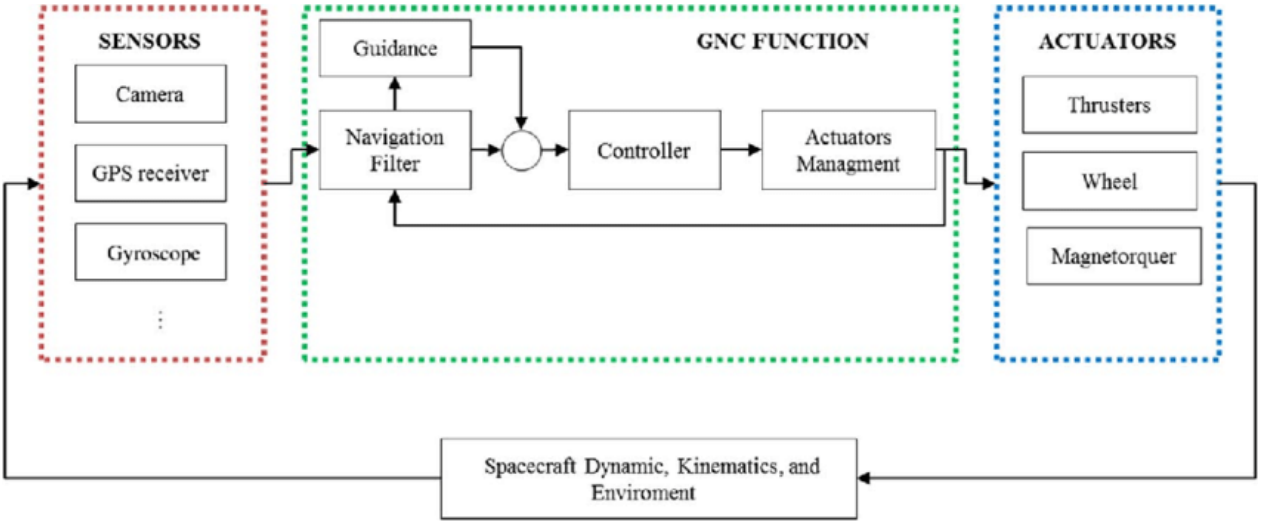

Figure 10: General GNC system architecture [33].

For navigation systems, star trackers provide location data based on the field of view the tracker has of the night sky. This navigation data will then be fed into a guidance algorithm, that will output the required motion through the attitude control systems. This feedback system is displayed in Figure 10. To navigate between satellites for refueling, and correctly position a refueling orifice, the guidance, navigation, and control system will be integral to the performance of the spacecraft.

7 Orbital Mechanics

The following includes subsystems, material and part justifications, and orbital calculations.

7.1 Calculations

Many orbital mechanics-related calculations were made in MATLAB including Hohmann Transfer, Plane Change, and Mass Distribution calculations. See MATLAB Code in Section 19.1. Random altitudes (between 300 km and 1000 km) and inclination angle changes were chosen for a sample mission. These values were different every time. All equations used in these calculations were from EMA 550: Astrodynamics [23].

7.1.1 Hohmann Transfer

The Hohmann Transfer [24] is a two-impulse orbit that will be used to change attitudes in an efficient way. See Section 5 for more information. Equations 1 and 2 show the required Δv for the transfer.

$$\Delta v_1 = \sqrt{\frac{\mu}{r_1}}\sqrt{\frac{r_2}{a} - 1} \tag{1}$$

$$\Delta v_2 = \sqrt{\frac{\mu}{r_2}}\sqrt{1 - \frac{r_1}{a}} \tag{2}$$

These Δv values, which are added together, will help the group find the mass values of the rocket. More Δv values were found at different altitudes and plotted in Figure 11. From this graph, it can be seen that going to a higher altitude requires an increase in speed while lowering down to a smaller height requires a decrease in speed.

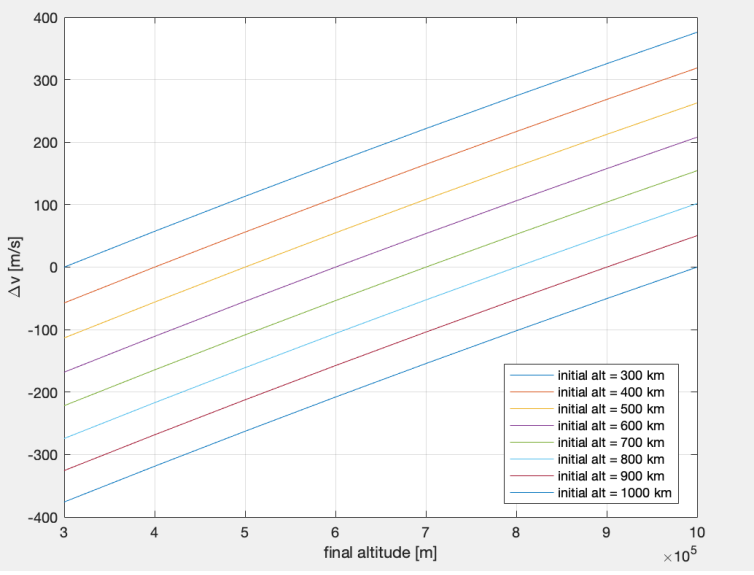

Figure 11: Δv map of Hohmann transfers at various altitudes.

Figure 11 shows that going to a higher altitude requires an increase in speed while lowering down to a smaller height requires a decrease in speed. Additionally, when a final and initial

altitude match, there is no increase or decrease in speed, as expected. A Hohmann transfer does not require a large impulse, as the largest Δv value is less than 400 $\frac{m}{s}$ to get from 300 to 1000 km. Because of this, altitude change is not as much of a concern, and the satellite is free to service anyone in the current range.

7.1.2 Plane Change

The calculations for a plane change are rather simple, only having one short equation. Equation 3 shows that the change in inclination angles and the radial position affect the impulse required to get to a desired orbit.

$$\Delta v = 2v_c \sin \frac{\Delta i}{2} \tag{3}$$

Equation 3 was plotted over a range of 0° to 180°. This plot was normalized by its own radial position to show the effects of angle change more clearly. This plot can be seen in Figure 12.

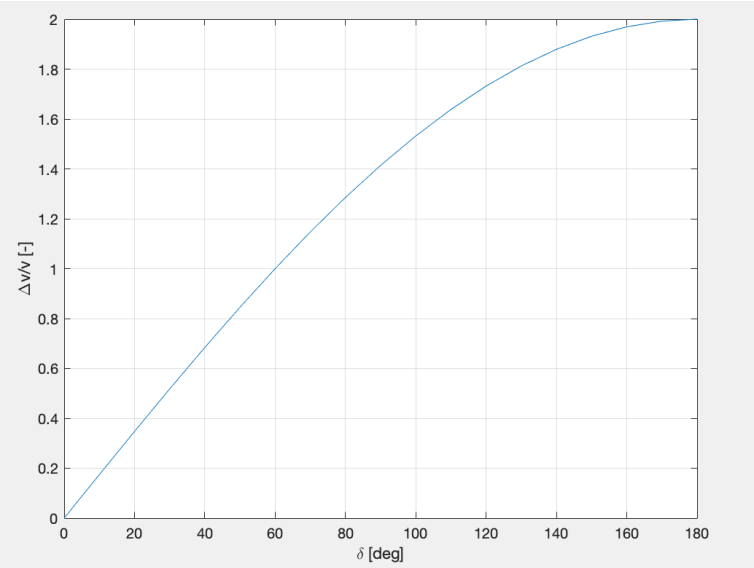

Figure 12: Plane Change Maneuvers at different δ angles.

From this plot, it can be seen that large impulses are necessary to change planes. If a satellite is cruising at 4 $\frac{km}{s}$ and needs to change to a plane 60° away, it will have to have a Δv equal to its current value of 4 $\frac{km}{s}$. Because of this, the Refueler will be making minimal plane changes on a desired mission. Since the Δv value is so high for a plane change, sum of all Δi changes will be $\leq 20°$ for a refueling mission. The range of inclination angles will be determined by the launch site. Figure 13 shows the location and inclination angles at different launch sites.

7.1.3 Optimal Transfer Orbit

When combining Hohmann transfers with plane changes, it is more efficient to do both at once rather than as separate maneuvers. Because of this, the equations used above will not work. Instead, Equations 6, 7, and 8 will be used as a system of equations and solved

Name	Location	Lat	Lon	Min Az	Max Az	Min *i*	Max *i*
Alcantara Space Center	Alcantara, Brazil	2.283	-44.38	343	90	2.3	107.0
Baikonur Cosmodrome, aka Tyuratam Missile and Space Center	Kazakhstan	45.997	63.301	340	90	46.0	103.7
Dombarovsky Launch Site, Russia	Dombarovsky, Russia	50.803	59.512 also Yasny nearby				
Guiana Space Center	Kourou, French Guiana	5.235	-52.772	351	95	5.2	99.0
Hammaguira Space Track Range	Algeria	30.876	3.066 closed				
Jiuquan Space Center	China	40.966	100.285	101	190	42.2	97.5
Kapustin Yar Missile & Space Complex	Russia	48.648	46.017	350	107	48.6	96.6
Kodiak Launch Complex	Kodiak, Alaska	57.436	-152.338	110	220	59.6	110.2
Plesetsk Missile and Space Complex	Russia	62.922	40.661	330	90	62.9	103.2
Reagan Test Site	Kwajalein Atoll	8.720	167.732	-15	145	8.7	104.8
San Marco Launch Platform	Indian Ocean (Kenya)	-2.941	40.213	50	150	2.9	40.1
Satish Dhawan Space Center, formerly Sriharikota Launching Range	India	13.727	80.232	100	290	16.9	155.9
Svobodny Launch Complex	Russia	51.880	128.374 closed, Vostochny replacement				
Taiyuan Space Center	China	38.849	111.608	90	190	38.8	97.8
Tanegashima Space Center	Yoshinobu, Japan	30.400	130.974	90	190	30.4	98.6
Uchinoura Space Center, formerly Kagoshima Space Center	Japan	31.251	131.081	20	150	31.3	73.0
USAF Eastern Test Range	Cape Canaveral, FL	28.533	-80.575	32	111	28.5	62.3
USAF Western Test Range	Vandenburg AFB, CA	34.669	-120.61	152	202	67.3	107.9
Wallops Island	Wallops Island, VA	37.843	-75.479	90	160	37.8	74.3
Woomera, Australia	Woomera, Austrailia	-30.943	136.521	350	45	52.7	98.6
Xichang	China	28.246	102.027	94	105	31.7	28.5
Yavne Launch Facility	Israel	31.898	34.701				

Figure 13: Launch sites with allowable inclinations.

in MATLAB with vpasolve(). Equations 4 and 5 show how to get the perigee and apogee velocities. From these equations, the optimal angles to perform a plane change at, as well as the resulting values of Δv, are calculated.

$$v_p = \sqrt{\mu(\frac{2}{r_1} - \frac{1}{a})} \tag{4}$$

$$v_a = \sqrt{\mu(\frac{2}{r_2} - \frac{1}{a})} \tag{5}$$

$$\Delta v_1 = \sqrt{v_p^2 + v_{c1}^2 - 2v_{c1}v_p \cos(\alpha)} \tag{6}$$

$$\Delta v_2 = \sqrt{v_a^2 + v_{c2}^2 - 2v_{c2}v_a \cos(\Delta i - \alpha)} \tag{7}$$

$$\frac{v_p v_{c1} \sin(\alpha)}{\Delta v_1} = \frac{v_a v_{c2} \sin(\Delta i - \alpha)}{\Delta v_2} \tag{8}$$

The results from this system of equations at the specified locations give a table of Δv values, with the maximum value being just over 1 km/s.

7.2 Sample Mission

A sample mission was performed using optimal-angle Hohmann transfers. It involves 10 randomly selected altitudes between 300 and 1000 km and 10 randomly selected plane changes of less than 2°. This mission is discussed in Section 9.

8 Subsystems

This section includes information on the subsystems of the spacecraft. Each subsystem is broken into component subsections, and considered components are listed within. Many of the components and images were found on SatCatalog [34].

8.1 Propulsion

Since the refueling spacecraft will need to adjust its orbit to successfully dock with customer satellites, a large propulsion system will be necessary. The main components of the propulsion system are the main thruster and propellant. Since the hydrazine tank will be a large custom structural member, integral to the design of the spacecraft, it has its own section. The reaction control thrusters are found in the GNC subsystem.

8.1.1 Propellant

The propellant SpacExxon's depot will use to deliver and get to other satellites is hydrazine. The justifications for hydrazine have already been explained extensively in Section 6.1. For pipe transportation of hydrazine, the pressurant gases that will be used are either Helium or Nitrogen. Both are compatible with the Iridium NEXT tank, which the custom tank is being modeled after, and are often used as pressurant gases for hydrazine shown in Figure 20. Material justifications and the new custom tank that will carry the propellant will be talked about in Section 8.3.

8.1.2 Main Thruster

The main propulsion system responsible for the energy to change orbits is the MONARC445 thruster from Moog. This engine generates the required thrust by means of a hot gas jet produced by the decomposition and expansion of hydrazine. The thruster can provide a steady state thrust of $445N$, and has an SSF-specific impulse of around 230 seconds depending on the upstream pressure [35]. This thruster will be positioned on the aft face of the spacecraft.

8.2 Structures

The main purpose of the structure of the satellite is to both hold all of the components of the satellite together as well as withstand any loading that the satellite will experience. This loading will come during launch in the form of vibration, shock, static, and dynamic loading as well as thermal loading once in orbit. The estimate of the required mass of the structure, a summary of the expected loading scenarios, as well as the selected payload adapter, are outlined in this section.

8.2.1 Internal Structure

The mass of the internal structure needs to be estimated to estimate a preliminary mass of the satellite for orbital calculations. Since the internal structure of the satellite has not been designed yet, a rule of thumb is applied to get a rough idea of the mass of the structure. A good rule of thumb for satellite weight is that 80% of the total mass should be the mass

of the fuel, and the remaining 20% should be divided evenly to the mass of the components and the mass of the internal structure [36].

The internal structure will consist of members that will support the spacecraft during launch, the most intense loading period. The structure will likely be made out of aluminum and steel framing, using trusses to support the main tank. The launch adapter will need to be integrated into the design, and it can go on the forward face of the spacecraft, assuming it is cylindrical.

8.2.2 Load Definition

During the launch, the satellite will experience a range of axial and lateral accelerations while attached to the launch vehicle. This loading range is provided in the Starship Users Guide and is shown in Figure 14. The plot depicts the maximum expected load factors [7].

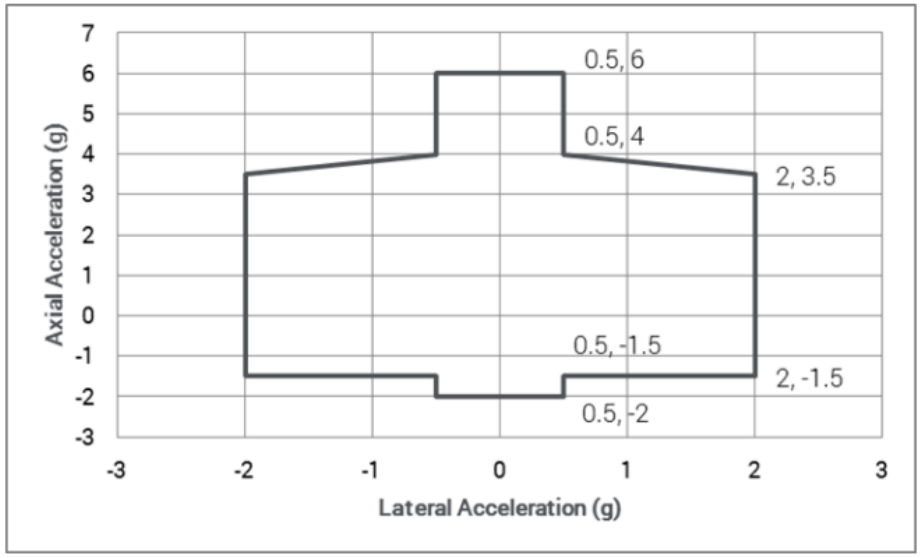

Figure 14: Starship payload maximum design load factors [7].

During the launch, the satellite will be subjected to a range of vibrations."Levels are highest during liftoff and transonic flight, due to acoustic and aerodynamic excitations" [7]. The maximum expected vibrations are shown in Figure 15.

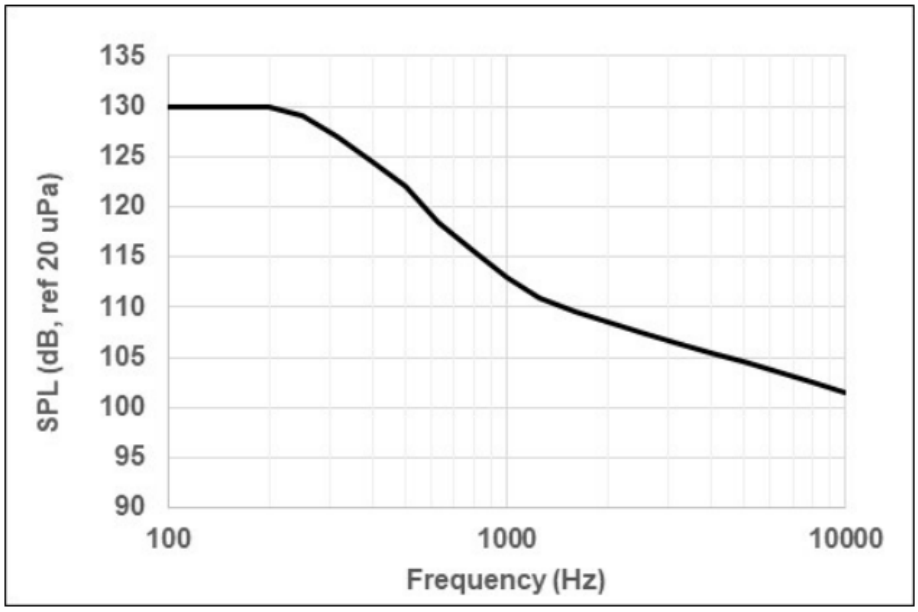

Figure 15: Starship payload acoustic environment (1/3 octave) [7].

The satellite will experience maximum shock due to the payload separation [7]. The typical maximum shock levels at the payload separation are shown in Figure 16.

Frequency (Hz)	Shock SRS (g-peak)
100	20
1000	1000
10000	1000

Figure 16: Starship typical payload separation-induced shock at the payload separation plane [7].

This loading defined in the Starship Users Guide will inform the internal design. Additionally, the structure of the satellite will need to be analyzed to ensure that it can withstand the given loading scenarios. The loading definition will be particularly important and frequently referenced when completing Finite Element Analysis (FEA).

8.2.3 Starship Fairing Volume

The payload fairing is the envelope that encloses the payload on the launch vehicle. It serves the purpose of holding and protecting the satellite during launch. The volume of the fairing is a limiting factor for the sizing of the satellite. The satellite must fit within the volume of the fairing and be mounted using a payload adapter. The Starship Users Guide does not provide the explicit fairing volume, so this value must be estimated. The dimensions of the fairing are provided in Figure 17 [7].

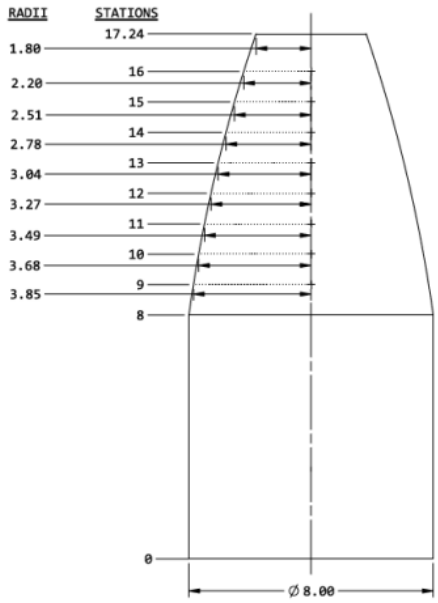

Figure 17: Starship payload volume (dimensions in m) [7].

The volume is then estimated by calculating the volume of a series of cylinders with dimensions corresponding to Figure 17. The volume of each of these cylinders is then added together to get an estimated total fairing volume of 664.025 m^3. Note that this will be a slight underestimate.

8.2.4 Payload Adapter

According to the Starship Users Guide, Starship will have a standardized payload adapter to interface between Starship hardware and consumer satellites [7]. This can be assumed to be similar to the SpaceX Falcon launch adapter. The Falcon payload launch adapter is a 1,575 mm (62.01 in.) diameter bolted interface. It is designed "to conform to the EELV 1,575 mm (62.01 in.) diameter medium payload class mechanical interface defined in the EELV Standard Interface Specification" [29]. The payload adapter interface is shown in Figure 18.

Figure 18: SpaceX Falcon 1,575 mm payload adapter [29].

Although it can be assumed that the Starship will use a similar standardized payload adapter, SpaceX has yet to release any information about it. Therefore, it cannot be used for this project. For SpacExxon, the SpaceX Falcon launch adapter will be used. All information for this payload adapter is given in the Falcon User's Guide [29]. Information that will be useful for designing the connection to the adapter such as sizing and bolting pattern is given. A drawing of the payload adapter with sizing and the bolting pattern is shown in Figure 19.

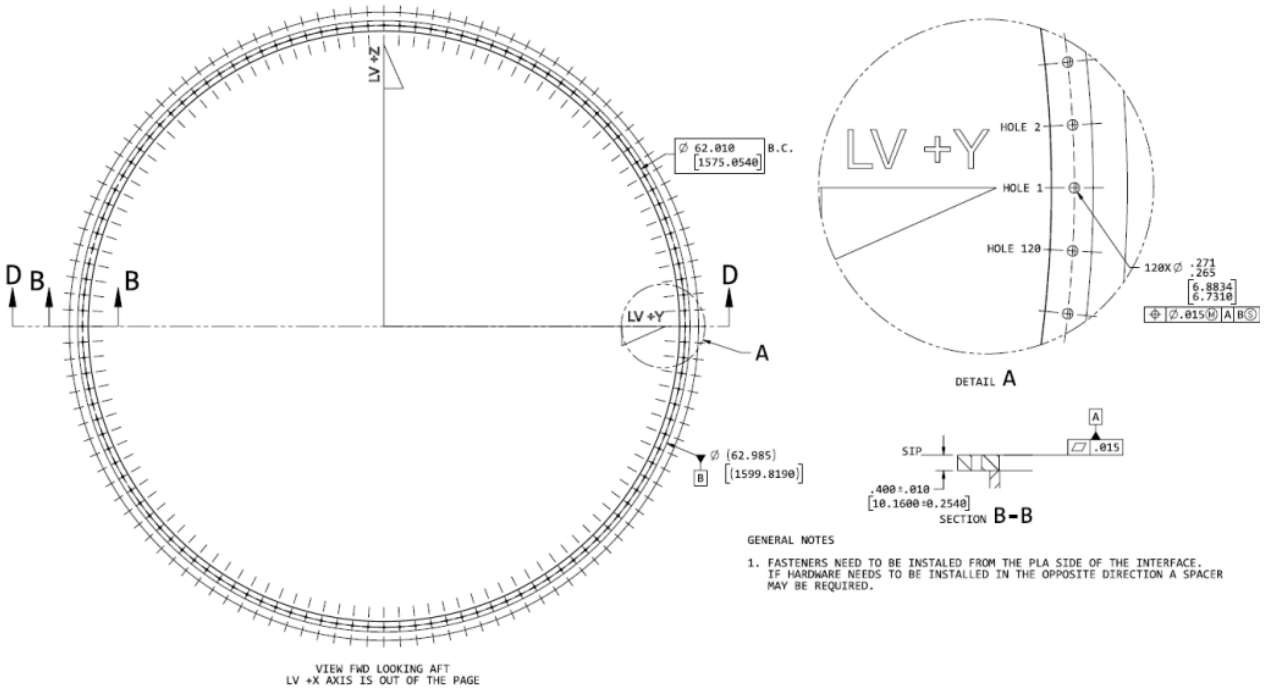

Figure 19: SpaceX Falcon 1,575 mm payload adapter drawing with dimensions [29].

8.3 Hydrazine Tank and Thickness Considerations

The tank is arguably the most important early consideration because SpacExxon's mission is to carry enough fuel to refuel at least ten satellites. Therefore, the tank will have to be custom-designed. The following sections will walk through the considerations that SpacExxon went through to justify the final tank design.

8.3.1 Material Justifications

A critical requirement in the design of the depots and justification that refueling can extend the lifetime of satellites is the material compatibility of storage or transportation material with the propellant. That is, what should the fuel tank and the pipes for the transportation of fuel be made of?

To help answer this question, SpacExxon referred to the design book "Material Compatability with Space Storable Propellants" prepared for the Jet Propulsion Laboratory at CalTech [37]. The guidebook intended to summarize the information gathered from literature searches and their personal contacts. It gives material compatibility of metals and non-metals on a variety of propellants including hydrazine. Focusing on hydrazine, the fuel SpacExxon is concerned with, Table 3 summarizes the findings for metals and nonmetals that were found to either have compatibility or probable compatibility with hydrazine for long-term storage of fuel.

Table 3: Compatibility Summarizing of Metals and Nonmetals with Hydrazine - conflicting data or data based on sister material [37].

Compatability Level	Metals	Non-Metals
Compatible	**Aluminum** (Pure, 1100, 2014*, 2024, 3003, 5052, 6061*). **Titanium** (Alloys in general, 6Al-4V, 5Al-2.5Sn, A-70). **Tantalum, Zirconium**	**AF-E-102** **AF-E-332**
Probable Compatability	**Aluminum** (General, 2021, 2219*, 356) **Steel** (Short term only. 301 Cryoformed, 304, 321, 410, 430, 440C, 17-4 PH or 17-7 PH, A-286) **Lead, Platinum, Tin, Chromium**	**TFE Teflon** **FEP Teflon** **Kel-F** **Polyethylene** **Rulon** (PTFE) **EFR's** (general, 132) **EPT's** (general, 10) **Graphite** **Asbestos**

Considerations of compatibility included that the material would not corrode for metals and that there was a negligible loss of physical properties for non-metals. For metals, the general observation is that the metal type could have potential effects on the propellant, but not the other way around. Particularly, metals show great corrosion resistance for long-term storage of neat hydrazine. Corrosion of metals was only a concern with contaminated hydrazine [37]. This indicates that the quality of the hydrazine is a significant consideration for long-term storage in space.

The effects that some metals can have on hydrazine, however, are highly dependent on the metal type. Therefore, it is an extremely important consideration for long-term storage. Orbital theory helps explain the trend. For metals with incomplete d-subshells, they showed an increased decomposition rate of hydrazine. Compared to a control sample in glass, nickel decomposed at a rate 200 times greater, stainless steel 316 times greater (up to only 10 times greater with 304 and 321 SS), and aluminum decomposed at approximately the same rate as control samples [37].

In a separate report, TRW and DMIC quantified a metal as compatible for long-term storage of hydrazine if it has a corrosion rate of less than one ppm/yr, does not promote hydrazine decomposition and was not considered shock sensitive in contact with hydrazine [37]. All metals in Table 3 were considered compatible within this definition.

One of the longest-lasting satellites in space is Iridium's Block 1 satellites that were launched in the 1990s. The block 1 satellites use a titanium alloy fuel tank that still "works perfectly" [16]. Evidently, there is great potential to extend satellite lifetime in satellites that use compatible metals for fuel storage.

In conclusion, based on the recommendations of the guidebook and searching what most fuel tanks are made of, the fuel storage tank that SpacExxon will be made of either titanium

or aluminum alloys that are contained in Table 3.

8.3.2 Mass Justification

Because of the large amount of fuel the SpacExxon depot carries, it was necessary to design the fuel tank. An appropriate way to do this is to take an existing hydrazine tank design and make modifications. Since the Iridium Block 1 satellite tanks talked about in the previous section were proven to be extremely reliable, SpacExxon used the Iridium NEXT mono-propellant diaphragm tank as an example [38]. Iridium NEXT is the next-generation satellite following Block 1. Specifications were not public for the Block 1 satellites, but the NEXT tank was most likely the same or inspired by the Block 1 tank. The Iridium NEXT tank is designed for hydrogen and nitrogen pressurant gases.

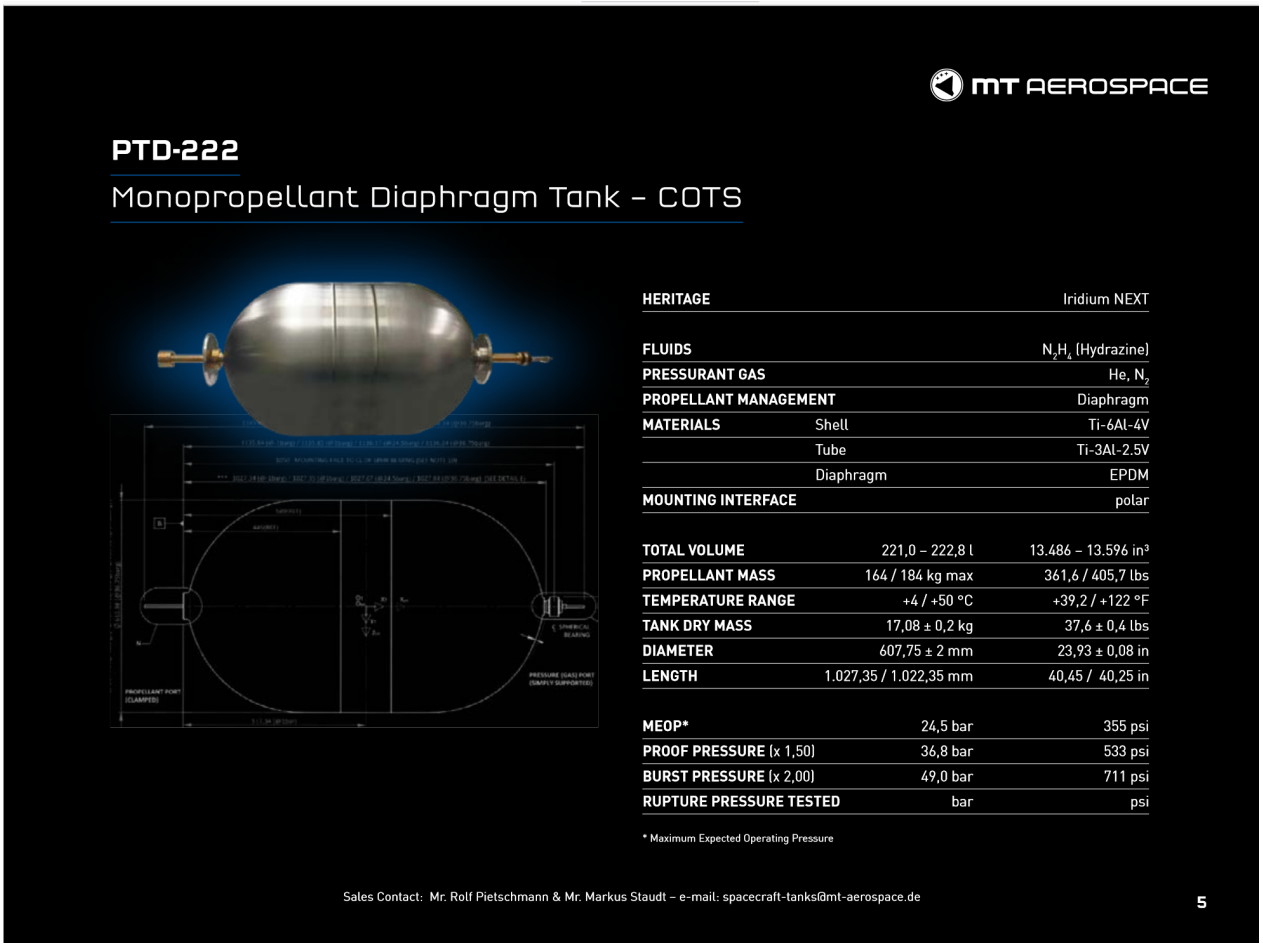

Figure 20: Iridium NEXT PTD-222 monopropellant diaphragm tank specifications [38].

Figure 20 shows the design specifications of the Iridium Next Tank. The tank is designed for a maximum propellant mass of 184 kg. SpacExxon needs to carry 1000 kg of payload propellant in addition to the propellant that will go into arriving at the satellites. The first assumption that is being made is that hydrazine is incompressible. The justification of this assumption is that liquid hydrazine has a compressibility factor of 2.45E-5 per atm [39]. At its maximum expected operating pressure (MEOP) of 2.45 MPa (24.2 atm), this means the

volume changes proportionally < 1E-3, a change of less than 0.1 percent. Therefore, the material properties of density at STP is;;;;;;;;;;; a good assumption for hydrazine. At STP, hydrazine has a density of 1021 kg/m^3 [39]. This is helpful to find the overall propellant mass that can be carried on the tank given a volume using Equation 9 to relate density (ρ) to mass (m) and volume (V). This equation will help determine the new internal volume needed to store the payload and additional propellant.

$$\rho = \frac{m}{V} \tag{9}$$

The tank is designed for a MEOP of 2.45 MPa [38]. Unfortunately, the thickness of the tank is the key information missing from the tank specification information.

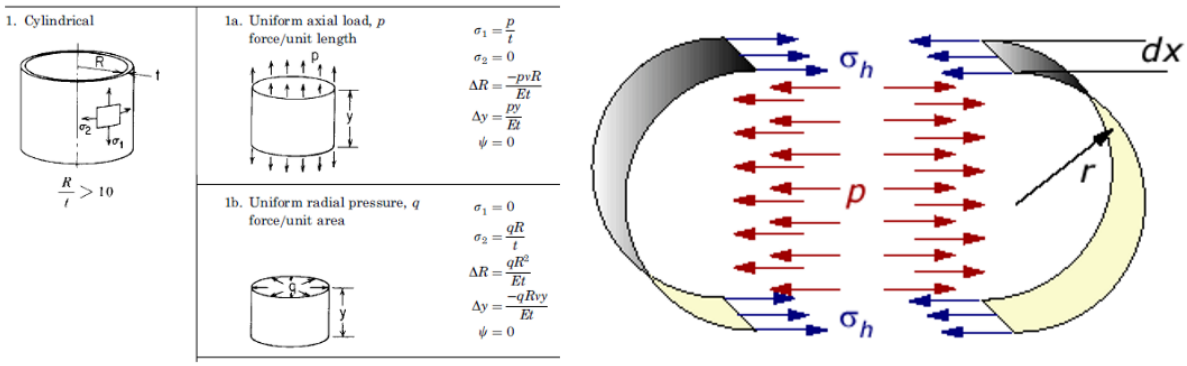

Figure 21: The two loading conditions for diaphragm tank design [40] [41].

Therefore, SpacExxon did some backtracking to figure out the thickness and maximum stresses to find the new thickness for the larger tank design. The magnitude of these stresses depends on if the pressure vessel is a thin-walled or thick-walled vessel. A thin-walled pressure vessel is defined as having a thickness at most 1/10th of the smallest inner radius [40]. The Iridium NEXT tank is a thin-walled pressure vessel, so the new tank design should also include a final check if it is thin-walled to justify the following assumptions that went into calculating the new tank.

In space, the maximum internal pressure will be equal to the MEOP. As for the external, outer space pressure is essentially zero. So, the thin-walled pressure vessel is in a load condition of an internal uniform radial pressure of MEOP. The diaphragm tank design is composed of a cylindrical middle base and a spherical-type end cap. The result is that the tank will experience hoop and longitudinal stresses in superposition. Figure 21 illustrates the cylindrical loading conditions and the spherical end-cap which will have hoop stress along the end-caps but also add longitudinal stress for the cylinder.

Case 1b on the left side shows the conditions for uniform radial pressure in a cylindrical pressure vessel [40]. Meanwhile, the spherical stresses have a magnitude half that of the cylindrical hoop stress in both directions [41]. This will also result in longitudinal loading stress in the cylindrical direction as indicated by the right image in Figure 21. As a result, the largest stress - the limiting factor - is the hoop stress in the cylindrical loading condition. This stress is given in Equation 10, where σ_{max} represents the maximum (hoop) stress experienced as a function of radial pressure (q), the radius of the tank (R), and thickness of the tank

(t). MEOP already defines the factor of safety of 1.5 for proof bursting and 2.0 for burst pressure, so the factor of safety is already included in this calculation.

$$\sigma_{max} = \frac{qR}{t} \tag{10}$$

Using Equation 10, MEOP as the maximum pressure, the radius of the Iridium NEXT tank, and the tensile yield strength of the shell (Ti-6Al-4V, 1100 MPa) [42], the minimum thickness of the Iridium NEXT tank was calculated to be 0.027 inches or 0.68 mm. For a logical check, SBI, a plasma welding company, states that propellant tanks of satellites usually are made of titanium sheets with a thickness of 0.8-1.2 mm [43].

Based on original estimates from Section 19.1, the tank will need to carry at least 7769 kg of fuel. To round up, the design will be for 7800 kg of fuel. Using Equation 9, that equates to a tank with a volume of 7.64 m^3.

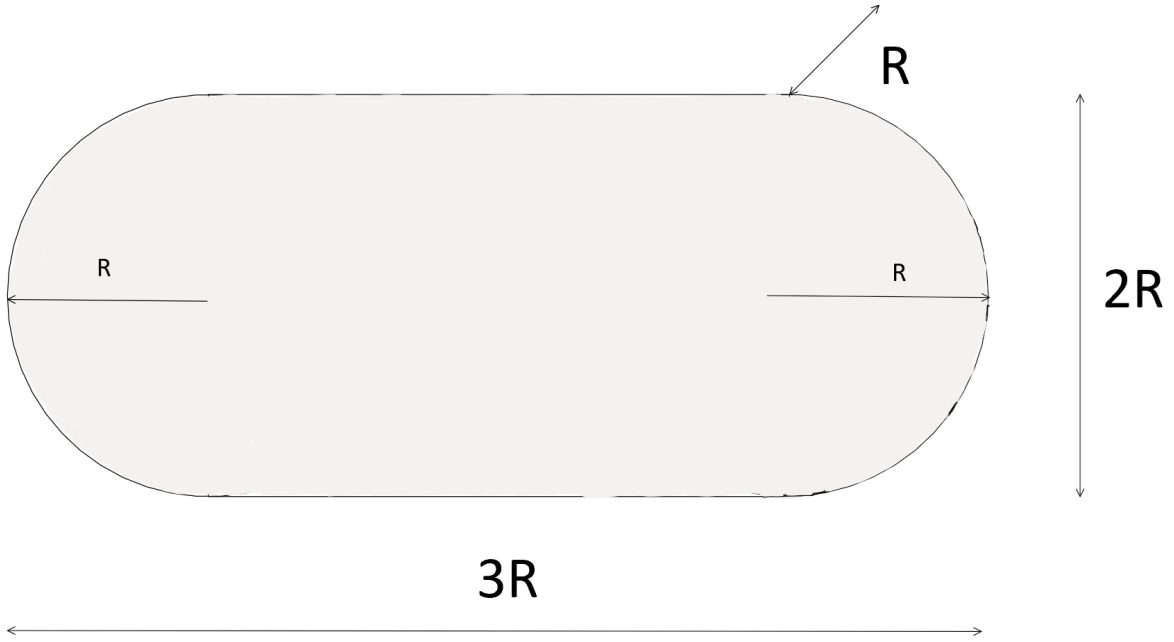

Figure 22: Dimensions for new diaphragm tank design.

Figure 22 shows the dimensions of the new tank design, based on the approximate proportions of cylindrical and spherical tank space on the Iridium NEXT tank. This is helpful to find the radius of the tank design.

$$V = \frac{7\pi R^3}{3} \tag{11}$$

Combining the spherical volume and cylindrical volume equations, Equation 11 was used to find the tank needs a radius of 1.01 meters to support this fuel. Additionally, using Equation 10, and the new radius of the tank, the thickness required for this tank equals 0.088 inches at a minimum, or 2.23 mm. Then, the new tank design has a mass of 223 kg - about 13 that of the iridium NEXT tank but carrying approximately 46 times the amount of fuel.

8.4 Guidance, Navigation, and Control

To properly operate a stable spacecraft, a Guidance, Navigation, and Control (GNC) system is required. The GNC system connects the planned trajectory, the current spacecraft attitude, and the control actuators. In short, navigation is where the spacecraft is currently going, guidance is knowing how to get to a final position, and control is the execution of the commands generated by the guidance system by onboard actuators. There are many sensors necessary for generating the state of the spacecraft at any given moment: inertial measurement units (IMU), star trackers, horizon, and sun sensors, for example. The main flight computer and onboard avionics handle the input and output of all three systems. Actuators like the reaction control system, reaction wheels, control moment gyroscopes, mangetorquers, and more, assist in the repositioning of the spacecraft for a given attitude. This section will summarize the chosen components for the GNC subsystem.

8.4.1 Avionics

The main flight computer is an essential piece of avionics hardware that is necessary for space travel. The main flight computer helps calculate flight paths, fuel burn rates, and overall data processing for any of the craft's various subsystems. The computer selected for this spacecraft was selected due to its unique compactness, low dry mass, and low energy sink from the main battery. Figure 23 shows the Magellan Aerospace, CDH On-Board Computer that was selected for use.

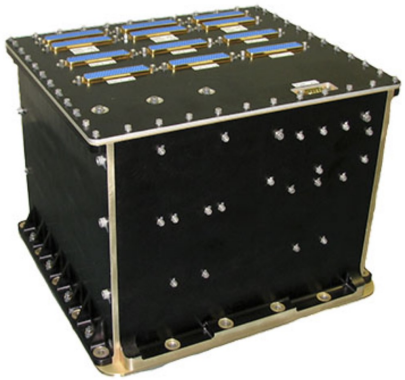

Figure 23: Magellan Aerospace CDH on-board computer [34].

A spacecraft's main flight computer has a processor at its heart, used to handle the mass amounts of data being stored, sorted, and constantly intersected from the plethora of system inputs. The processor selected has been widely used in past missions with high reviews and yields an almost "negligible" low mass [34]. Figure 24 shows an image of the Airbus SCOC3 ASIC CDH subsystem processor that was selected for use.

Similar to the other portions of avionics previously discussed, the Inertial Measurement Unit (IMU) helps with the overall navigation of the Spacecraft. The IMU impacts the navigation by relying upon specific gravity and angular rates of the item it is attached to and relying on that data to other subsystems that rely on that data, making the IMU a vital navigation subsystem. The selected ASTRIX NS IMU was chosen due to its compactness and low mass, a common theme used when selecting internal sub-components for satellites. The IMU selected for use can be seen in Figure 25.

Figure 24: Airbus SCOC3 ASIC CDH subsystem processor [34].

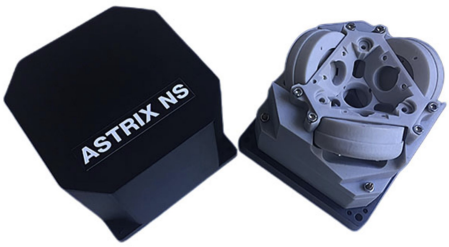

Figure 25: Astrix NS IMU [34].

The last piece of avionics hardware is the Northrop Grumman Scaleable SIRU-E Avionics package optimized for small satellites. In the words of Northrop, "spacecraft manufacturer's choice for sensor pointing/stabilization and spacecraft attitude control on demanding long-term space" [34]. This compact system will aid in improving the control of the satellite with its subsystems, acting in unison with the main flight computer and IMU. Figure 26 shows an image of the selected avionics package chosen by the team.

Figure 26: SIRU-E Northrop Grumman avionics package [34].

8.4.2 Control Moment Gyroscopes

Two common control actuators for generating moments to react to changes in angular velocity are reaction wheels and Control Moment Gyroscopes (CMGs). Reaction wheels generate torques by changing the angular velocity of a rotating flywheel, and this change is transmitted in an equal and opposite manner to the spacecraft due to the conservation of momentum. CMGs use different dynamical approaches, and instead, make use of a phenomenon called gyroscopic precession to generate moments about specified axes. When a force, or precession is applied to a flywheel with a given angular velocity, a gyroscopic moment is generated about a third orthogonal axis. This axis is then aligned using motors to generate an equal and opposite spin for the spacecraft. The chosen CMG for the spacecraft is the CMG-8, a package containing four flywheels in two axes, by black Canyon Technologies. The CMG-8 is less than 10 kg and can provide 8 Nm of maximum torque and draws 15 W at full momentum [44]. Two of the CMGs will be used for redundancy.

Figure 27: CMG8 from black Canyon Technologies [44].

Reaction wheels are commonly used on spacecraft to electrically control attitude. These maneuvers, however, are often over long time periods, and since the refueling spacecraft requires instantaneous control when docking, there will be an accompanying system of reaction thrusters. Also, these wheels produce moments, and often, linear momentum needs to be used to generate desired motion.

8.4.3 Reaction Control Thrusters

For high impulse control maneuvers, a Reaction Control System (RCS) consisting of five hydrazine MONARC90-LT thrusters will be used. These thrusters are from Moog and have a specific impulse of 230 seconds depending on the pressure of the propellant [45]. There will be five thrusters positioned on top of the spacecraft. These specific thrusters were chosen as opposed to cold gas thrusters because there will be substantial inertia due to the large amount of fuel in the tank. More details on the specifics of the RCS system are detailed in Section 15.5.

8.4.4 Communication

In order to communicate with the satellite in LEO, an antenna, transmitter, and receiver are needed [46].

There are a variety of satellite frequency bands that can be used, and designated levels have been developed for specific uses. Because of SpacExxon's satellite functionality, it would make the most sense to transmit and receive on the S-band (2-4 GHz). According to The European Space Agency, the S-band is appropriate for satellite communications - for example, NASA uses this band to communicate with the ISS and Space Shuttle [46].

The parts that SpacExxon will use for this purpose are EnduroSat's UHF Antenna III, their S-band Tx Type I transmitter, and their S-band transmitter. An advantage to using a wire-type transmitter is the extremely low weight - because it is not providing a communication service, it does not need a reflector-type antenna which would be heavier [34]. With all three parts, the weight totals 0.515 kg.

Figure 28: EnduroSat's receiver (left), transmitter (middle), and antenna (right) [34].

8.4.5 Star Tracker

The navigation system requires consistent inputs from multiple sensors to determine the state vector or attitude of the spacecraft. As stated earlier, the IMU records linear and angular accelerations, but this is not enough for the determination of an orbit. A star tracker is a computer-vision system that compares a given view of celestial objects with a database of constellations for a given time and triangulates the spacecraft's attitude with that information. This is similar to how an autonomous vehicle might call on Google Maps, or a similar database, to determine its position. The chosen star tracker is the Sagitta star tracker from Arcsec, a CubeSat control system manufacturer [47]. This star tracker provides arcsecond range pointing accuracy, with an average power draw of 1.4 W. Figure 29 shows an image of the star tracker.

Other potential sensors are sun and horizon sensors. A sun sensor is self-explanatory and assists in the determination of orbital period, scheduling for high power subsystems, and attitude for maximum solar energy capture. The horizon sensor is similar to the sun sensor, but instead, it faces the earth to determine spacecraft alignment with geocentric coordinate systems. It is assumed that an IMU, star tracker, reaction wheels, and reaction thrusters will be sufficient for the Attitude Control and Determination System (ACDS) and GNC system.

8.4.6 Camera

Attached to the satellite to either be deployable or fixed externally, three cameras will be necessary for ground crews to get essential imaging on the portion of the satellite that will be docking with other spacecraft for their refueling purposes. Two will be positioned on the main satellite and another with be used on the planned arm to be used for navigating fuel

Figure 29: Sagitta star tracker [47].

during the refueling process. The selected camera is the MultiScape200 CIS manufactured by Simera Sense. This camera selection was used due to the compactness, low mass, and relatively low power usage per unit. Additionally, the camera has 12-bit pixel depth and offers seven different spectral viewing bands. Figure 30 shows an image of the MultiScape 200 camera that can be seen.

Figure 30: MultiScape200 CIS Simera Sense camera [34].

8.5 Thermal Systems

Thermal systems are integrated into all satellites and spacecraft to maintain the craft's sensitive internals within their allowable temperature ranges, typically within -170°C to 123°C in LEO orbit [48]. The passive systems the team plans to incorporate into the design typically involve external insulation, a heating and cooling system, and typically an external debris shielding system that adds a tangible amount of insulation as well.

8.5.1 Insulation

The incorporated insulation is Multi-Layer Insulation (MLI), also known as the shiny reflective materials that many recall as "tinfoil" wrapped on the exteriors of most spacecraft and satellites, especially those with much external imaging hardware that is particularly sensitive to radiation. Ten layers of MLI will be incorporated into this craft. Ten layers are within the typical amount of layers used for spacecraft to reflect 90% of external heat

encountered as stated by DesignNews in an article on the *The ABCs of Multi-Layer Insulation for Spacecraft* [49]. Figure 31 is an image showing a closer look at typical MLI used for radiation management in spacecraft thermal systems.

Figure 31: Multi–Layer insulation piece manufactured by Dunmore [13].

The insulation is typically applied in sheets and adhered together with adhesive strips. Each sheet averages around 50 microns thick, and with ten layers around almost the entirety of the satellite, the mass per unit area equals 0.69 kg/m^2. Another important aspect of passive thermal systems is the heating and cooling sources implemented into the internal system.

8.5.2 Heaters and Coolers

Heaters and coolers are always incorporated into satellites and especially spacecraft that house crew. Luckily, the satellite is unmanned and only requires enough heating and cooling to maintain the sensitive hardware from malfunctioning, which is a much larger range than needed to be maintained for human life. The heater and cooler system that will be used to counter the extremes of space is a Standard Passive Orbital Thermal-control (SPOT) structure manufactured by Thermal Management Technologies. As stated by the manufacturer of this passive thermal management system, "TMT adapted its multi-functional, heat spreading structure technology and scaled it to smaller satellite configurations... and smooths out the temperature extremes in the environment of space. SPOT facilitates the use of available satellite area and thermal capacitance"[50]. In figure 32, an image of the 6U SPOT structure can be seen.

The SPOT system utilizes electric resistance heaters similar to thermal straps which utilize braids, AKA straps, of highly-conductive material such as copper and graphite alloys to create the heat sources as current runs through. The SPOT conversely uses thermo–electric coolers to counter any extreme heat sources in the satellite. The next important aspect of thermal systems for satellites is the added thermal protection that results from the addition of external debris.

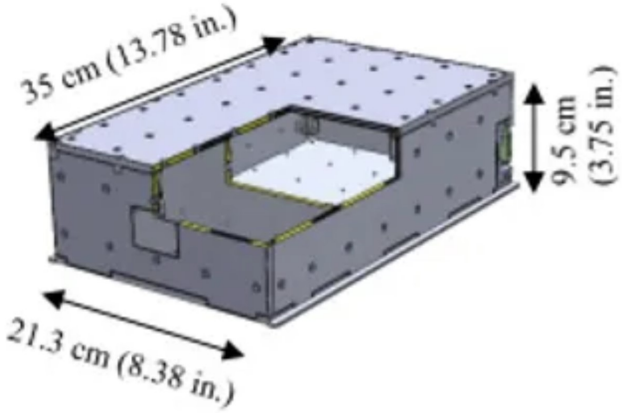

Figure 32: Standard Passive Orbital Thermal–control (SPOT) manufactured by TMT[50].

8.5.3 Whipple Shielding

Shielding against micrometeoroid and orbital debris (MMOD) in space, an ever-growing necessity as the commercialization of space continues to grow, has been implemented in spacecraft since they first left Earth's atmosphere. A time–tested and simple solution to MMOD is the implementation of Whipple shielding on the outside of the craft. First invented by Fred Whipple of NASA in the 1940s, the Whipple shield implements an outer metallic screen to break up the initial MMOD and lessen the cloud impact on the back-lying aluminum plate that absorbs the majority of the impact, preventing puncturing of the spacecraft [51]. A newer adaption of Whipple shielding that has been adopted by space agencies since the 1940s is the Aluminum foam Whipple shield. Similar to honeycomb shielding, which is used on the International Space Station (ISS), the aluminum foam has an outer screen, and a back plate, but the majority of the stopping power originates from the porous aluminum foam that is between the two walls instead of the honeycomb array used on the ISS. Shown in Figure 33 is an image of a cutaway of aluminum foam Whipple shielding technology after an impact test. This form of shielding has a density per square meter of 16.8 $\frac{kg}{m^2}$ and will be used mainly for the protection of the hydrazine payload, which the mission is planned around in its entirety. The ballpark mass that this portion of the depot will add to the overall mass is not known as of now due to the variability of the unknown surface area.

When compared with the typically used Honeycomb MMOD shielding, "the foam modifications were shown to provide a 15% improvement in critical projectile diameter at low velocities (i.e. 3 $\frac{km}{s}$) and a 3% increase at high velocities (i.e. 7 $\frac{km}{s}$) for normal impact [52]. The thermal insulating features mainly are attributed to the fact that the Whipple prevents the internal structure from being penetrated. The physical thermal shielding offered by the aluminum foam Whipple is relatively minimal as aluminum is conductive, though when covered with the MLI it will offer more of a barrier between space and the inside than if nothing

Figure 33: Aluminum foam MMOD shielding cutaway after impact [51].

was there; think of the comparison of the temperature shielding a car door offers.

8.6 Power Systems

To capture, manage, and disperse energy on the spacecraft, a power system is necessary. Generally, the spacecraft will require a specific amount of power for a given maximum operating state; this power must be generated through the conversion of solar radiation to electrical energy, and this energy will be stored inside batteries. The batteries must be able to supply the maximum operating power for a given half-orbital period, without the need for solar panels. The power systems are significant because, without a consistent power source, the actuation of motors, computation, signal processing, and instrumentation use, all require electrical power. This section describes the subsystem responsible for converting and retaining solar energy. The thermal system could also be described as a subsystem of the power system, but it can be found in its own section.

8.6.1 Solar Cells

As stated, solar panels are an integral part of spacecraft power systems. They allow for sustainable energy generation, and they also can be purposed as radiators for the thermal system. From the initial summation of the power requirements for the instrumentation, propulsion, thermal, and refueling arm, the maximum total power is 1103.6 W. With this requirement, solar panel areas can be easily sized. Rocket Lab acquired a solar panel manufacturer named SolAero in 2022. SolAero has many types of optimized solar cells with efficiencies of around 30%, this is due to the use of germanium, which is 1-2 times more efficient than standard silicon solar cells [26].

Specifically, the ZTJ-Omega solar cell is promoted to be optimized for LEO environments and has a power per unit area of 408.2 $\frac{W}{m^2}$ [53]. This leads to an area of 2.70 m^2 for the solar array. With this solar cell, a solar panel or array can be constructed by adding many cells in parallel. Other options include specifying a particular solar panel, such that the manufacturing process would be less expensive. These germanium cells are expensive as well but are considered the current state of the art [54], and overall the ZTJ-Omega is the chosen

cell.

8.6.2 Batteries

For energy storage in orbit, since solar energy is not always accessible, a rechargeable battery is required; this is denoted as a secondary battery, whereas a primary battery is non-rechargeable. Common secondary battery types include nickel-cadmium, nickel-hydrogen, lithium polymer, and lithium-ion. The TITAN-2 L5 is a high-density lithium-ion battery matrix with a capacity of 2 $\frac{kW}{hr}$ [34]. Note that the required 1.1 kW requirement in the previous section is heavily influenced by an assumed 900 W for the refueling arm, which is informed by the CanadaArm power requirements. With a substantially smaller arm, the power requirement would also decrease with the required torque.

9 Mass Analysis

This section involves discussion of the mass distribution of the satellite. Commonly, the masses are divided up into three categories; propellant, payload, and structural.

9.1 Propellant Mass

The entire satellite is based around the value needed for the propellant mass. At each stage, 100 kg of hydrazine will be delivered to the customer. Additionally, the propellant needed to get from one location to the next must be determined. Section 9.4 explores this number through an average of many samples. Regardless of what the sample mission could produce, it's always important to have a very high ratio of propellant mass to the entire mass. [36].

9.2 Payload Mass

The term 'payload mass' is often times used to describe the most important object of a certain mission, whether that be instruments for a surveillance orbiter or astronauts on an extra-terrestrial multi-stage exploratory rocket. For this specific mission, the most important material objects are the shipments of hydrazine. Because this is also our propellant, the payload mass for this mission refers to the GNC instruments, Power Systems, and the refueling arm. Having a high payload mass ratio is also very important in order to accomplish a certain mission as effectively as possible. The payload mass was estimated to be around 325 kg, most of which is due to the arm.

9.3 Structural Mass

The structural mass of the satellite is everything else including beams and plates, propulsion elements, and the payload adapter. The type of mass is the easiest to change because there are so many variables. Changing the cross section of a certain beam can allow for less mass and overall better performance. This is just one example, and its something that varied after FE analysis. The refueler's structural mass was estimated to be around 1150 kg.

9.4 Sample Mission Results

The reason why Δv values were needed was to calculate the mass of the Refueler at each stage of a mission. Equation 12 shows how the initial mass was calculated from a final burnout mass of 1500 kg (the calculated structural and payload mass). The specific impulse of hydrazine is around 300 seconds. 100 kg is subtracted from the previous stage because the Refueler is delivering 100 kg shipments. A sample mission of 10 random test runs was conducted. This small number of runs was chosen solely based on processing power of the computer it ran on. These numbers were then averaged to show mass distributions of the average mission. The average mass from each stage is the last bar in each stage. The "11^{th} Stage" represents the final burnout mass, determined by the structural and payload masses.

$$m_i = m_{i+1} e^{\frac{\Delta v}{g I_{sp}}} - 100; \tag{12}$$

From this, a bar chart was generated with the mass of the satellite at each stage. This can be seen in Figure 34. Values are also shown in Table 13. The calculated average initial mass is just less than 7200 kg. This means that the initial average propellant mass of the satellite is around 5700 kg.

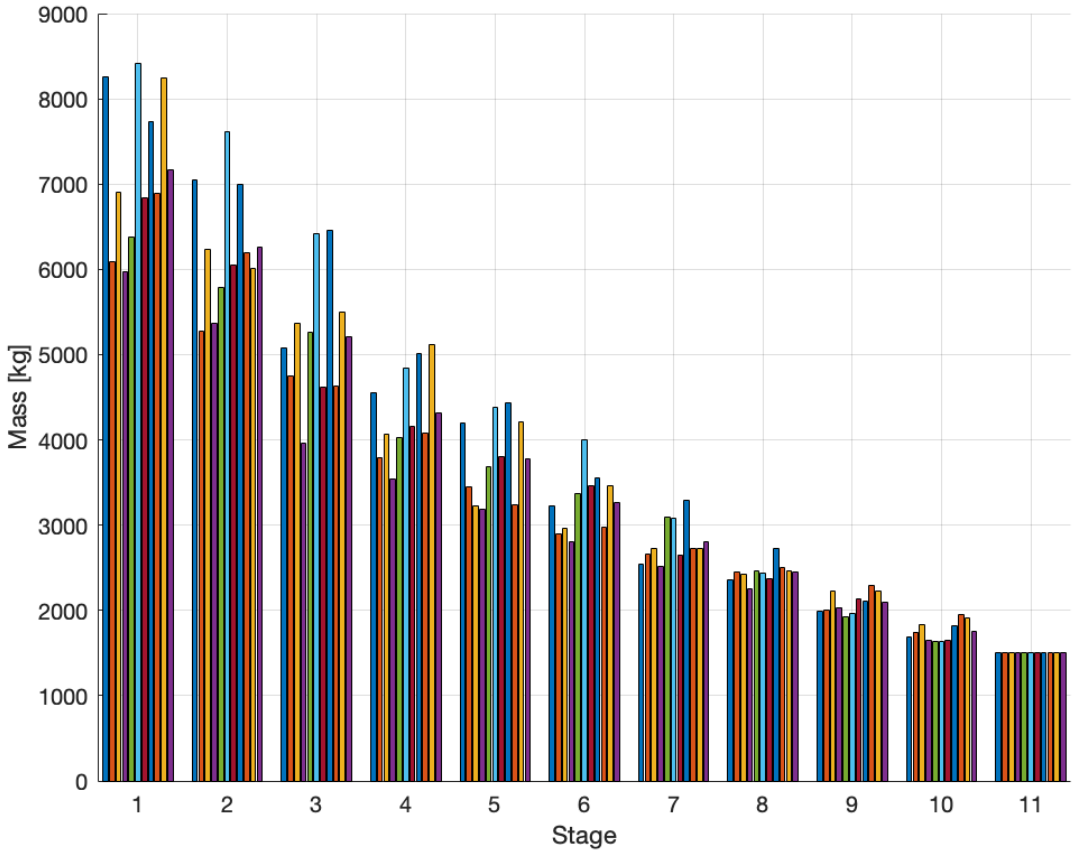

Figure 34: Mass of satellite at each stage of the mission over 10 test runs.

10 Refueling Apparatus Design

Four different design concepts were considered for the refueling apparatus. The refueling apparatus will be the method of transferring the hydrazine fuel from SpacExxon to other satellites. The four concepts that were considered were a direct connection, a robotic arm, a tethered drone, and a free-roaming drone. A direct connection would require movement and rotation of the entire satellite to line up a connection with another satellite in order to transfer the fuel. A robotic arm (3-6 axis) would allow for the satellite to reach out and rotate just the arm to make a connection. This would require more power, but it would be more fuel efficient, would increase the reach of the satellite, and reduce the maneuvering of the satellite as a whole. A tethered drone would essentially be a smaller satellite set out on a tether with a hose to make the connection to the satellite. This would also increase reach and fuel efficiency but would be more complex to navigate to make the connection. Lastly, a free-roaming tank drone would again be a smaller satellite sent out to make the connection and transfer the hydrazine. However, in this concept, the smaller satellite would have to carry enough fuel to move itself to and back from the satellite to be refueled. SpacExxon would not be maneuvering to satellites itself, but the smaller satellite would be.

A design matrix was created to help determine which design concept to move forward with. The three criteria that were considered were attachment range, fuel efficiency, and navigation complexity. All three of the criteria were given equal weight because they are all equally important to the success of the final design. The four concepts were then ranked one through four for each criterion. The scores were then totaled to determine which design to move forward with. The completed design matrix is shown in Table 4.

Table 4: Refueling manipulator design matrix.

	Direct Connection	Robotic Arm (3-6 Axis)	Tethered Drone Ejection	Tank Drone Ejection
Attachment Range	1	3	3	4
Fuel Efficiency	1	4	4	2
Navigation Complexity	1	3	2	2
Totals	3	10	9	8

The results of the design matrix suggest that the robotic arm is the best design. This is due to it not requiring any additional fuel to maneuver to make a connection, increasing the overall connection range of the satellite, and having the least complex navigational requirements.

One example of a robotic arm being used in an astronautical application is Canadarm on the Space Shuttle and Canadarm2 on the ISS. The Canadarm2 is shown in Figure 35. The robotic arm performs station maintenance, moves supplies and equipment, catches visiting vehicles, and brings them to the ISS [55].

Figure 35: Canadarm2 performs a connection with SpaceX's Dragon cargo ship [55].

The Canadarm2 sets a precedent for using a robotic arm in space, a similar concept can be applied to SpacExxon. Canadarm and Canadarm2 also provide a starting point in determining mass and power requirements for the robotic arm. From NASA data on Canadarm and Canadarm2, the mass of the robotic arm will be about 450 kg and the power required will be around 850 W [56]. Although Canadarm2 will likely need to be scaled down in size for use in the design of SpacExxon, it is nearly 60 feet long and requires a significant amount of power. Another off-the-shelf robotic arm could also be modified for use in space for the design of SpacExxon. The Canadarm and Canadarm2 simply provide a good baseline for determining mass and power requirements.

11 Preliminary Computer-Aided Design

Preliminary CAD is created for the satellite structure before performing structural and Finite Element Analysis (FEA) to assess the structural integrity of the design. The preliminary CAD provides an initial design that can be used to determine the general layout and geometry of the satellite. It provides a starting point for the structural analysis to ensure that it can meet the loading requirements.

FEA is used to analyze the structural behavior of a design under different loads and conditions. It provides detailed information about the stresses, strains, and displacements of the design. These can be used to optimize the design and ensure that it meets the required loading and safety factors. However, in order to complete FEA, a detailed and accurate model of the structure, including all the structural elements and connections, is required. Thus, completing preliminary CAD of the structure is required prior to beginning FEA to determine the geometry and sizing of the structural elements so that a useful finite element model can be created and analyzed. Overall, the preliminary CAD provides a valuable tool for designing the structure by allowing the creation of a finite element model that can be used in iterations of FEA analysis.

11.1 Structural Design

The general shape of the structure of the satellite was determined to be a hexagon because it creates triangular sub-frames and well contains the shape of our tank. A circular design was considered, but mounting the solar panels and manufacturing them to the circular frame would be much more complicated. The sizing of the satellite is largely determined by the size of the tank. The structure was designed to enclose the capsule-shaped tank as it is the largest component of the satellite by volume. The structure is made up of vertical support bars, a top subassembly, tank support bars, a bottom subassembly, and a payload adapter. An isometric view of the structure assembly is shown in Figure 36.

The material specified for the structural components of the satellite is Aluminium 2024 alloy. Aluminium 2024 alloy is favorable for aerospace applications due to its high strength-to-weight ratio. It was also chosen because high-strength aluminum alloys have been commonly used in spacecraft for decades [57].

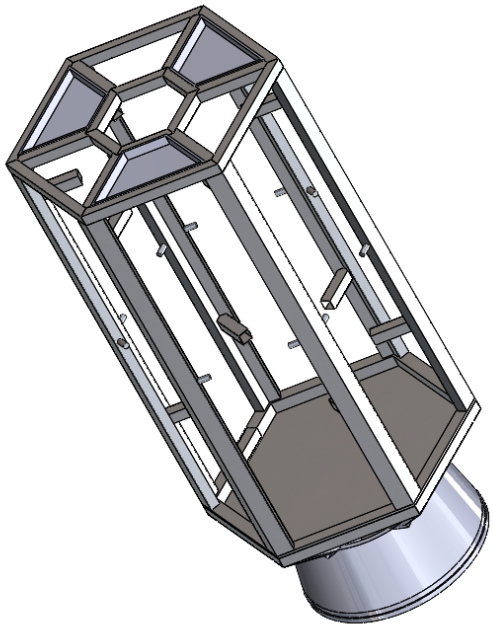

Figure 36: Structure assembly isometric view.

The top portion of the assembly is made up of one assembly of outer bars forming a large hexagon, another assembly of bars forming a smaller inner hexagon, crossbars connecting the two hexagons, and pocket inserts that fit into the gaps. The bottom subassembly consists of the same larger hexagon made up of bars with a plate inserted into the inside which will serve as a place to mount various components within the satellite. The vertical support bars match the shape of the corners of the hexagon design and connect the top and bottom subassemblies. Note that the cross-section of the vertical bars was created to match the corners of the hexagon design, not for structural or manufacturability reasons. This cross-section will likely need to be changed following structural analysis. The tank support bars are then attached to the inside of each of the vertical bars. Note that the exact location of the tank has not been determined because plumbing has yet to be created and the pressurant tank needs to be resized from the time that preliminary CAD was created. Another isometric view of the structure can be found in Figure 37, which gives a view of the bottom portion of the assembly.

The bottom portion of the assembly has tapered beams going from the larger hexagon design to a smaller hexagon assembly. The purpose of the tapered beams is to support the loading due to both launch accelerations and forces of the propulsion system, and to provide a place to mount the payload adapter. The propulsion system will be mounted on the smaller hexagon assembly inside the payload adapter. The payload adapter matches the dimensions given in Section 8.2.4. The cross sections of each of the bars in the structure assembly are hollow with a thickness of 0.01 m from each outer face. The thickness of the beams making up the hexagon assemblies is 0.1 m by 0.1 m, and the rest of the dimensions were created to match those. The length of the vertical bars is 3.75 m.

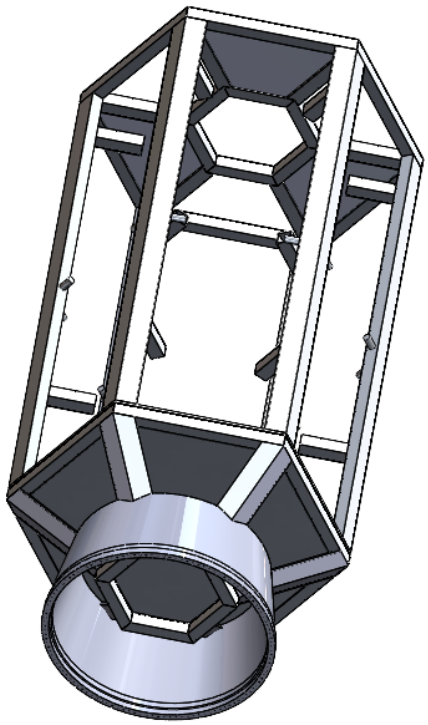

Figure 37: Structure assembly bottom isometric view.

11.2 Propulsion System Design

The propulsion system consists of main and RCS thrusters. Both types of thrusters will be bought from Moog Aerospace, a manufacturer and vendor specializing in high-performance aerospace control components and systems. These monopropellant thrusters also use hydrazine, the fuel that SpacExxon will deliver to other spacecraft.

11.2.1 Main Thrusters

The main thrusters will be the MONARC-445. These thrusters were chosen because of their high thrust (445 N steady-state) and low dry mass (1.6 kg). More data on the thrusters used can be seen in Table 5.

Table 5: Data from Moog on the thrusters used [35].

Engine	**MONARC-90LT**	**MONARC-445**
Steady-State Thrust (N)	90	445
Feed Pressure (psia)	80-370	70-400
Nozzle Expansion	40:1	50:1
Valve Power (W)	72	58
Mass (kg)	1.12	1.6
Engine Length (cm)	30	41
Exit Diameter (cm)	8.4	14.8
Specific Impulse (s)	232.1	234
Minimum Impulse Bit (N-s)	1.8	11.52
Total Impulse (MN-s)	2.042	5.6
Pulses	50,000	12,000

The MONARC-445 can be seen in Figure 11.2.1. A CAD model was constructed using data from Table 5.

Figure 38: MONARC-445 thruster.

Six MONARC-445 thrusters will be placed on the bottom of the satellite at each of the vertices of the tapered hexagonal structure.

11.2.2 Reaction Control System Thrusters

The RCS thruster is the MONARC-90LT. This thruster was chosen because it provides a large amount of thrust (90 N) with an angled nozzle. The board that the nozzle sits on also provides for a compact system that can be connected to the main structure easily. This thruster is from the same family as the MONARC-445 and its data can be seen in Table 5. There are two versions of the MONARC-90. The Refueler will use the lighter version to minimize structural mass. Figure 11.2.2 shows the MONARC-90LT. A CAD model was constructed using data from Figure 5.

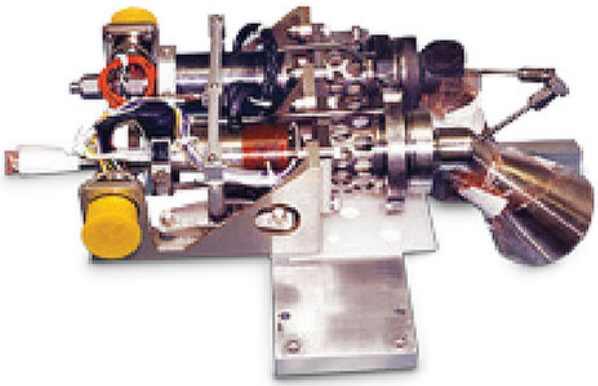

Figure 39: MONARC-90LT thruster.

Five MONARC-90LT thrusters will be placed on the structure to allow for impulses about the axis of symmetry as well as for plane changes. Impulses about the axis of symmetry will be very uncommon as the arm has a large angular reach. Plane changes will be very small ($\leq 2°$), and aren't a problem for the MONARC90-LT thrusters.

11.3 Tank Design

The tank assembly is made up of the hydrazine tank and the pressurant tank. The hydrazine tank is capsule-shaped and sized according to the calculations found in Section 8.3. The tank is created as a solid of revolution with the thickness found in Section 8.3. A ring is added on the top and bottom of the tank as a surface to mount the tank to the structure of the satellite. A spherical pressurant tank is created and attached to the tank with a pipe. The pressurant tank serves the purpose of pushing the hydrazine out of the tank to either the arm or the propulsion system. Note that the pressurant tank will need to be resized following plumbing calculations.

Figure 40: Tank assembly front view.

11.4 Refueling Arm Design

An important consideration at this point is designing the robotic arm. From the ground up, this section will cover the arm considerations that SpacExxon has taken.

11.4.1 Choosing an Arm Design

Robotic arms for space applications exist in many forms. The most important consideration in the design of the space arm for SpacExxon was the desire for an arm that simplifies the need for fine adjustments when arriving at a new satellite in terms of docking for refueling and also provides fuel via the arm. The arm is not looking to support a docking with satellites with large differences in velocity upon arrival. Additionally, the payload is already quite large. For this reason, a smaller arm is desired – the arm should add minimal weight and space desirably. After research, the options that were considered were a two-joint, three-joint, and a four-joint or greater arm - all with small linear actuators for fine adjustments.

11.4.2 Two Joint Arm Considerations

A new type of design that is possible is a rotational joint that has two joints and a linear actuator. This can be seen in Figure 41 where the first joint is located near the arm attachment to the spacecraft and the second joint is located where the arm bends. The linear actuator is placed at the end of the second arm. This design is unique in that the joint further from the base only has freedom of 45° rotation from the normal. This allows it to still

have moderate movement freedom (with movement capabilities in a cone-like range shown in Figure 41). Additionally, this design eliminates the need for more joints reducing complexity and storage space compared to traditional setups [58]. A downside of this, however, is that while the volume storage space is lower, the fact that it can only fold 45° means that the robot arm has limited folding capability which is illustrated in Figure 41. Additionally, the two joint approaches have a limited range of motion compared to those for arms with more joints, and since SpacExxon's satellite wants to make as few adjustments as possible, then it is certainly a large concern. Otherwise, the two-joint robot design is an exciting one that has many potential future use cases in space.

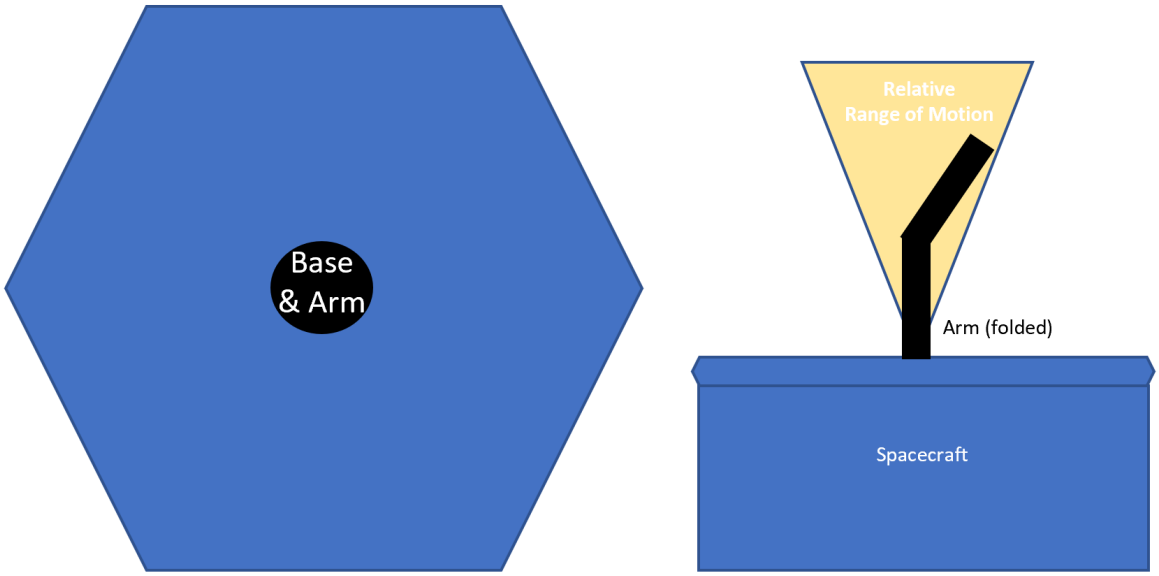

Figure 41: Visualization of the two-joint relative flexibility and fold-ability on the satellite.

11.4.3 Three Joint Arm Considerations

The most common type of arm used in satellite spacecraft is one with three motors and rotation points [59]. As displayed in Figure 42, this would involve the ability for the arm to rotate in a similar fashion to a human arm with one rotation around the "waist", "shoulder", and "elbow" axes. This is referred to as a three-joint robotic arm in the report.

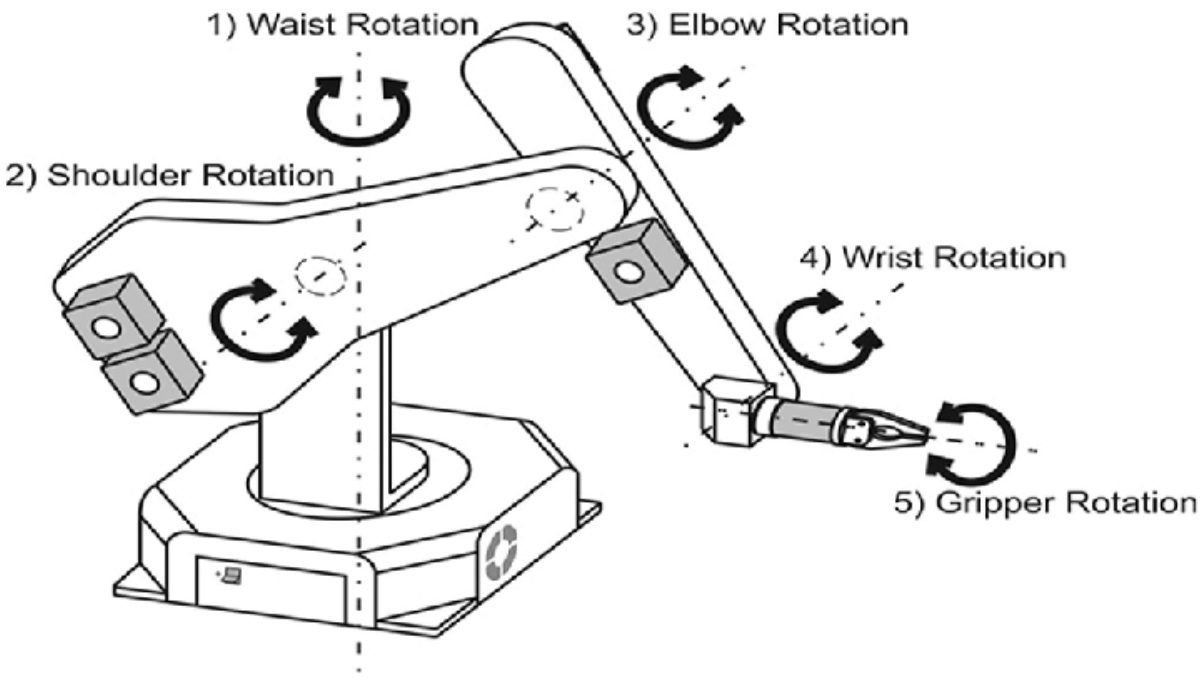

Figure 42: General robotic arm model [60].

A three-DOF robotic arm has a few advantages. First, they are commonly produced and well-studied - such that a control system already exists for sale and uses in purchased arms and software. SpacExxon is designing a custom arm and would expect to make the software itself; however, the three-DOF robotic arm could still be advantageous because there are many research articles describing the dynamics and manufacturing considerations of this type of arm which could reduce time spent on research and development.

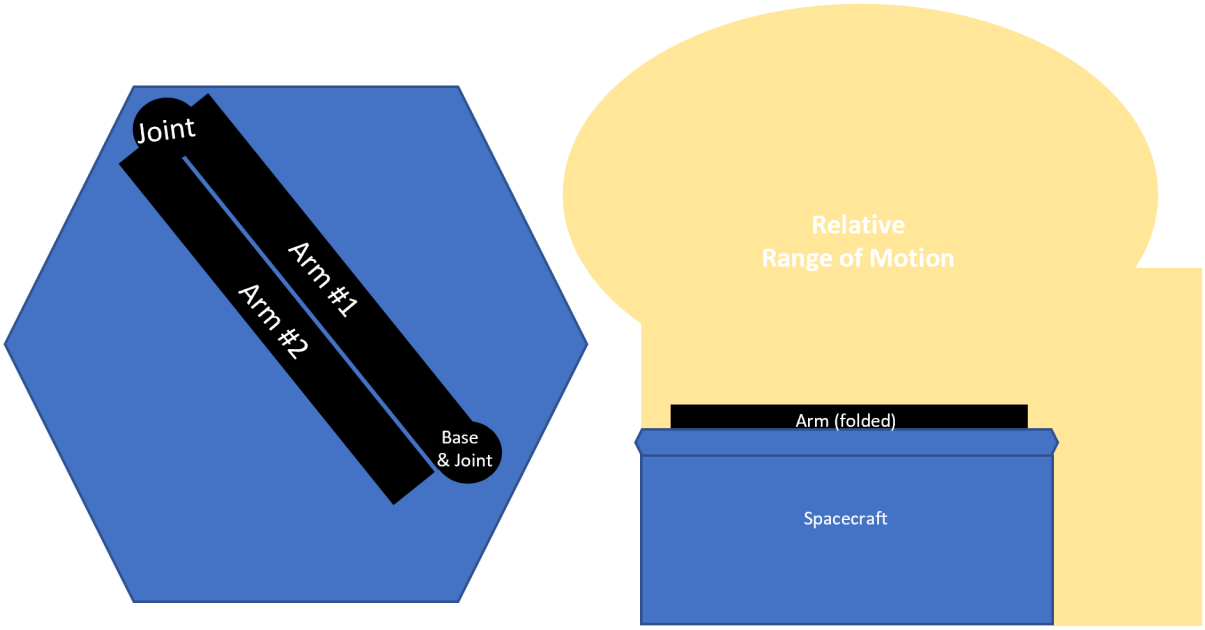

Figure 43: Visualization of the three-joint relative flexibility and fold-ability on the satellite.

On top of complexity, the three-joint robot is able to fold more than the two-joint system and therefore much more compact which is a large benefit for the satellite which is already long. With its foldability, it also offers more mobility and is, therefore, able to simplify other parts of the satellite. However, the addition of an extra arm means the design would weigh a considerable amount more than the two joint designs. Figure 43 illustrates two 2D views of the satellite system to show how the design arm would be able to fold during takeoff and also the relative range of potential motion in that it would be able to operate.

11.4.4 Four-Plus Joint Arm Considerations

In addition to a three-joint robotic arm, the other design option that was considered was a four or greater-joint robotic arm. Such an arm is similar to the functionality of a human arm if considering the wrist and fingers as well. An example of use in space is the Canadaarm2 shown in Figure 35 used on the ISS. For another reference, Figure 42 shows the design for what would be referred to as a 5-joint robotic arm.

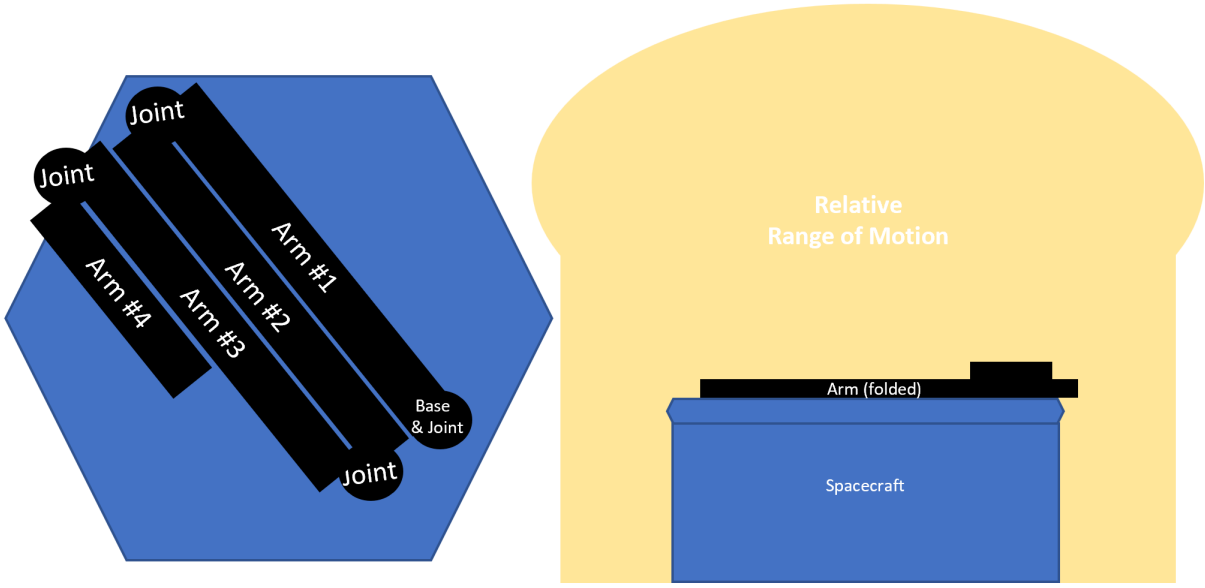

Figure 44: Visualization of the four-joint relative flexibility and fold-ability on the satellite.

The multiple joint designs offer the most mobility of all designs and are, therefore, able to simplify other parts of the satellite to the highest degree possible. However, this design comes at some costs. Because it involves more arms and the foldability is not exactly linear such as the three-joint design, it is not as foldable or compact on launch and it is quite a large design that would weigh more than the design requires. In addition, since there would be a fuel line the control system would have to be particular in the movements to make sure that it does not get tangled on multiple joints folding. Lastly, a design for this many joints would be quite complex, take a long time to make and develop, and as a result, be costly to design. At the moment, the refueling satellite is a one-time operation so minimizing manufacturing time and the cost is important.

11.4.5 Decision Matrix and Arm Design Decision

	CRITERIA KEY	RATING SCALE					
	Folding and Compactability	High = 5 to Low = 1					
	Mobility of Design	High = 5 to Low = 1					
	Complexity	Easy = 5 to Difficult = 1					
	Does it Simplify Other Parts?	High = 5 to Low = 1					
	Weight	Low = 5 to High = 1					
	CRITERIA	Folding and Compactability	Mobility of Design	Complexity	Does it Simplify Other Parts?	Weight	WEIGHTED SCORE
	WEIGHT	0.3	0.15	0.15	0.2	0.2	1
	%	30%	15%	15%	20%	20%	100%
DECISION	OPTIONS	CRITERIA 1 RATING	CRITERIA 2 RATING	CRITERIA 3 RATING	CRITERIA 4 RATING	CRITERIA 5 RATING	OPTION SCORE
✗	Two Joints (45 degree Cone DOF)	5	2	4	3	5	3.9
✓	Three Joints	4	4	5	5	4	4.2
✗	Four+ Joints	2	5	2	5	2	2.9

Figure 45: Decision matrix for joint design.

Figure 45 shows the decision matrix used for the arm design justification. As a result, it makes the most sense for the spacecraft to have a three-joint robotic arm because of its foldability, complexity, and mobility advantages. While it does not dominate all categories, it does not lack any necessary criteria and is the best overall arm design for the refueling satellite.

11.5 Three Degree of Freedom Arm Design

11.5.1 Relative Dimensions and Weight

The refueling arm will require some back-tracing to develop. To start, three versions of the arm were modeled in CAD to maximize the length of the arm while also minimizing the extra volume that it will occupy when folded in the spacecraft during launch. Because the spacecraft is designed to approach the other satellites with minimal differences in velocity, the structural integrity of the space arm is definitely a consideration – but not the major determinant for the original design. In future work, acceptable velocities and impact loads will be quantified to re-design the dimensions. For now, the first space arm dimensions were purely from a geometric and logical perspective in terms of structural stability and compatibility with the RAFTI refueling attachment which Orbit Fab uses. The relative design look can be seen in Figure 46. The RAFTI refueling attachment is 84 x 84 mm [5], so the arms cross-sections should be large enough to support it. Each of the two arms is made of Ti-6Al-4V for weld compatibility with the structure and weight considerations. To simplify the analysis, the arms are modeled in the analysis as tubes of length 1.25 m, an outer diameter of 100 mm, and a thickness of 5 mm. Therefore, each arm in this model weighs 4.23 lbs.

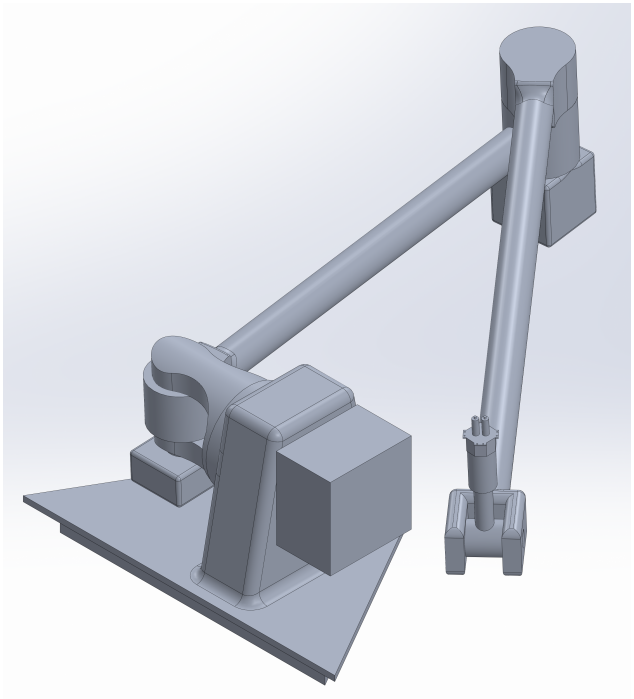

Figure 46: Preliminary design of the arm.

A preliminary version of the arm CAD can be seen in Figure 46. Something to note is

that the current version appears to have an extra joint of mobility at the end - this will be gone for the final version of the arm, it will only have three joints of rotation. Additionally, the base was rotated 90 degrees to allow for maximum folding of the design, although it will limit mobility slightly. However, this is acceptable because when folded, this design is extremely compact on the satellite. For now, the box structures are modeling a black box of the motors that will be on the arm. Lastly, the RAFTI refueling attachment can be seen in Figure 46 on the end of the arm for a reference for scale.

11.5.2 Torque and Motor Analysis

To determine how large the motors on each joint of the arm need to be in order to rotate out fully in a reasonable amount of time. The time is relatively arbitrary, since the orbit changes take lots of time and are highly structured the arm could, in theory, fold out slowly through the entire transit. However, it was decided that it is favorable to keep the arms folded when thrust changes are happening from an inertial and stress or vibrations on the robotic arms standpoint. Therefore, it was required to design the motor size around the arms folding out in the last few minutes of the trajectory toward the satellite. Specifically, in one minute. This section will examine the dynamics that was considered for a three-joint arm and finalize a selection of motors at each joint for the arm.

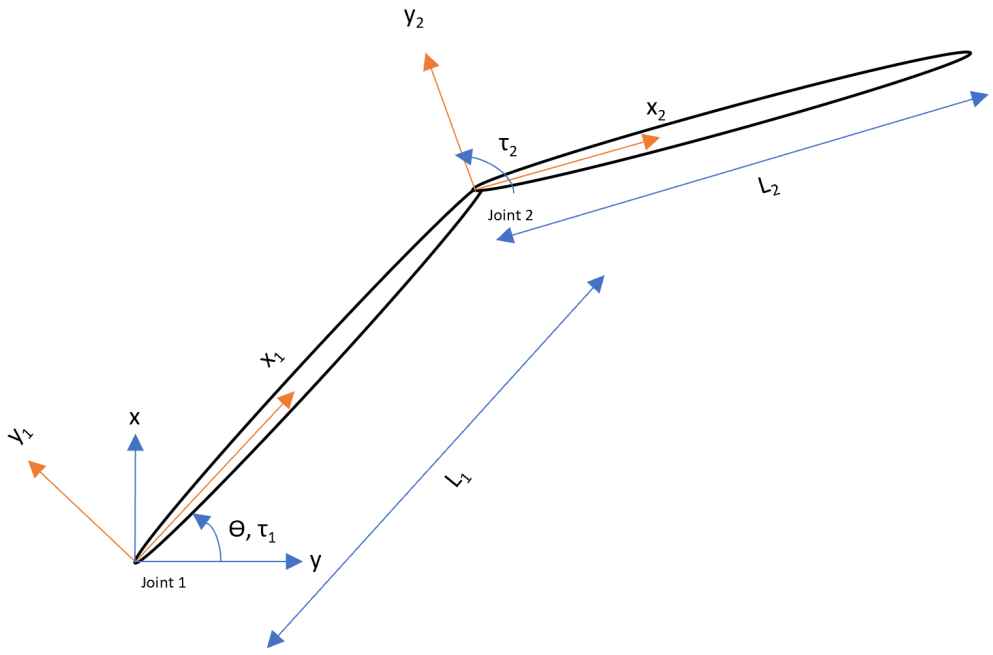

Figure 47: Two degrees of freedom robot dynamics diagram.

Since the first two motors are separated by a small moment arm around the same location of joint 1, the three-joint robotic arm dynamics can be simplified to an analysis of a 2-DOF Robotic arm as seen in Figure 47. In Figure 47, the missing motor would have the capability

to rotate about the x-axis. By the same logical assumption, the first two motors on the arm would require roughly the same torque from the analysis.

The design conditions of the arms are such that they should be able to fold out completely (a rotation of 180 degrees) in a minute (which will quantify $\dot{\theta}$ - the angular velocity - around joints 1 and 2). The arms in Figure 47 are modeled as two rods of continuous density and cross-section such that their center of mass lies at the midpoint of the rod's length. In Figure 47, τ_1 represents the torque required for the first two motors to complete this rotation, and τ_2 represents the torque required for the third motor to complete this rotation. L_1 and L_2 are measures of the length of the two rods.

In the absence of gravity, torque is still required to move the system. This is because angular acceleration will change the angular momentum (the vector product of a body's rotational inertia and rotational velocity) of the system, and as such, the moment around a point is derived from a combination of kinetic and momentum equations. The angular momentum at point A for an object (L_A) can be calculated, as shown in Equation 13, as related to the sum distance from A to the center of mass of an object ($\vec{r}_{j/a}$), the mass of the object (m_j), and the velocity of the object at its center of gravity relative to the velocity at A ($\vec{v}_{j/A}$).

$$\vec{L}_A = \sum \vec{r}_{j/A} \times m_j \vec{v}_{j/A} \tag{13}$$

And the resulting moment around that point is a function of the acceleration of A ($\vec{a}_A$), the distance from A to the center of the gravity of the system, the mass of the system (m_{sys}) and the change in angular momentum.

$$\sum \vec{M}_A = m_{sys} \vec{r}_{G/A} \times \vec{a}_A + \frac{d}{dt}(L_A) \tag{14}$$

Thankfully, Equation 14 simplifies when the point is a fixed point around where the rotation is happening (meaning no acceleration such as for joint 1 in Figure 47). It also simplifies when the system is only comprised of one object relative to the rotation such as the arm around joint 2 in Figure 47.

The relative velocity of point B with respect to A can be related to the angular velocity ($\dot{\theta}$) of the respective robotic arm in Equation 15.

$$\vec{v}_{B/A} = \dot{\vec{\theta}} \times \vec{r}_{B/A} \tag{15}$$

Lastly, the relative acceleration of point B with respect to A can be used to find the angular acceleration of the arm that the joint is connected to ($\ddot{\theta}$) for each respective robot arm in Equation 16. The equation is simplified because the first joint is a rigid body member attached to the spacecraft and as such has no relative acceleration compared to the spacecraft.

$$\vec{a}_{B/A} = \ddot{\vec{\theta}} \times \vec{r}_{B/A} + \dot{\vec{\theta}} \times (\dot{\vec{\theta}} \times \vec{r}_{B/A}) \tag{16}$$

Equations 13-16 were derived in class notes from Professor Sracic in Advanced Dynamics [61]. Using Equations 13-16, and checking with equations for controls of a 2 DOF robotic arm [59], the torque at joints one and two in Figure 47 are derived in Equations 17 and 18. The angle θ_2 represents the clockwise angle difference between arm sections 1 and 2.

$$\tau_1 = (\alpha + 2\beta cos(\theta_2))\ddot{\theta}_1 + (\delta + \beta cos(\theta_2))\ddot{\theta}_2 - \beta sin(\theta_2)\dot{\theta}_1\dot{\theta}_2 - \beta sin(\theta_2)(\dot{\theta}_1 + \dot{\theta}_2)\dot{\theta}_2 \tag{17}$$

$$\tau_2 = (\delta + \beta cos(\theta_2))\ddot{\theta}_1 + \delta\ddot{\theta}_2 + \beta sin(\theta_2)\dot{\theta}_1^2 \tag{18}$$

Where,

$$\alpha = 2I_z + m(1.5L^2) \tag{19}$$

$$\beta = \frac{1}{2}mL^2 \tag{20}$$

$$\delta = I_z + \frac{1}{4}mL^2. \tag{21}$$

Since the two rods are identical, the L, m, and I_z terms were simplified without reference to which mass, length, or inertia. The mass moment of inertia for both rods is that for a rod spinning around its end [40] is given in Equation 22.

$$I_z = \frac{1}{3}mL^2 \tag{22}$$

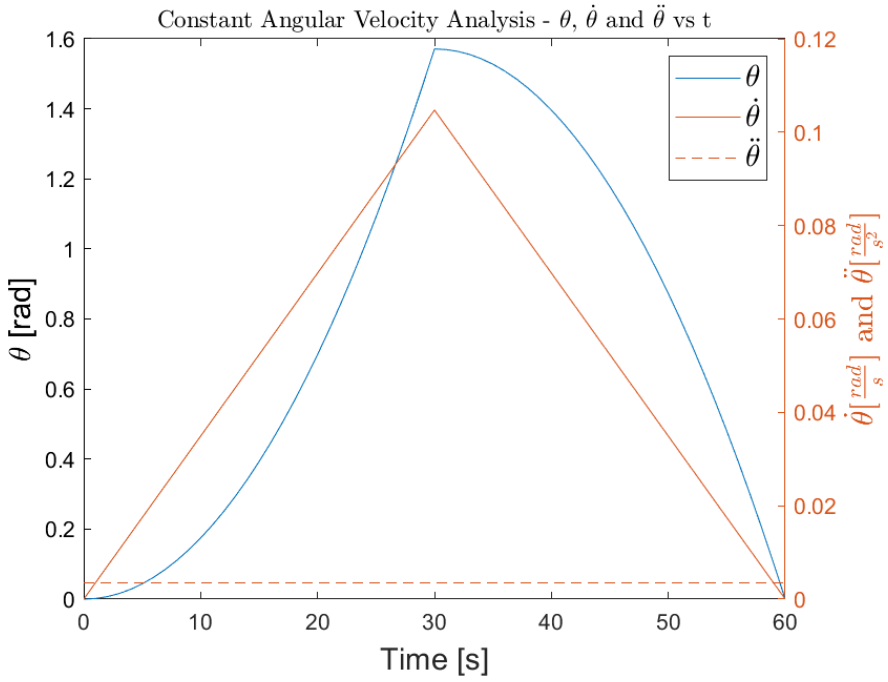

Figure 48: Plot of the movement for both arms in a constant angular acceleration case.

Figure 48 shows the angular movement of the two arms as they unfold during the constant acceleration analysis. The two extreme cases of unfolding happen when the arms start 0 degrees apart or 90 degrees apart - both of which will be explored to see if there are torque requirement advantages to folding out at the same time or separately.

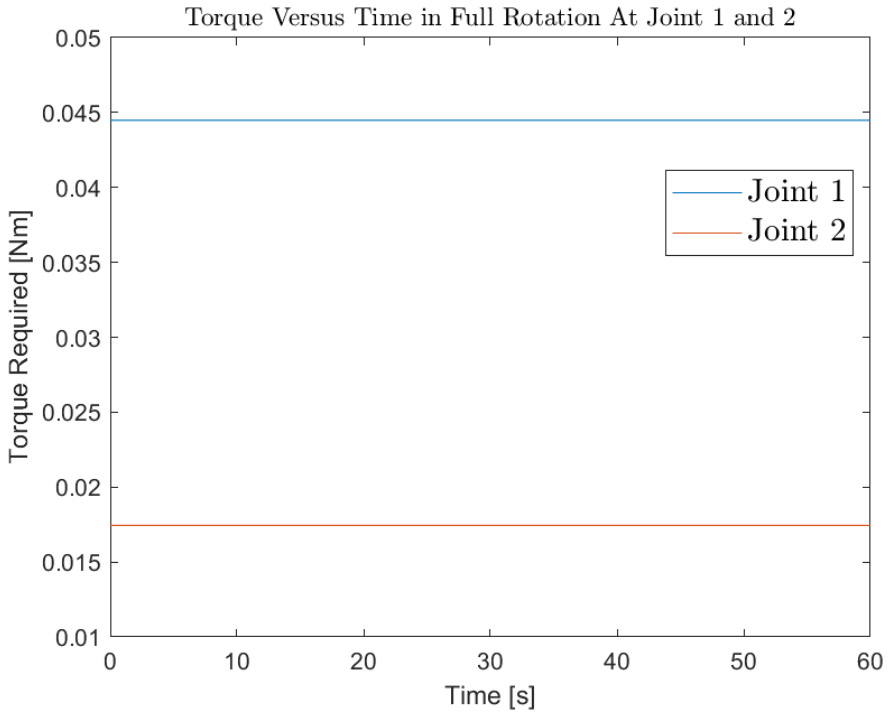

Figure 49: τ vs. t for joint 1 & 2 required for motion when both arms swing parallel.

Figure 49 shows the results of the torque required during the rotation of the system for its first full rotation around joints 1 and 2 when the arms swing perfectly parallel. When the arms swing together, the mass moment of inertia is maximized for joint 1, and fascinatingly Equations 17-18 for torque requirements joint 1 and 2 results in a constant torque required because they are only related to the angle difference and angular acceleration - which remain constant. The analysis also results in an important discovery - the torque requirements for the motion are quite small - peaking at less than 0.045 N-m.

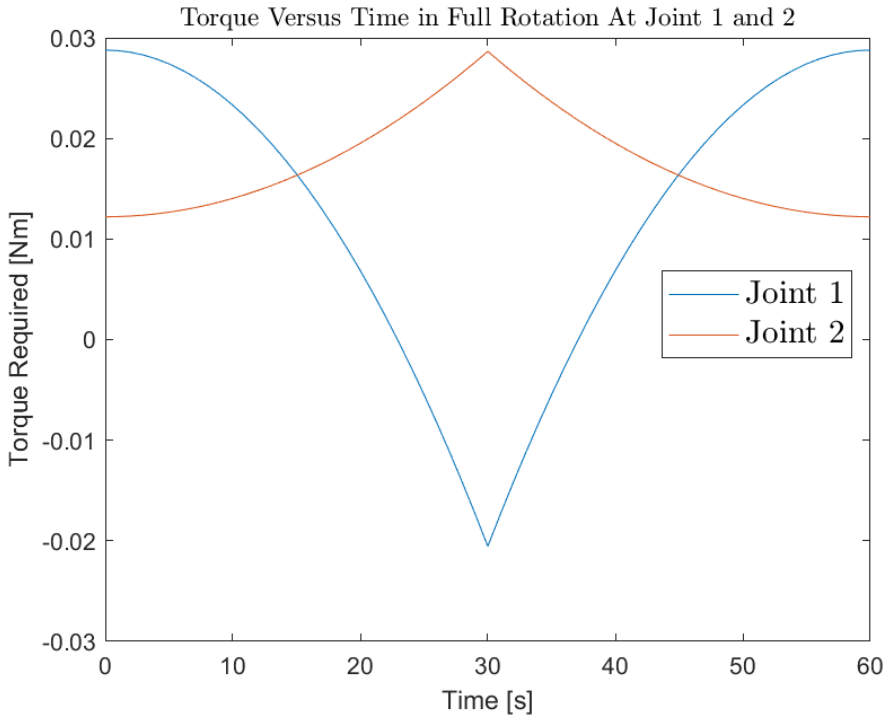

Figure 50: Torque vs. time for joints 1 and 2 required for motion when arms swing perpendicular to each other.

Figure 50 shows the results of the torque required during the rotation of the system for its first full rotation around joints 1 and 2 when the arms swing perfectly perpendicular to each other. Unlike when the arms are parallel, the torque requirements change with rotation. The maximum torque requirements are also lower than those required when the arms swing parallel together for joint 1 but are more than ten times greater for joint 2 - peaking at approximately 0.03 N-m each. This could be because the angular momentum of the second joint is positively helping joint 1 rotate from a dynamics perspective. This is also interesting because this could help the spacecraft optimize a rotation foldout if it were interested in minimizing motor size and weight. For now, the 0.03 N-m is small to the point of a non-factor, but it opens up the eyes to other types of optimizations that could be done with the motors. The MATLAB code used for this analysis is provided in the Appendix Section 19.4.

Usually, motors provide constant torque to the member attached to it. Therefore, an analysis was performed where the constant known were the values of torque instead of angular acceleration to check the results of the constant acceleration case and also so that the design could use it later to accurately predict arm movement from motors providing constant torque. This was done using small time steps and linearly interpreting Equations 17 and 18 to solve for angular acceleration and velocity at each time step. The full analysis and code is provided in the Appendix Section 19.5. The code provides a range of motion then for the two arms with factors that one can change to be specific to the arm such as torque, mass, total time and time steps, and initial angles. An example of this is to use the torque obtained in the constant angular acceleration case in Figure 49, which had a constant torque, and see if the motion between two arms is similar.

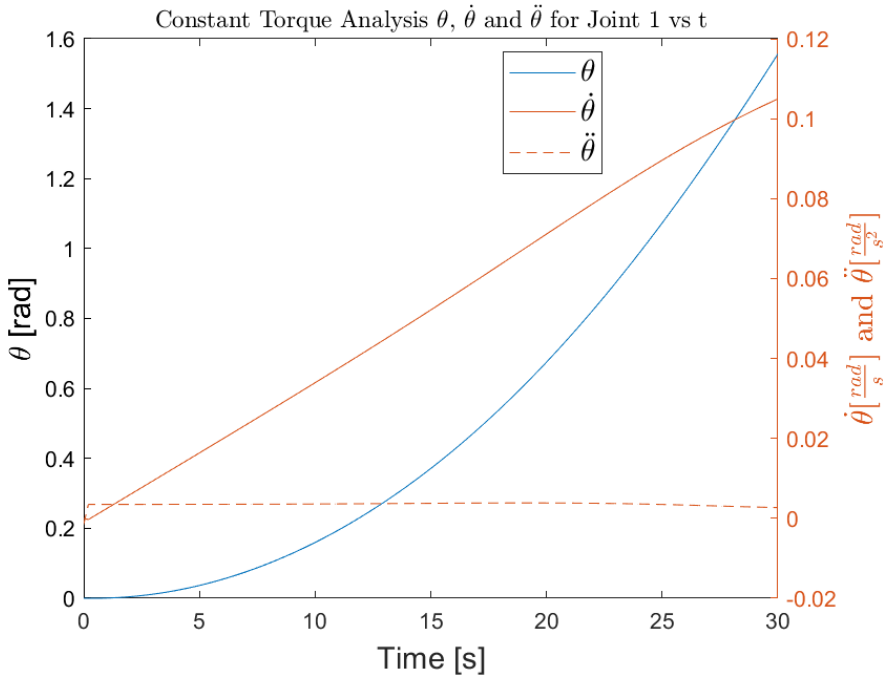

Figure 51: Angular terms for joint 1 in the constant torque case.

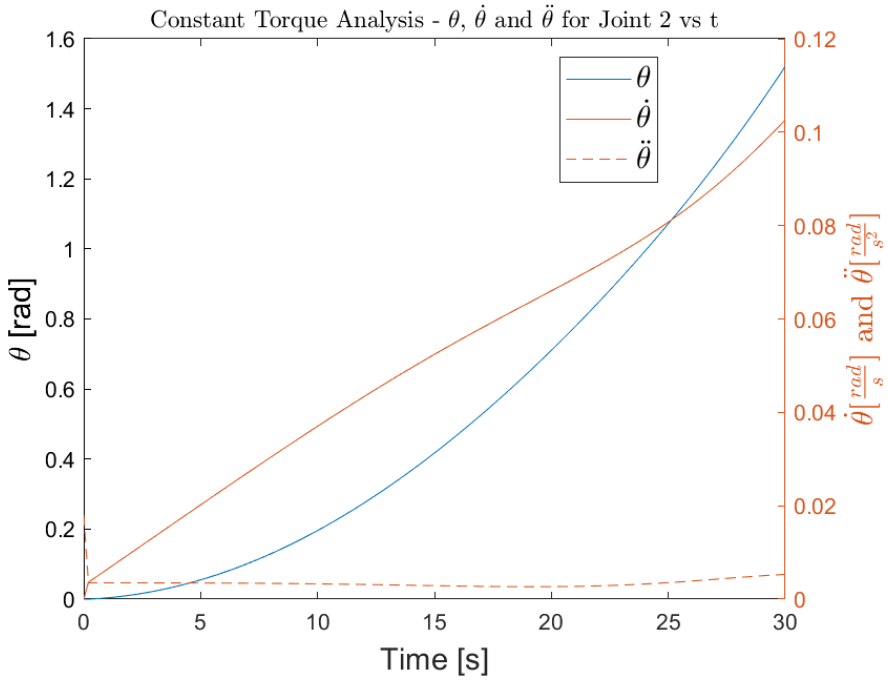

Figure 52: Angular terms for joint 2 in the constant torque case.

When the torque values from Figure 49 were used, the two arms appear to be swinging together in an almost perfect parallel motion during the entire 90-degree rotation - exactly as predicted as indicated by Figures 51 and 52. However, not all cases are this easy. When trying values by guess-and-check, even the smallest change in torque or starting position drastically changed the motion of the two arms. When trying to predict the motion of an

arm, there should be a plan to use the analyses of constant acceleration with appropriate starting angles as a baseline for reasonable torque or time values. Then, a guess-and-check approach or more sophisticated algorithm could be used to find the best time to activate each motor. Alternatively, and more practically, the motors could utilize a magnetic robotic joint capable of locking rotation when the motors are not activated. This type of approach would take longer to fold out, but most likely lead to more reliable movement. This is because only one arm is moving at a time. Time is not the greatest concern because the torque requirements so far are proving to be extremely small. If time were a concern when the torque is so low, the design could be upped easily to double the torque and have the rotation happen faster.

11.5.3 Friction Considerations

The torque requirements in terms of angular momentum in space were quite low in the specified requirements for movement. There was further motivation to see if the friction - specifically from the bearings - is a major contributor to the torque required for rotation.

In order to get a value of friction data, some rough assumptions must first be made on the bearing size and bearing pre-load exists in to determine how much torque is lost to friction. Based on the results from Section 11.5.2, the spacecraft used Moog's motors catalog to find motors that could fit the job. Moog is an American designer of systems for applications in aerospace. For their brushless motors below 900 W, the shaft diameters of those motors were typically in the range of $0.5m$ in diameter [35]. In addition to Moog, servo motors were also considered at varying sizes on commercial sites. Since the arm is folding out slowly at a rate of less than one rpm, the motors searched for can utilize a high gear ratio to maximize torque and minimize power requirements. An example of such a servo motor can be purchased on Amazon such as STEPPERONLINE's three N-m servo motor that utilizes only 11.1 W at maximum output - a great result because original estimates for the arm totaled 425 W for the power requirements before considerations of a high gear ratio motor. This servo motor was also in a reasonable range for diameter size [62]. So, roughly, the average between the inner and outer diameter size of a bearing attached to it would be 0.6 in diameter. Bearings of this size could be approximated to have at most 100 lbs of pre-load in them. It should be noted that extensive searching online gave no indication of bearing pre-load, so this is the best design decision based on physical intuition. If done extensively, a Hertzian contact setup could tell exactly give the full answer to how much pre-load exists in these bearings.

The most common type of ball bearing to use is a roller bearing. A rough calculation for a coefficient of friction (μ) for normal operating conditions and favorable lubrication is listed as 0.0018 from both Mark's Standard and also Machine Design [63] [64]. This should be especially noted because lubrication is generally not as good in orbit as it is on Earth. Equation 23 relates the horsepower lost due to frictional torque from a bearing design.

$$hp = \frac{T_f n}{63025} = \frac{\mu_f F_r d_{bb} n}{126050} \tag{23}$$

Where T is the frictional torque, n represents the shaft speed, d represents the bearing bore (0.6 in approximation), and F_r represents the radial bearing load (100 lbs approximation). From Equation 23, this results in an estimated torque lost to the friction of 0.045 lb-in, or about 0.005 N-m. Compared to the results from section 11.5.2 from the mass-moment-of-inertia torque required, this is not entirely a non-factor, as evident from the analysis in

Figures 49 and 50, so they should be accounted for if the arm is still to be so light and the arm foldout so slow. The Machine Design book predicts that the frictional torque loss would be insignificant in many designs, but clearly, this design should be aware of the potential impact [64].

Based on the analysis, the spacecraft would need to re-approach this analysis in the future to size the motors to the robotic arm when specifications for impact load, the maximum time to unfold, and unfolding and folding technique are finalized. For now, it could be said that any motor between 0.05 and 1 N-m is acceptable since the weight, size, and power requirements of these motors are relatively small (<1 lbs in weight each) [35].

11.6 Preliminary Spacecraft Assembly

The full preliminary CAD assembly of the SpacExxon spacecraft is shown in Figure 53. The full assembly includes the structure assembly with the tank mounted inside, solar arrays with control arms, the refueling arm with a mount, the propulsion systems, and various other components mounted to the lower plate. Note that not all of the internal components such as plumbing and Whipple shielding of the spacecraft are included in the preliminary full assembly. However, these components are not important for structural analysis and, therefore, are not the most important to be included at this point.

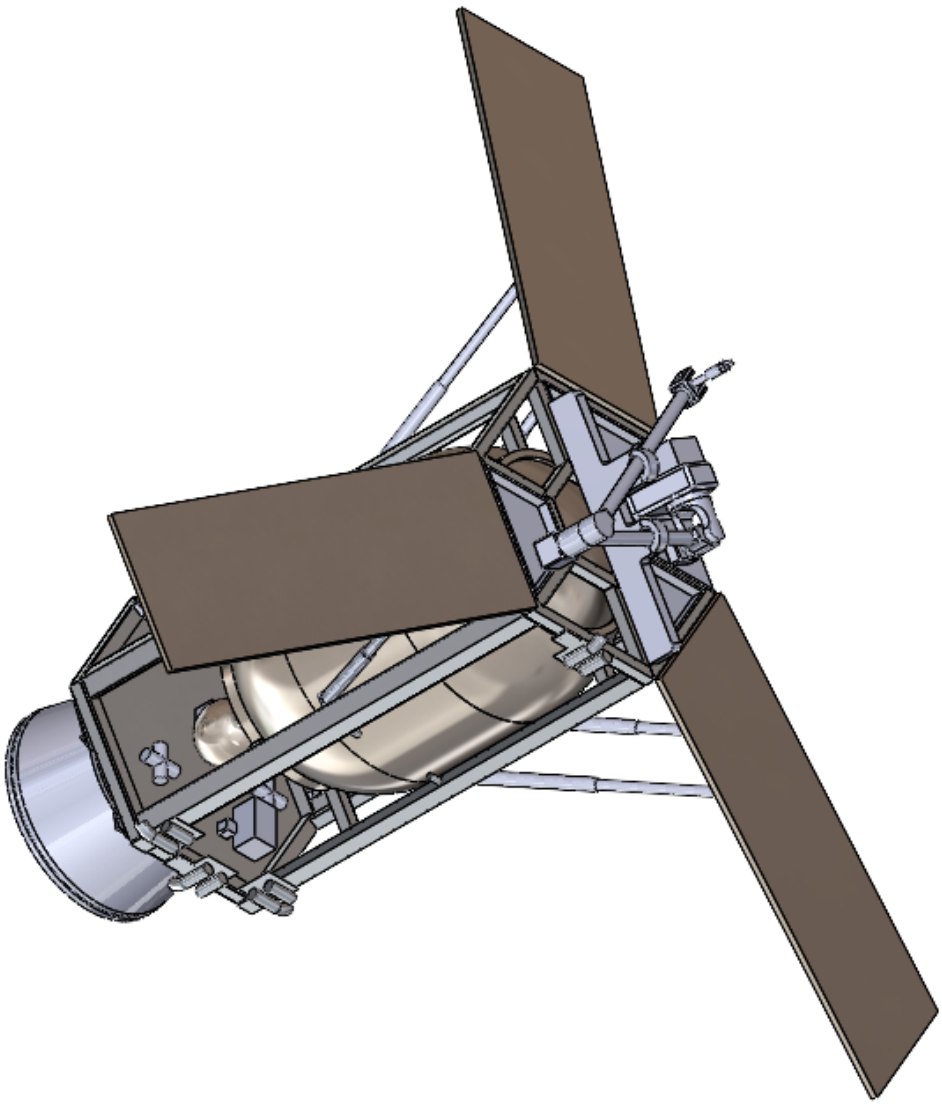

Figure 53: Full spacecraft assembly isometric view.

Figure 54 displays the top portion of the full spacecraft along with the refueling arm. The base of the refueling arm is mounted to the top portion of the spacecraft inside of the area between the inner and outer hexagonal design. The refueling arm is also mounted to the top of the spacecraft at two different points along the arm. This second mounting is meant to hold the arm in place during launch. This amount would then be released after separation from the launch vehicle to allow the refueling arm to move freely and connect with other satellites. The solar arrays can swing and be manipulated with the control actuators, they are shown in a fully deployed position.

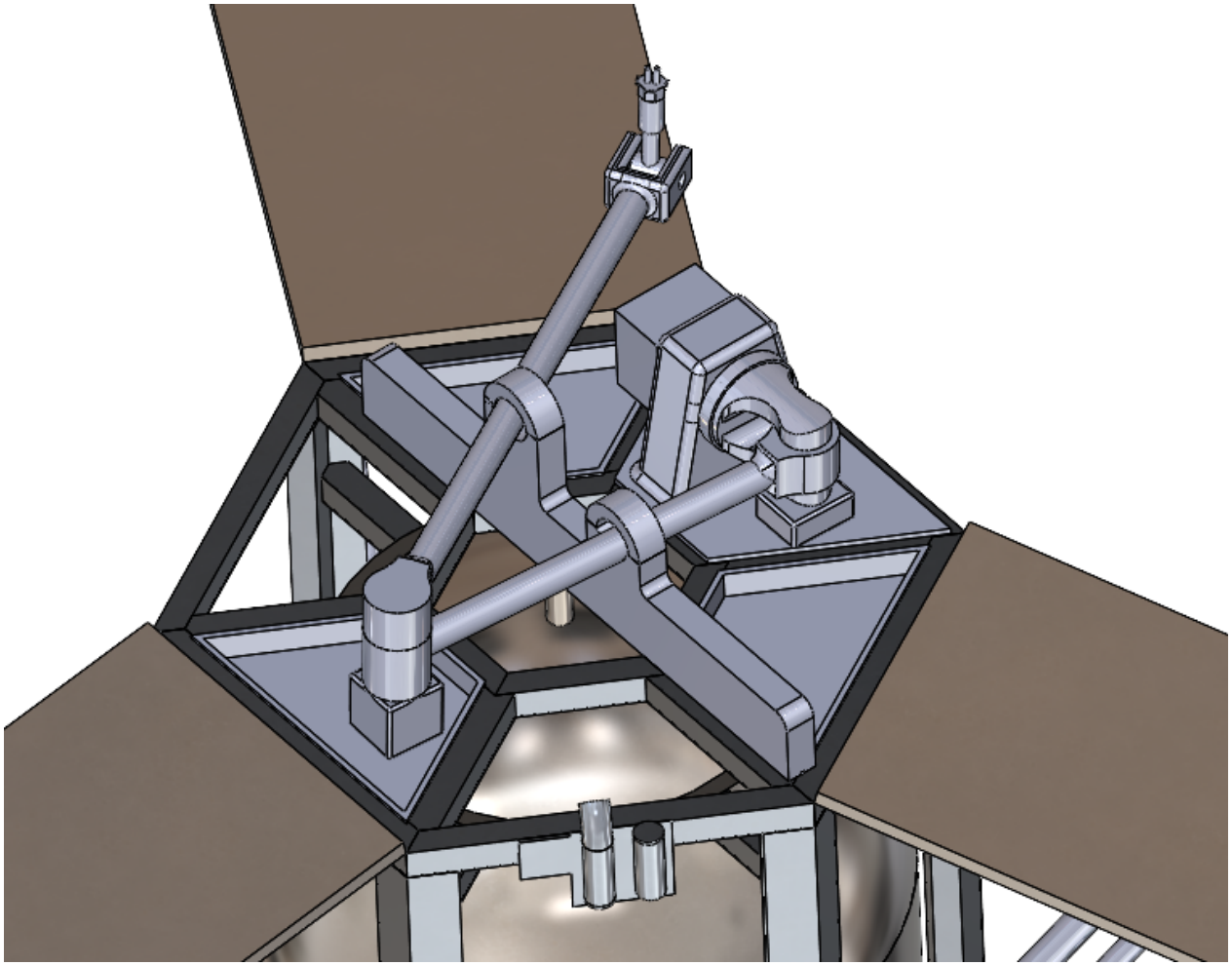

Figure 54: Full spacecraft assembly refueling arm and mount.

Another view of the full spacecraft assembly is shown in Figure 55, which displays the bottom of the spacecraft and the propulsion system. The propulsion system is made up of four RCS thrusters for attitude control of the spacecraft and six main thrusters. The six main thrusters are mounted on the bottom of the spacecraft on a small hexagonal assembly of bars inside the payload adapter. Three of the RCS thrusters are mounted on the side of the spacecraft towards the bottom and one is mounted towards the top of the spacecraft. The location of the connection between the solar arrays, the control arms, and the structure all can also be seen in Figure 55.

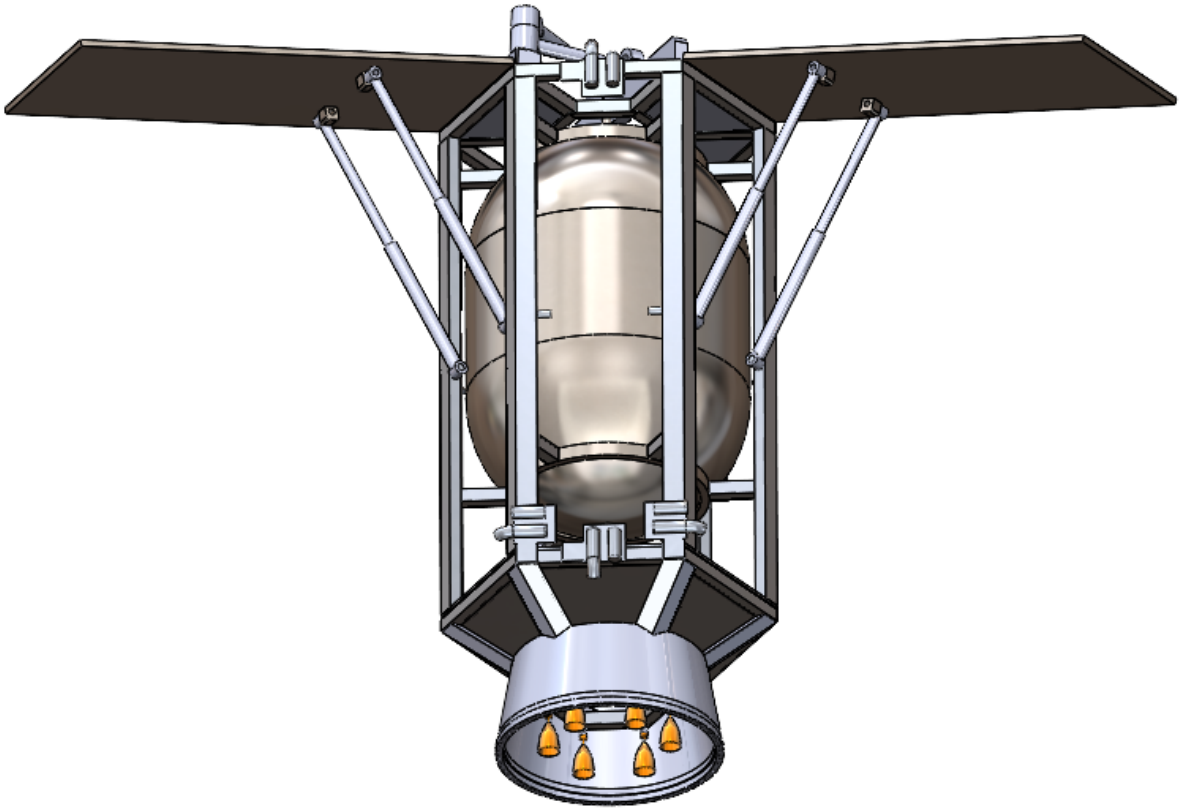

Figure 55: Full spacecraft assembly propulsion system and bottom.

12 Structural Analysis

In order to accurately predict the structural behavior of the satellite during launch and orbital operations, analysis techniques must be used to inform design decisions and protect against failure. The following subsections contain information about the Finite Element Model (FEM) and results generated through the simulated application of loads in Finite Element Analysis. Specifically, analyses of the static launch accelerations, the launch modal environment, and propulsion loads. For trivial cases, the results from the finite element models will be compared to theoretical calculations.

12.1 Static Analyses

This subsection analyzes the simulated structural loads from two scenarios, launch, and propulsion.

12.1.1 Analytical Calculations

Before running FEA, it is important to perform hand calculations to find stresses and ensure that the FEA results are accurate. By performing hand calculations prior to running an FEA, the accuracy of the FEA results can be verified. The following hand calculations were completed for this purpose.

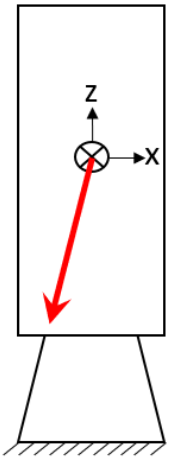

Figure 56: Side view of the lateral plane.

First, the reaction forces during launch conditions were found. According to figure 14, the maximum equivalent static loading for the spacecraft during the launch is a 6g axial load and 0.5g axial. This loading condition is shown in Figure 56. The distance from the fixed end to the CG is $L = 3.1$ m, and from the most recent CAD assembly, the mass of the spacecraft is $m = 7172$ kg.

Using Newtonian Mechanics, the sum of the moments and the sum of the forces can be found to be equal and opposite of the reaction forces at the base of the structure.

$$\sum \vec{M} = \vec{r} \times \vec{F} = (3.1\hat{\mathbf{k}}) \times (-0.5gm\hat{\mathbf{i}} - 6\text{mg}\hat{\mathbf{k}}) \text{ Nm} \tag{24}$$

$$M_R = 1.478 \times 10^5 \text{ Nm} \tag{25}$$

$$\sum \vec{F} = m\vec{a} = (-6\text{mg})\hat{k} - (0.5mg)\hat{\mathbf{i}} \; N \tag{26}$$

$$\vec{F} = -4.77 \times 10^4 \; \hat{\mathbf{i}} - 5.723 \times 10^5 \; \hat{\mathbf{k}} \; N \tag{27}$$

Maximum Value Over Time	
X Axis	8.0408 N
Y Axis	48487 N
Z Axis	5.8331e+005 N
Total	5.8532e+005 N

Figure 57: Ansys results for base reaction force.

It can be seen that the analytical calculations of the reactions are within 2% of the results in Figure 57. This is a sanity check to ensure the proper assembly of the FEM.

Next, the tapered beams were modeled as an angled beam bending problem to solve for stresses. A sketch of the problem is shown in Figure 58 with $F = 445$ N, $\theta = 37.24°$, and $L = 0.56$ m.

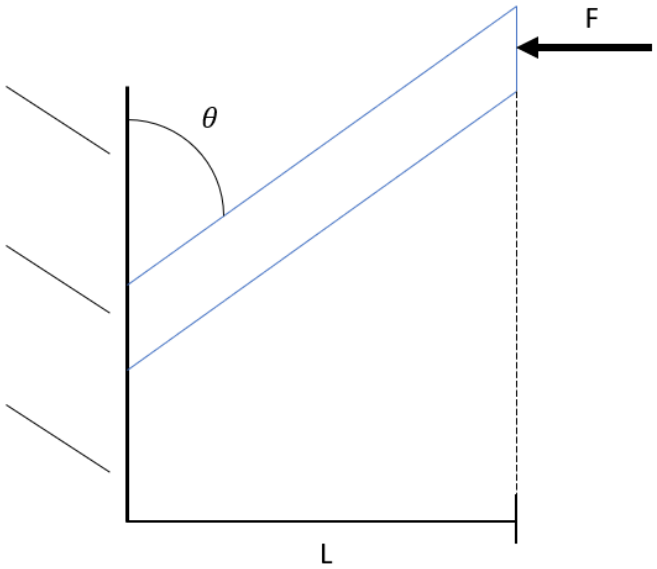

Figure 58: Sketch of angled beam bending problem.

The cross-section of the beam is a hollow square with an outer side length of 0.08 m and an inner side length of 0.06 m. This gives a thickness $t = 0.01$ m and a cross-sectional area of 0.0028 m^2. The yield stress of Ti-6Al-4V (σ_{yield}) is 1100 MPa [42]. The forces at the fixed end are found in Equation 28.

$$\begin{aligned} F_x &= F\cos\theta = 354.3 \text{ N} \\ F_y &= F\sin\theta = 269.3 \text{ N} \\ M_z &= LF\sin\theta = 150.8 \text{ N-m} \end{aligned} \tag{28}$$

The stress due to the axial force is found in Equation 29. The stress due to bending is found in Equation 30 with $I = 3.75 \times 10^{-6}$ m^4. The stress due to shear is found in Equation 31 with $Q = 6.4 \times 10^{-5}$ m^3. The principle stresses are then found in Equation 32, which are $\sigma_{1,3}$ due to the forces being in a plane.

$$\sigma_x = \frac{F_x}{A} = 126524 \text{ Pa} \tag{29}$$

$$\sigma_y = -\frac{M_z y}{I} = -1608580 \text{ Pa} \tag{30}$$

$$\tau_{xy} = \frac{F_y Q}{It} = 459595 \text{ Pa} \tag{31}$$

$$\begin{aligned} \sigma_{p1,2} &= \frac{\sigma_x + \sigma_y}{2} \pm \sqrt{\left(\frac{\sigma_x - \sigma_y}{2}\right)^2 + \tau_{xy}^2} \\ \sigma_1 &= 240743 \text{ Pa} \\ \sigma_2 &= -1.7228 \times 10^6 \text{ Pa} \\ \tau_{max} &= \sqrt{\left(\frac{\sigma_x - \sigma_y}{2}\right)^2 + \tau_{xy}^2} = 981771 \text{ Pa} \end{aligned} \tag{32}$$

For Tresca/max shear failure criteria, there is a failure when $\sigma_1 - \sigma_3 = \sigma_{yield}$. For Von Mises/distortion energy, there is a failure when $\sigma_{yield}^2 = \frac{(\sigma_1-\sigma_2)^2+(\sigma_2-\sigma_3)^2+(\sigma_3-\sigma_1)^2}{2}$. Yield should not occur in either case as shown in Equation 33.

$$\begin{aligned} \sigma_1 - \sigma_3 &= \sigma_{yield} \\ 1.96354 \times 10^4 \text{ Pa} &< \sigma_{yield} \\ \sigma_{yield}^2 &= \frac{(\sigma_1 - \sigma_2)^2 + (\sigma_2 - \sigma_3)^2 + (\sigma_3 - \sigma_1)^2}{2} \\ \sigma_{yield}^2 &= 1.21 \times 10^{18} \text{ Pa}^2 > 3.44074 \times 10^{12} \text{ Pa}^2 \\ \sigma_{yield} &= 18.5 \text{ MPa} \end{aligned} \tag{33}$$

Another hand calculation that was completed to verify the FEA results was for the plate holding the tank assembly in place. This can be modeled as a force on a hole in a plate. The force is found according to the mass of the tank and acceleration during launch. The stresses in the plate are found according to Roark's Formulas for Stress and Strain [65] in Equations 34 through 42. The plate is approximated as circular for the calculations. An image of the loading is shown in Figure 59.

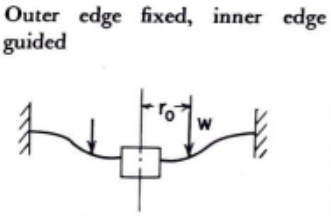

Figure 59: Model of tank mounting plate loading [65].

$$\begin{gathered}\text{Plate radius: } a = 1.03 \text{ m} \\ \text{Hole radius: } b = 0.71 \text{ m} \\ \text{Poisson's ratio: } v = 0.3 \\ \text{Plate thickness: } t = 0.02 \text{ m} \\ \text{Mass of the tank: } m = 1234.85 \text{ kg} \\ \text{Unit line load: } w = 2.71556 \times 10^3 \text{ N/m}\end{gathered} \tag{34}$$

$$C_5 = \frac{1}{2}\left(1 - \left(\frac{b}{a}\right)^2\right) = 0.2624 \tag{35}$$

$$C_8 = \frac{1}{2}\left(1 + v + (1-v)\left(\frac{b}{a}\right)^2\right) = 0.8163 \tag{36}$$

$$L_6 = \frac{b}{4a}\left(\left(\frac{b}{a}\right)^2 - 1 + 2\log\left(\frac{a}{b}\right)\right) = 0.0378 \tag{37}$$

$$L_9 = \frac{b}{a}\left(\frac{1+v}{2}\log\left(\frac{a}{b}\right) + \frac{1-v}{4}\left(1 - \left(\frac{b}{a}\right)^2\right)\right) = 0.2300 \tag{38}$$

$$M_{rb} = \frac{wa}{C_5}L_6 = 402.73 \text{ N-m} \tag{39}$$

$$M_{ra} = -wa\left(L_9 - \frac{C_8 L_6}{C_5}\right) = -314.58 \text{ N-m} \tag{40}$$

$$\sigma_{ra} = \frac{6M_{ra}}{t^2} = -4.7187 \times 10^6 \text{ Pa} \tag{41}$$

$$\sigma_{rb} = \frac{6M_{rb}}{t^2} = 6.0409 \times 10^6 \text{ Pa} \tag{42}$$

Finally, the stresses are plotted as a function of thickness in Figure 60. The current values are circled on the plot.

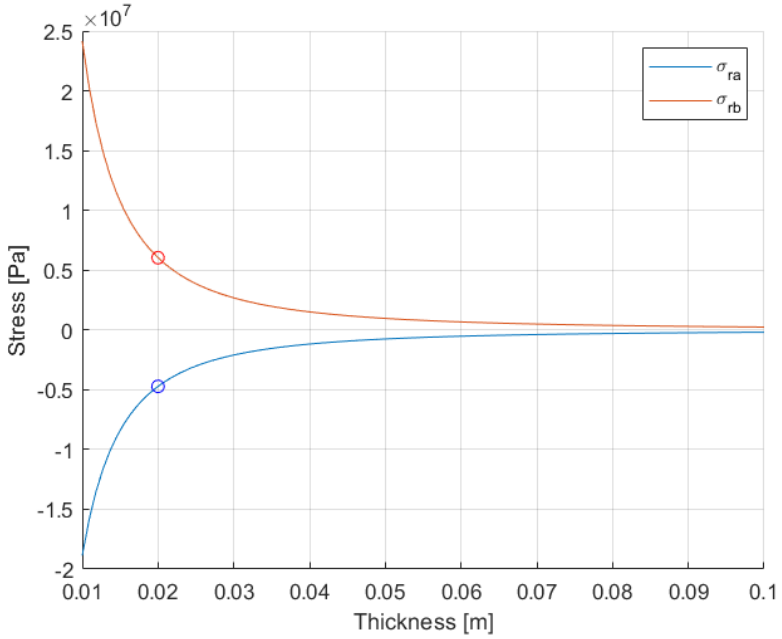

Figure 60: Stresses on the tank plate as a function of thickness.

12.2 Finite Element Model

The finite element model was generated by importing the profiles of integral geometry from the full spacecraft assembly. To define "integral" geometry, the main structure assembly, the tank, the pressurant tank, and the payload adapter were considered. The arm was not included in the FEM to decrease model computation time, and it is not a rigid structural member that impacts the stiffness of the entire structural assembly. Figure 61 shows the geometry in Ansys DesignModeler to mesh in Ansys Mechanical.

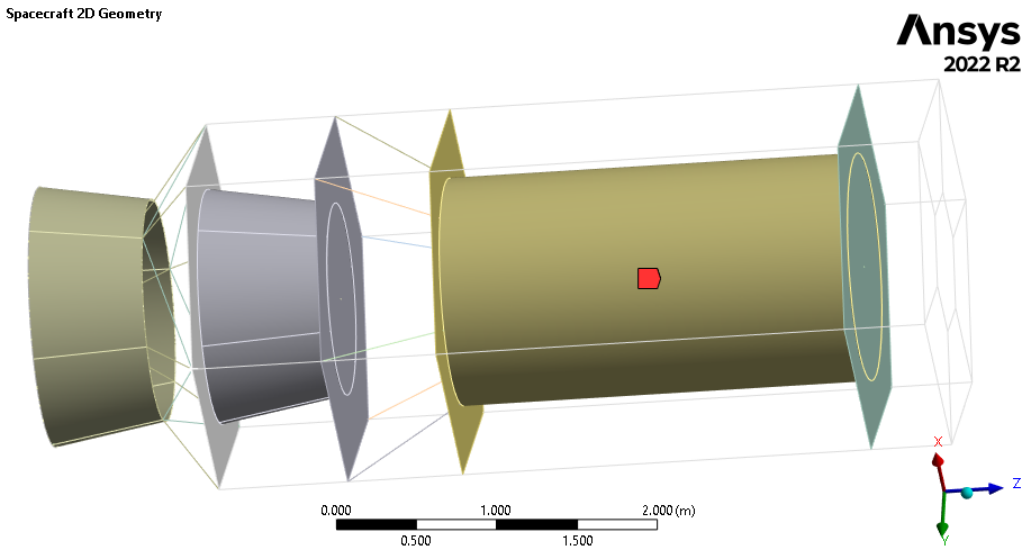

Figure 61: Isometric view spacecraft geometry.

To decrease the element count, 2D beam and shell elements were modeled. A full import of the 3D geometry would slow iteration. Specifically, 754 BEAM 189 and 7165 SHELL281 were used. Titanium was used for the structural members and the tank. A point mass, rigidly centered in the tank, of 7800 kg was used to simulate a full propellant load. Contacts were automatically generated, and all six degrees of freedom at the end nodes of all beams were restricted.

A primary iteration of the structural analysis generated a finite element model (FEM) was generated and iterated upon. The mesh of the previous iteration can be seen in Figure 62. The cross sections in this model are from a previous iteration of structural analysis shown in Table 6.

Table 6: Square beam tube section descriptions

Description	Width (mm)	Thickness (mm)
Tapered Bar	75	10
Axial Bar	100	10
Tank Bar (Top)	80	10
Tank Bar (Bottom)	100	10
Hexagonal Web Bar	50	5

The main differences from the first iteration include the introduction of plates to hold the tank, the inclusion of the pressurant tank, and new designs for an internal beam structure.

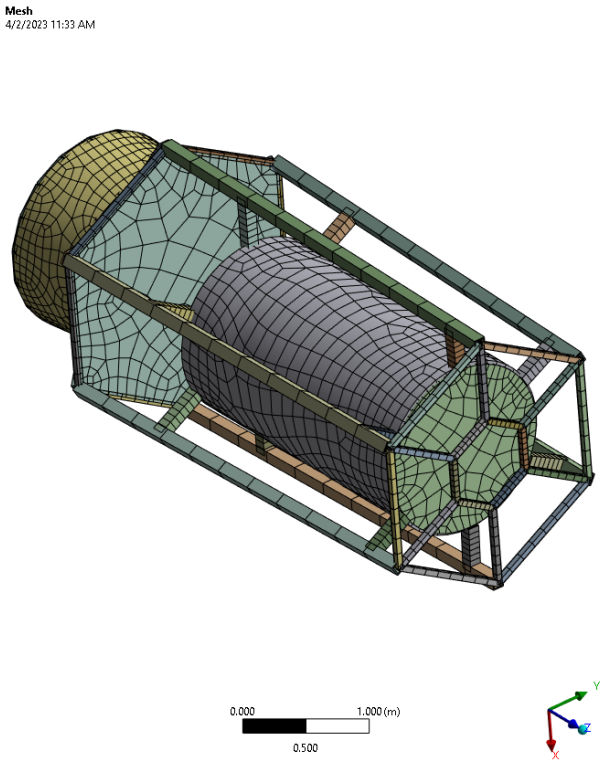

Figure 62: Previous iteration view of spacecraft mesh.

Figure 63 shows a view of the new iteration mesh, containing eighteen new structural members, new tank plates, and the pressurant tank. Element size was iterated upon in high-stress areas, like the payload adapter beams.

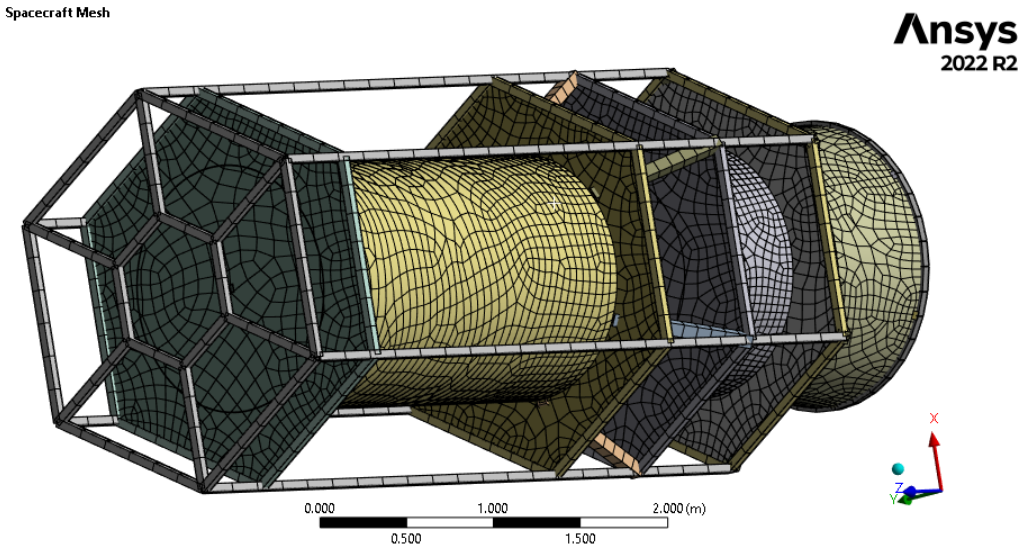

Figure 63: Isometric view of spacecraft fore mesh.

Figure 64 shows a side view of the aft mesh for the spacecraft, giving a view of the new structural members in the payload adapter.

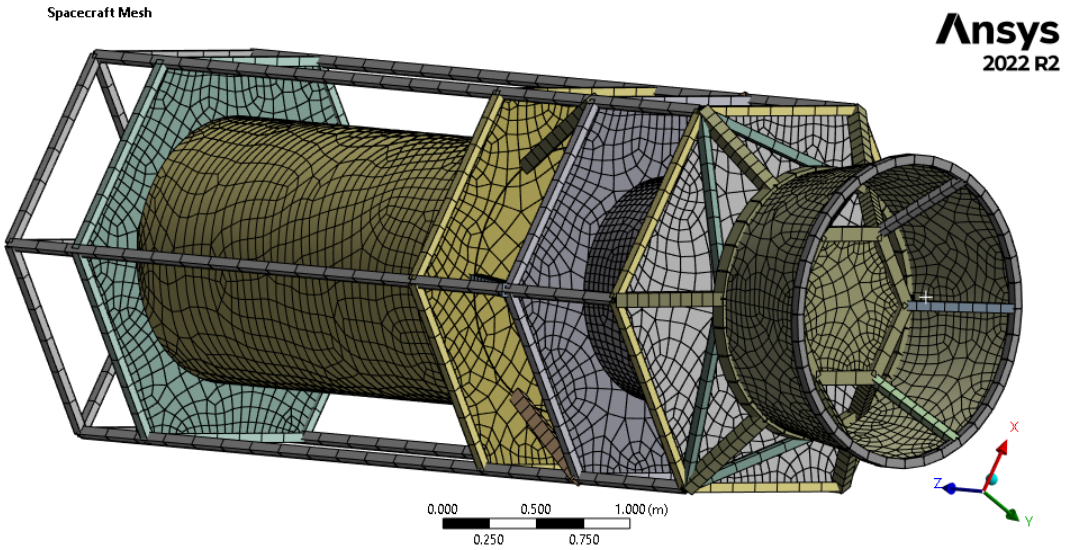

Figure 64: Side view of spacecraft mesh.

Figure 65 shows the aft view of the spacecraft mesh, where new diagonal beams create a green triangle shape. New vertical tapered beams were also introduced from the propulsion plate down towards the payload adapter to decrease the propulsion plate stresses.

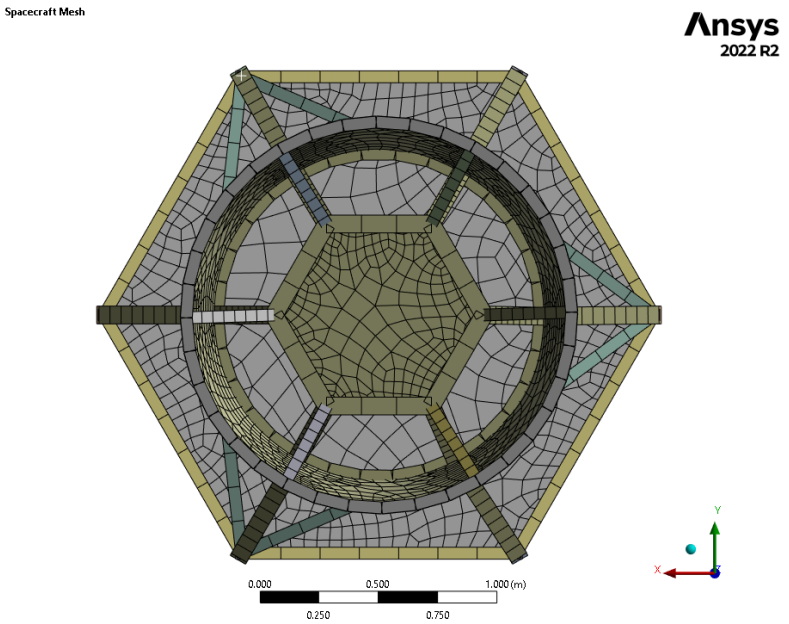

Figure 65: Aft view of spacecraft mesh.

For the entire structure, a builtin Titanium Alloy material with a density of $\rho = 4620$ kg-m^2, Young's Modulus of $E = 96$ GPa, and yield strength of $\sigma_y = 1.1$ GPa were used.

12.2.1 Launch Accelerations Finite Element Analysis

To simulate the accelerations from the definition in the Starship User Guide in Section 9.2.2, an axial load of 6g and a lateral load of 0.5g was applied while keeping the base of the payload adapter fixed. Figure 66 is a contour plot of the maximum Von-Mises stress in the shell elements, and Figure 67 is the maximum stress in the beam elements. The maximum stress was $\sigma_{max} = 120$ MPa in the shells, and $\sigma_{max} = 19.9$ MPa for the beams. To validate that these stresses did not pass the yield stress of Ti-6Al-4V with $\sigma_y = 1100$ MPa, with a factor of safety of 1.4, the stresses must not be above 785 MPa. The beams were optimized to nearly reach this threshold. For the shells, the maximum stress occurred in the coupling shield, where it interfaces with the tapered beams on the aft section of the spacecraft.

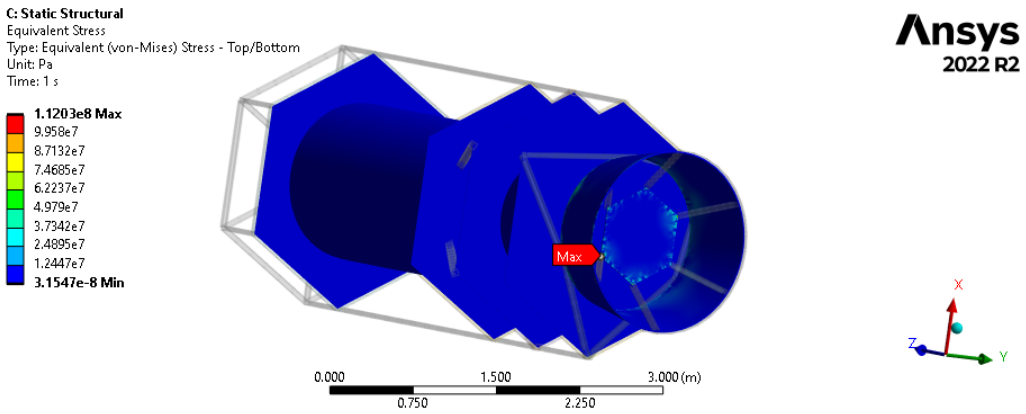

Figure 66: Maximum Von-Mises stress in shell elements during launch.

Figure 67 shows the maximum combined stress, or tensile stress, in the spacecraft beam elements. It can be seen that the top ring of the payload adapter is the point of the maximum stress, but it is two orders of magnitude from yielding.

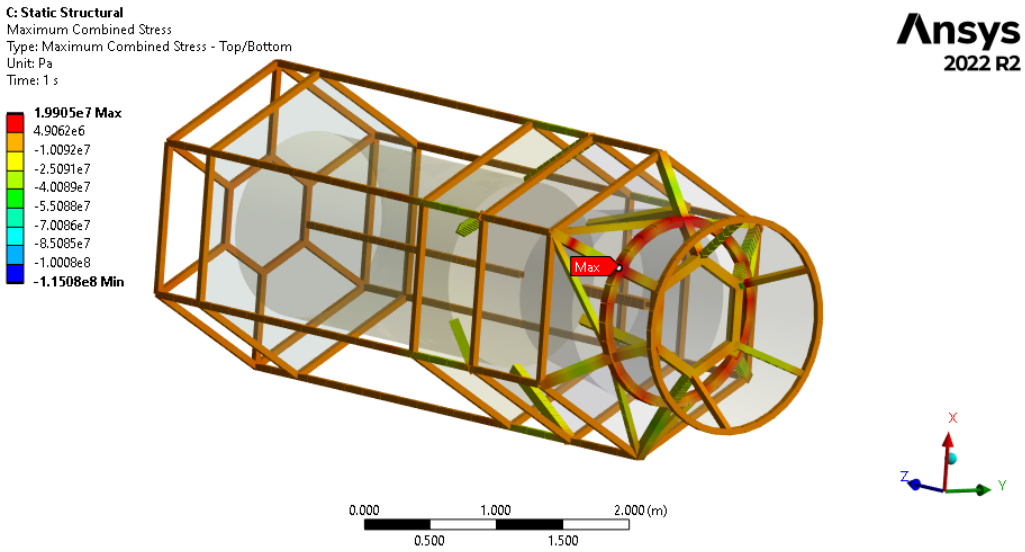

Figure 67: Maximum combined stress in beam elements during launch.

Figure 68 shows the minimum combined stress, or compressive stress, in the beam elements. The maximum occurs at the interface of the propulsion plate to the payload adapter tapered beams. This area is a known high-stress area, and will be further explored in the random vibration analysis.

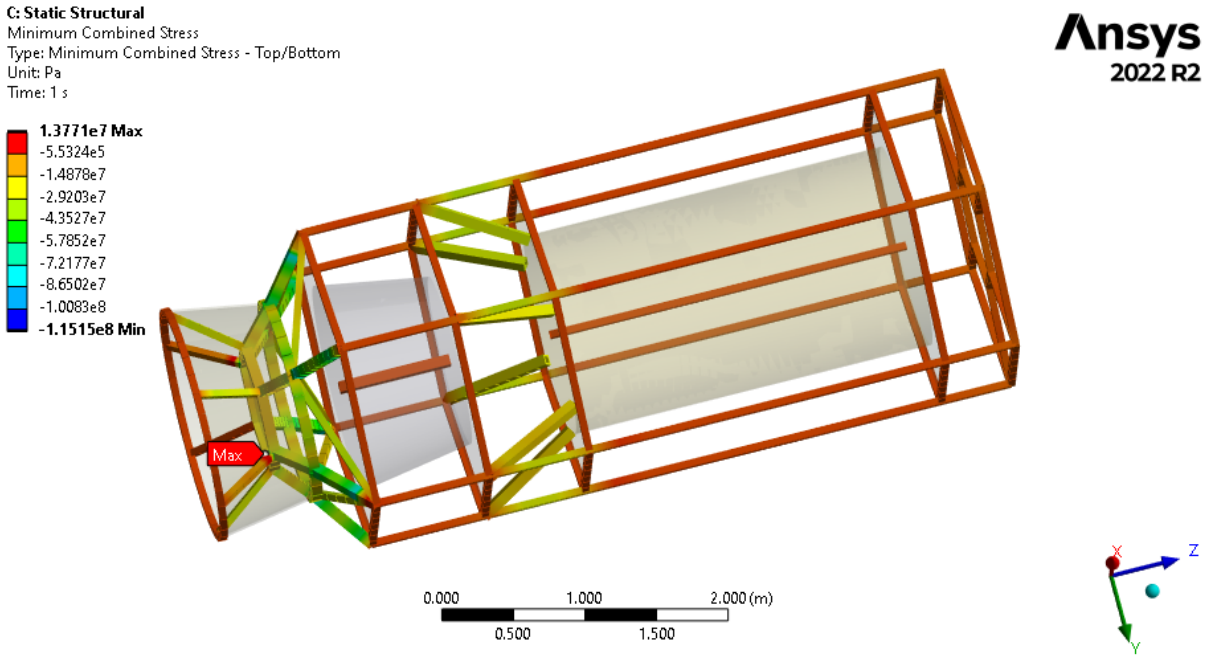

Figure 68: Minimum combined stress in beam elements during launch.

Since these stresses are less than those obtained in a future analysis, they were not a driving constraint for the sizing of the beams and the plates. The geometric values, seen in Table 8 in the conclusion, were iterated to provide the value nearest a factor of safety of 1.4, compared to the static structural analysis results, chosen through close analysis of [66].

12.2.2 Propulsion Impulse Finite Element Analysis

To simulate the stress applied to the structure when an impulsive force from the propulsion array is applied, another static analysis was necessary. An axial load of 2670 N, representing six 445 N thrusters, is applied at the rear beam connections where the nozzles are mounted. To approximate a worst-case scenario, the front of the satellite was assumed to be fixed. This is not representative of the inertia that resists the satellite, but it sets a high margin on the strength propulsion system mount. Figure 69 shows the stresses in this situation, with a maximum of $\sigma_{max} = 104$ MPa occurring on the beams holding the propulsion plate. This result does not exceed the yield stress for titanium and gives high margins due to the fixed boundary condition. This shows the safety of the light propulsion system on the refueler. The stresses in shell elements were not reported, due to being similarly lower than the yield stress.

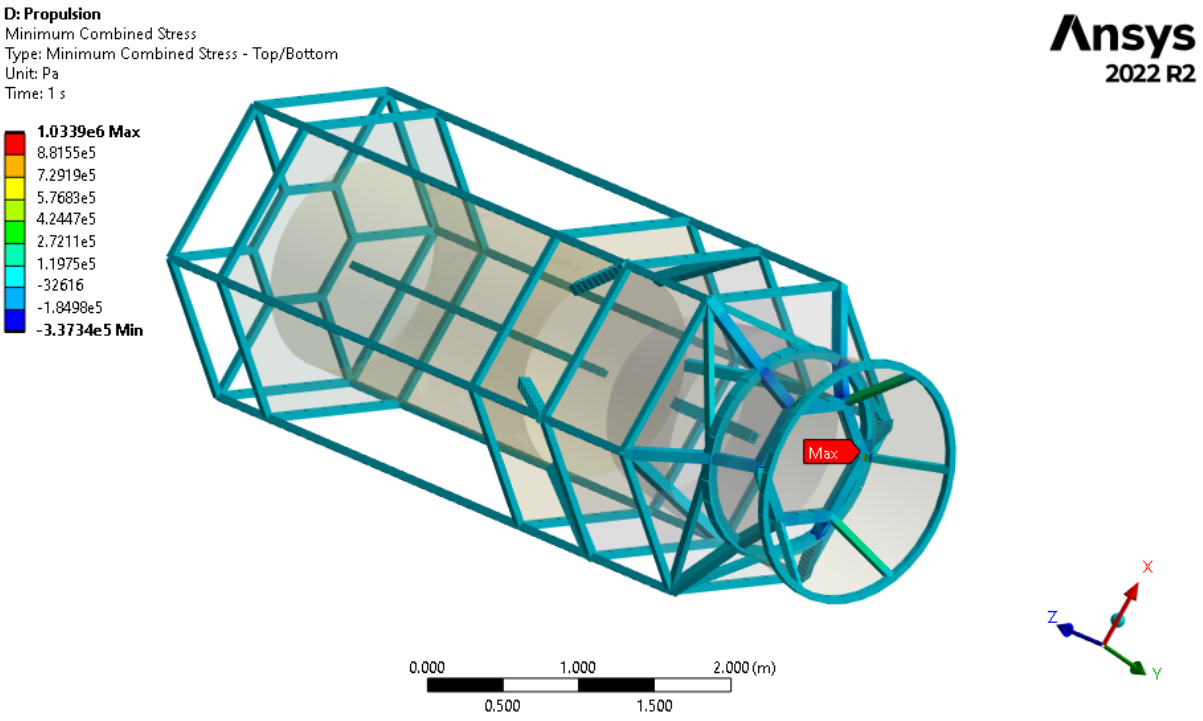

Figure 69: Maximum combined stress in beam elements for a simulated propulsion load.

Compared to the analytical result for the tapered beams, the FEA result is nearly 50 % less than the analytically obtained value. This is possibly because the analytical value models only a single beam with no other internal supports from the payload adapter ring.

12.3 Modal Analysis

To simulate the vibration of the spacecraft as it is mounted inside of the launch vehicle, a fixed base modal analysis is conducted. The base of the payload adapter is fixed to the launch vehicle via a bolted connection, and the spacecraft acts like a tuning fork atop the rocket as it accelerates and is perturbed by atmosphere and thrust, and the natural frequencies, or modes, are of interest. As the rocket increases frequency towards its maximum aerodynamic pressure, it is possible that the resonant frequencies of the rocket match that of the spacecraft, such that the amplitude of forced oscillations is magnified. The large displacements, and the corresponding stresses, are of interest as a failure mode at these natural frequencies.

Generally, the solver in Ansys uses a system of equations to solve for the displacement at every node, as well as its derivatives. The equation of motion for the system is shown in Equation 43. The matrices contain the mass, damping, and stiffness of nodes.

$$[M][\ddot{x}] + [C][\dot{x}][K][U] = [F] \tag{43}$$

Boundary conditions constrain this system, and modal analysis is generally more computationally costly as compared to static structural analysis. For this specific analysis, a fixed boundary condition was applied to the base of the payload adapter, and Ansys calculated frequencies and mode shapes. The first six frequencies, modes, are shown in Table 7.

Table 7: Modal analysis results.

Mode No.	Frequency (Hz)
1	16.567
2	18.375
3	44.390
4	46.732
5	46.732
6	52.082

These are rather high frequencies, the first two are bending mode shapes, three is a compression mode shape, and four, five, and six are torsional modes. A plot of the first bending mode shape is shown in Figure 70.

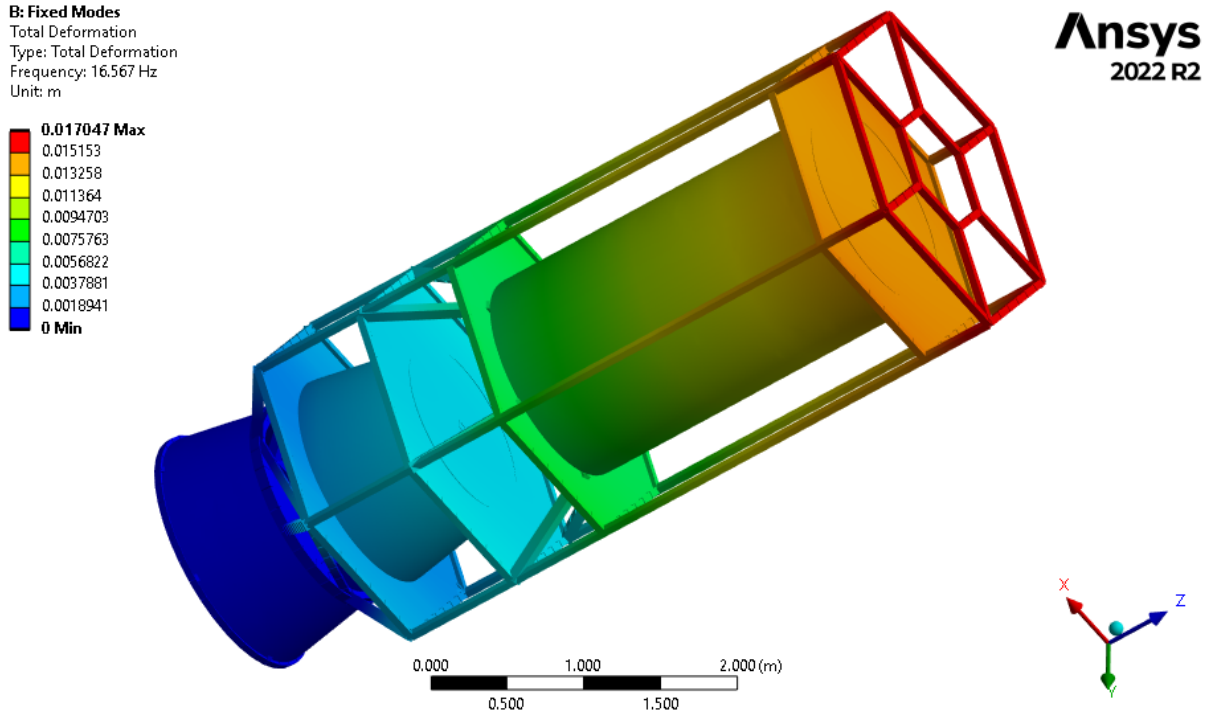

Figure 70: First bending mode deformation plot.

The spectrum of the first 50 modes is shown in Figure 71. The x-axis represents the mode number and the y-axis represents the frequency. These modes were all obtained to assist in running the random vibration analysis. It can be seen that around 50 Hz there is a densely packed response, and at 140 Hz there is a similarly dense response.

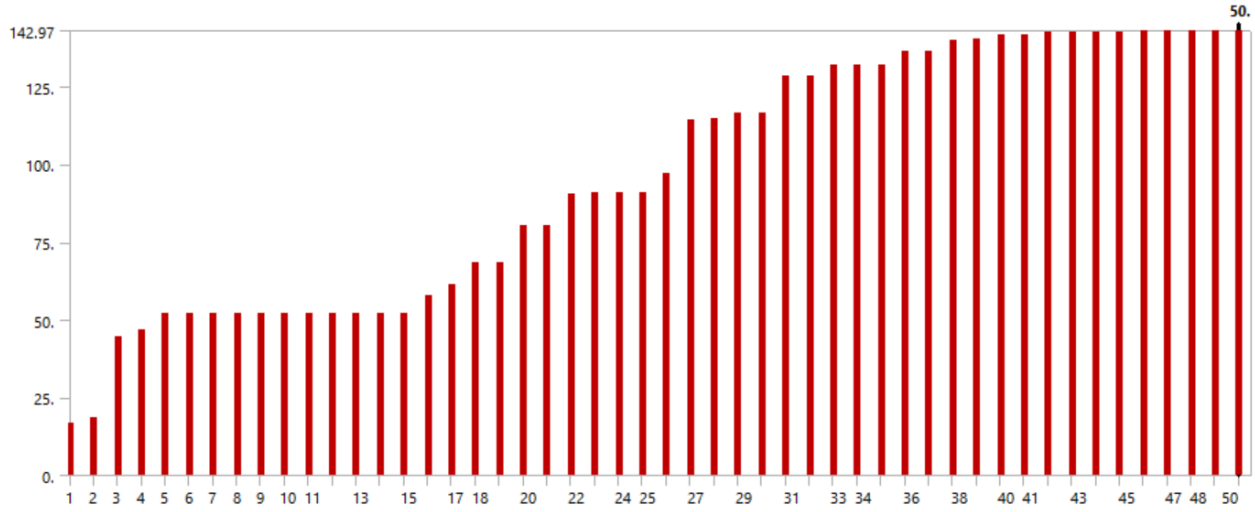

Figure 71: Mode number versus frequency.

12.4 Random Vibration Analysis

Random vibration is a non-deterministic motion that ensues when in many highly dynamic situations, such as a rocket launch. High aerodynamic loads and large internal stresses from propulsion cause perturbations in the structure at varying frequencies. The best way to model such an event is with a random vibration analysis that sweeps through different inertial "g" accelerations for frequencies in a certain range. These analyses are common for spacecraft FEMs and result in large stresses that can often be driving factors in structural design.

In the case of the refueling spacecraft, the previous modal analysis generated a large range of frequencies, many not shown, each of which can resonate with a certain frequency. From the Falcon User Guide, Figures 72 and 73 are obtained [29].

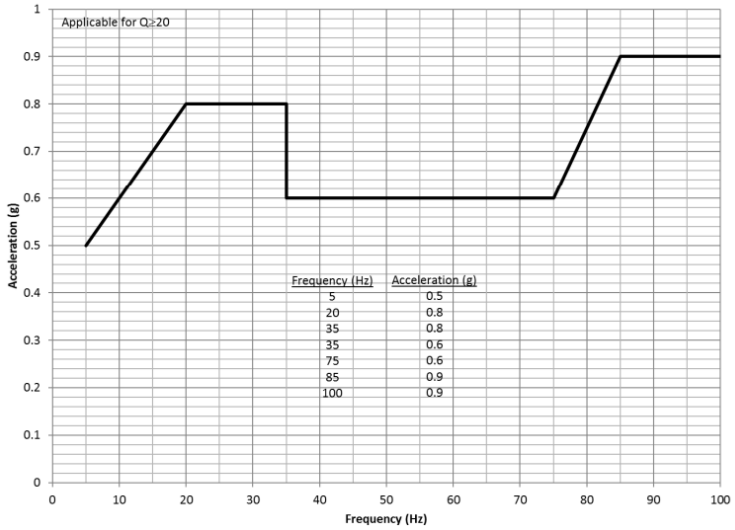

Figure 72: SpaceX axial sinusoidal inputs [29].

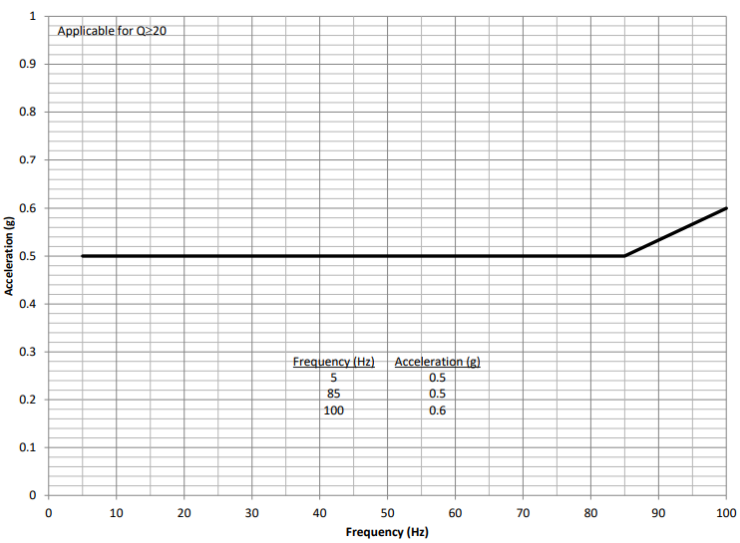

Figure 73: SpaceX lateral sinusoidal inputs [29].

Figures 72 and 73 give the axial and lateral accelerations as a function of frequency. These can be input as tabular power spectral densities, PSD-G objects, in Ansys Workbench, with reference to the previous fixed-base modal analysis. Fatigue is not considered due to the short duration of a rocket launch. For the analysis, a damping coefficient of $\zeta = 0.05$ was used from NASA standard MSFC-STD-3676 [67]. It should be noted that this damping assumption has a large impact on the output of the analysis, similar to how mesh fidelity can influence the results of the analysis. Since a random vibration analysis is non-deterministic, a probability factor of 3σ was used to assess the likelihood of these stresses forming to 99.73%. For shell elements, the maximum stresses were obtained on the top and bottom surfaces, and the results were generated as Von Mises equivalent stress. For beam elements, only a reasonable normal stress result was able to be generated in the X-direction (axial in the beam cross-section coordinate systems).

Figure 74 shows the maximum Normal stress in the spacecraft from the axial random vibration analysis. The high stress of $\sigma = 700$ MPa occurs at the interface of the propulsion plate to the beams. This is a concentrated area of normal stress because there is assumed to be a bonded or welded interface. There are also multiple beams connected to the points on the edge of the propulsion plate, such that if one beam is too stiff, it will cause a singularity on the thin plate. Normal stress was reported because Von Mises equivalent stress was not able to generate beam axial results.

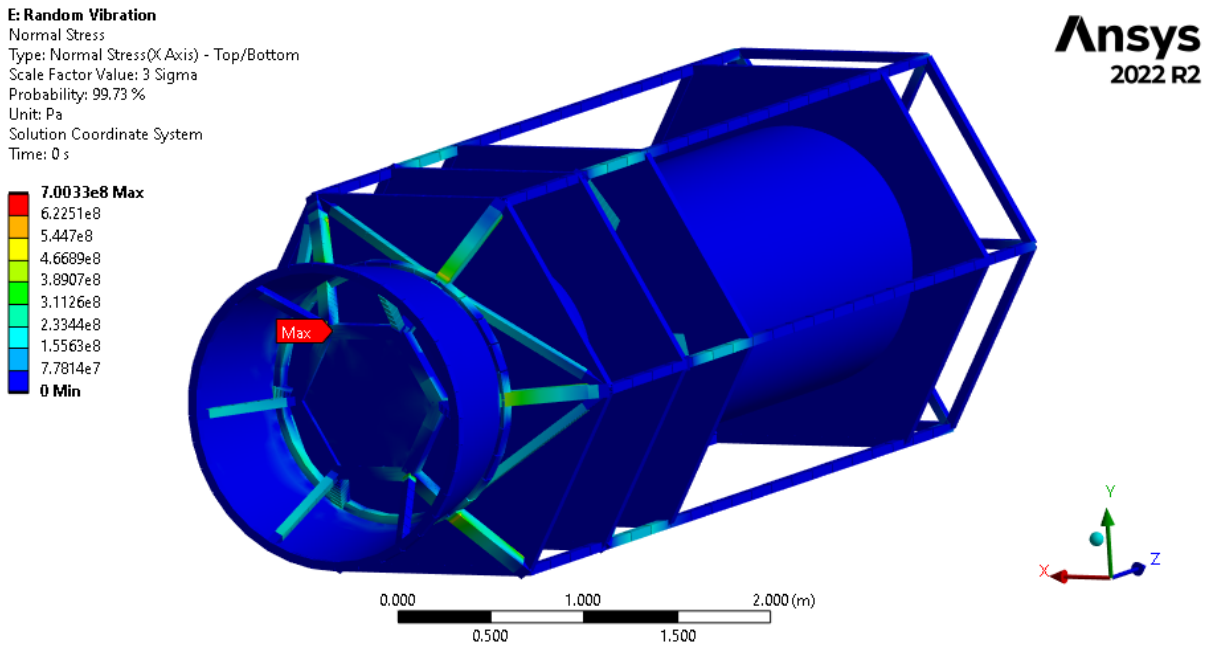

Figure 74: Axial response of sinusoidal inputs - Normal Stress.

Figure 75 shows the highest stress in the structural analysis, nearing the factor of safety yield stress of 785 MPa. Iteration was carried to a value of $\sigma = 748$ MPa, but due to the complicated nature of the structure, it was difficult to near the yield stress any further than 95%. The maximum stress is also reported at the same point as the maximum normal stress. A response plot for this maximum point is shown in Figure 76.

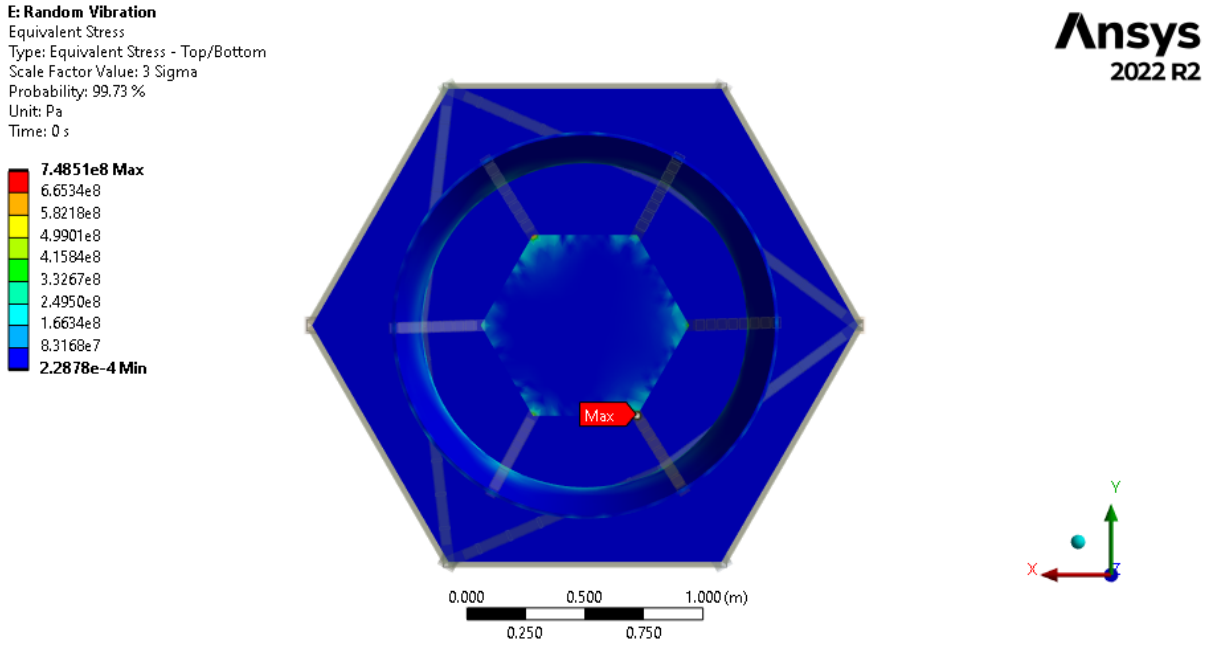

Figure 75: Axial response of sinusoidal inputs - Von Mises Stress.

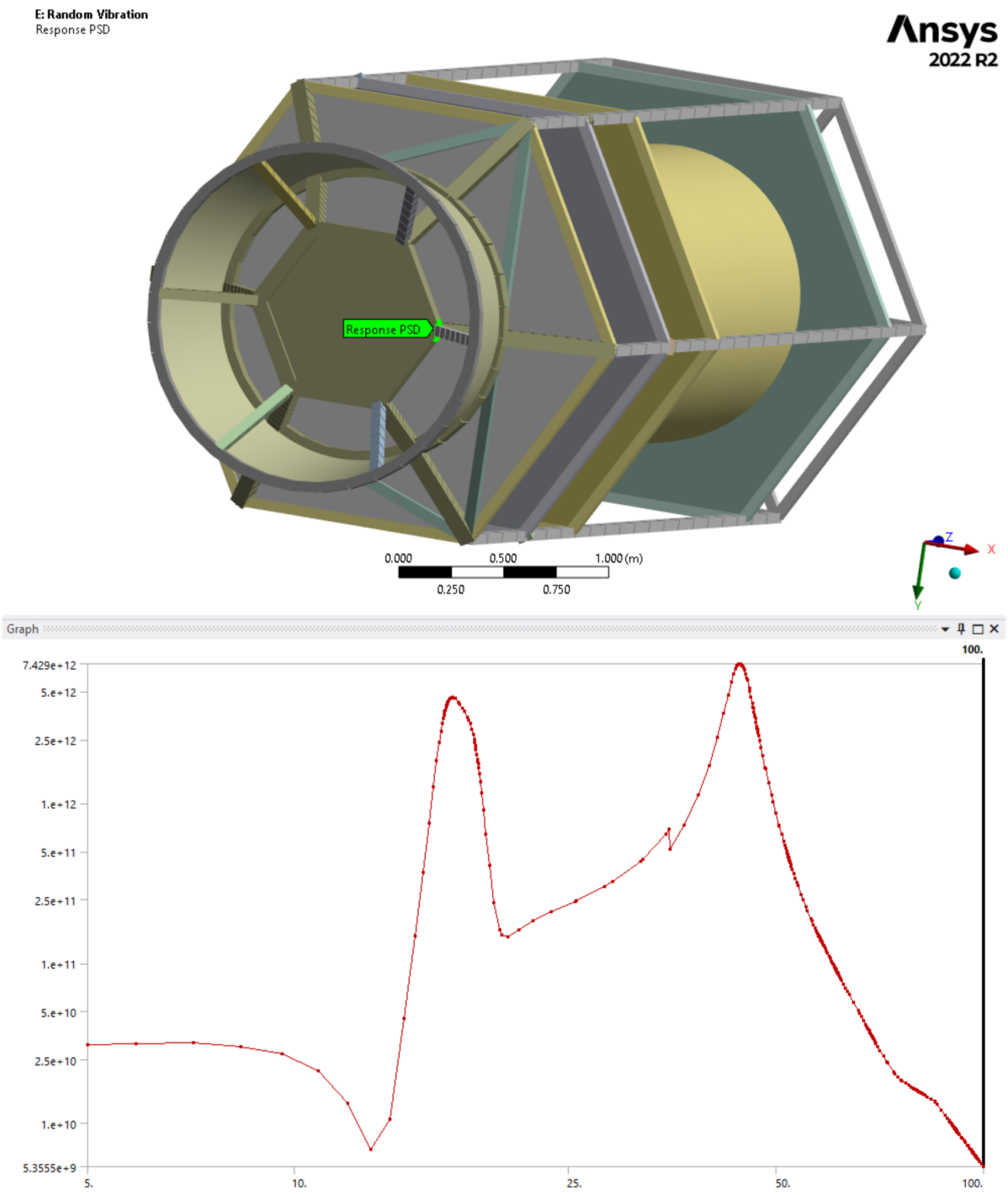

Figure 76: Frequency response at payload adapter interface for axial excitation.

To analyze the point of maximum stress, a frequency response plot is generated at the point on the propulsion plate. This response is shown in Figure 76. It is interesting that the response stress increases to such a large value, but it is unclear which element is being reported for, as multiple elements join at that node. There is a double resonance for the bending modes near 18 Hz and 50 Hz. These stresses should be minimized in future iterations.

For the lateral excitation, the analysis method was similar, a damping of $\zeta = 0.05$ was used and the data from 73 was input into a PSD-G acceleration tabular entry in Ansys. The results were obtained in the beams by using a normal stress value, and the stresses were obtained in the shells using a Von-Mises stress value. For the beams, the maximum stress of $\sigma = 596$ MPa occurs at the interface of the tapered beams to the bottom-most tank plate, as seen in Figure 77. This stress is safely under yield stress. This stress response in this area is shown in Figure 79.

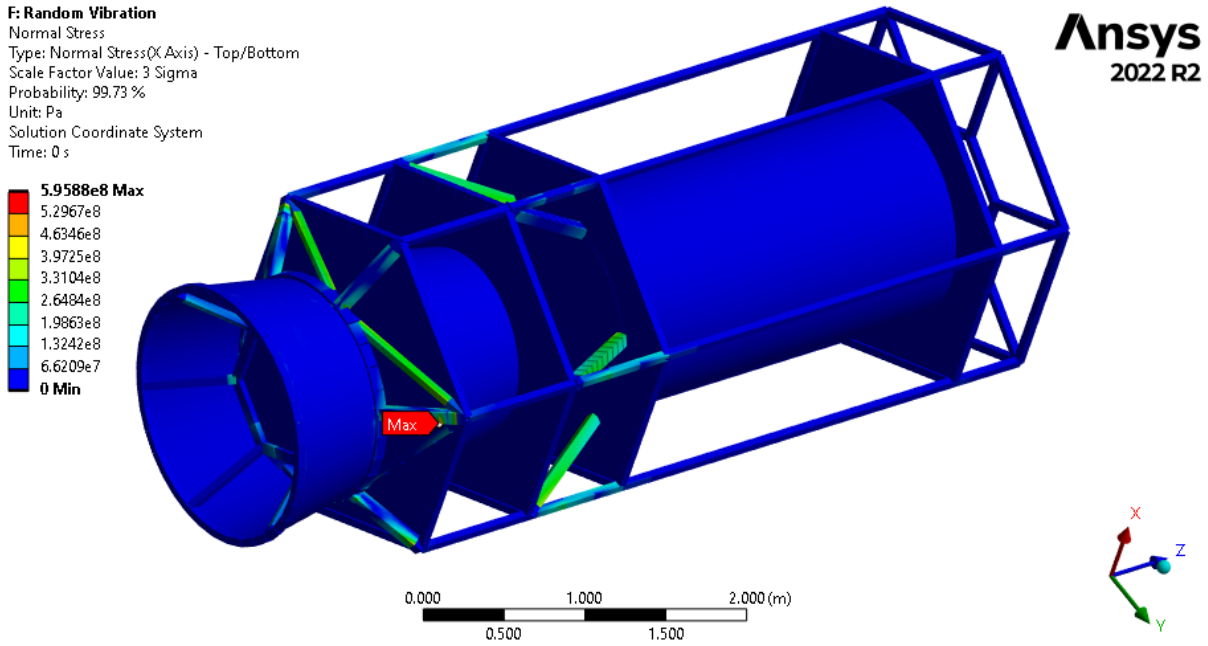

Figure 77: Lateral response of sinusoidal inputs - Normal Stress.

The Von Mises stresses are shown in Figure 78 and have a value of $\sigma = 512$ MPa at the interface of the payload adapter to the tapered beams. This stress is safely under yield.

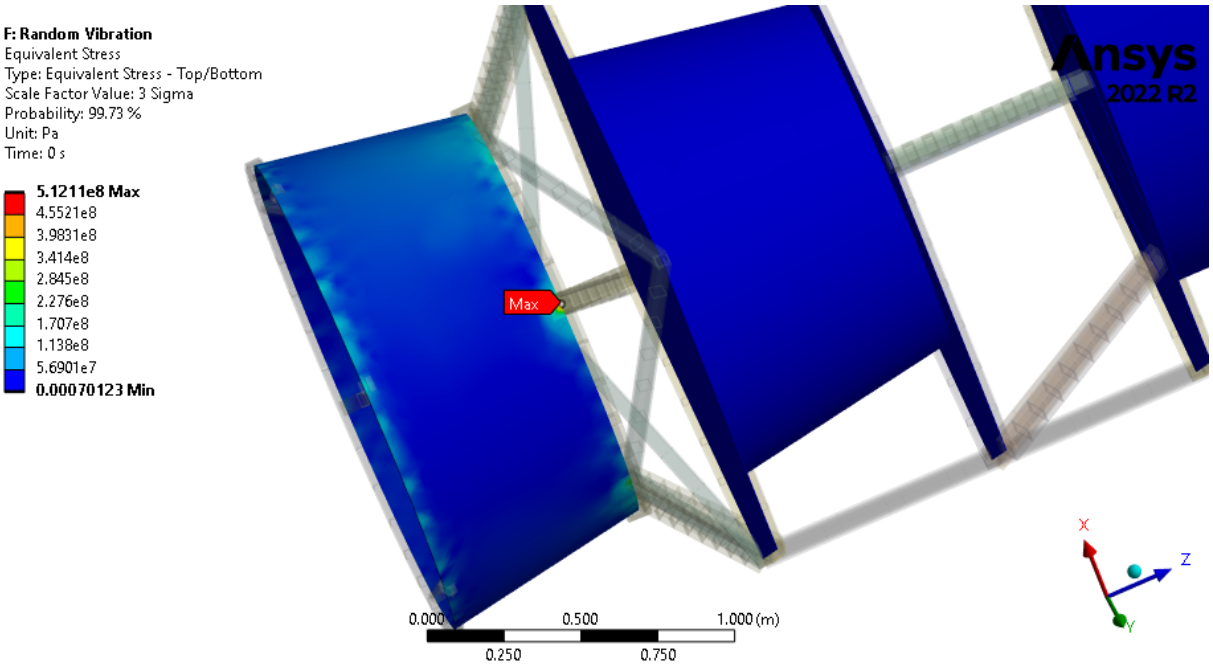

Figure 78: Lateral response of sinusoidal inputs - Von Mises Stress.

To analyze the specific area of high normal stress for the lateral random vibration excitation, the point shown on the geometry in Figure 79 has a stress response shown. The stress approaches a very high resonance at 18 Hz. These stresses will need to be minimized in future iterations.

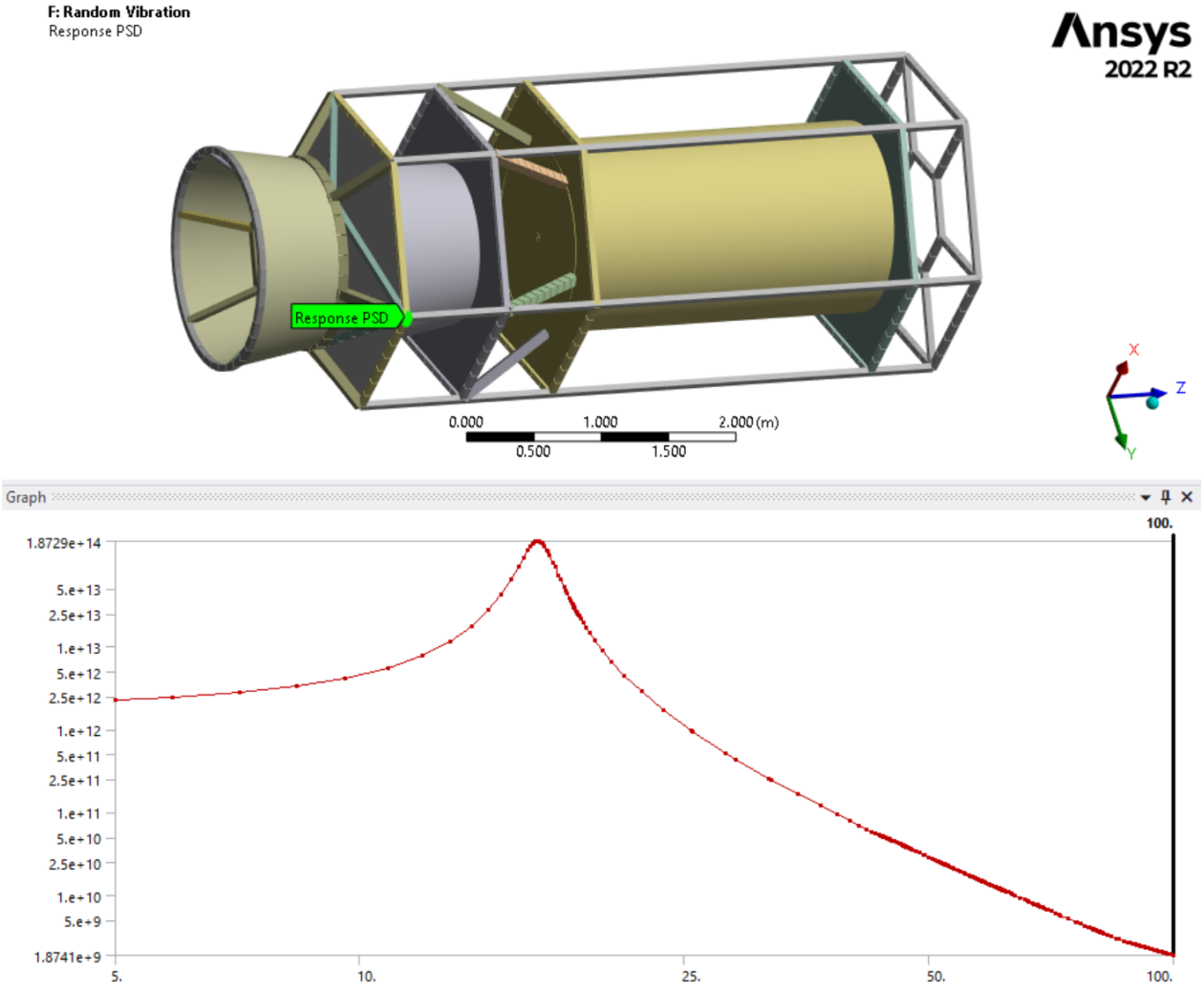

Figure 79: Frequency response at beam interface with tank plate for lateral excitation.

12.5 Structural Analysis Conclusions

Generally, the structure itself supports the weight of the large fuel tank to a satisfactory level. The analysis showed that the largest stresses occurred on the payload adapter, and extra structural members not included in the CAD would be necessary. This was the second iteration of the structural design, where the hexagonal plates were introduced to support the tanks instead of cantilever beams. This was able to decrease the stresses near the tank, but it increased the stresses in the aft structure.

A new random vibration analysis showed the highest stresses because the structure's resonant frequencies represented the large vibration of a large mass of the tank at the end of the beam. The axial random vibration was the highest stress in the analysis, optimized to the factor of safety yield stress within 95%. This analysis also informed the iterated sizes of the two beam cross sections and the three plate thicknesses. These can inform the next iteration of CAD. Figures 80 and 81 show what specific beams in the model were assigned to each cross-section.

Table 8: Square beam tube section descriptions.

Description	Width (mm)	Thickness (mm)
Coupling beams	75	15
Web beams	50	5

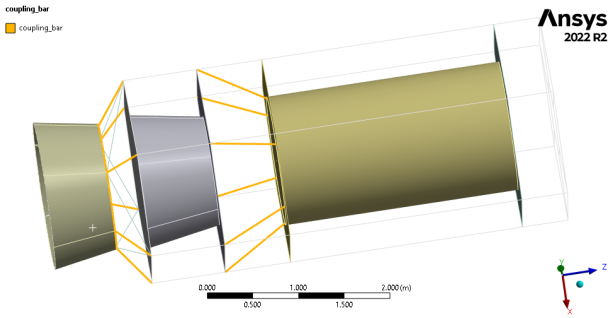

Figure 80: Geometry of selected coupling beams.

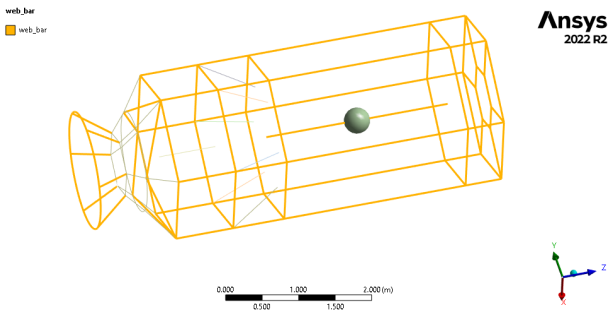

Figure 81: Geometry of selected web beams.

Table 9 shows the assigned plate thicknesses for the structural model. These can be iterated in a future version of the CAD.

Table 9: Plate thicknesses.

Description	Thickness (mm)
Propulsion Plate	10
Payload Adapter	15
Tank Plates	2.5

Ultimately, the second iteration of structural analysis on the refueling satellite confirmed the new structure would survive the launch environments analyzed. Future analyses include acoustic and thermal analyses, but these often do not generate high stresses and strains in comparison to static loading and random vibration analyses. The goal of the structural analysis is to inform the design, and the addition of new structural members in this iteration leaves the opportunity for new updates in the CAD. In reality, many iterations of heavy FEA completed by multiple analysts on every structural member are necessary to show that a satellite will survive the launch environment.

13 Spacecraft Dynamics

This section contains inertia information on the satellite, confirms axisymmetry and simulates the Monarch RCS thrusters for a rotation about the x-direction of the spacecraft. The code for this section can be found in the Appendix Section 19.3.

13.1 Inertia Properties and Stability

In order to approximate the satellite as axisymmetric, the inertia properties must be examined. An axisymmetric satellite will have symmetry about a single axis, and that is denoted as the axial direction (Z-direction in Figure 82 The lateral directions are defined as that perpendicular to the axial direction (X, Y-directions). In Figure 82, the spacecraft is in its operating conditions where the major axis is coincident with the axial direction of the spacecraft. The solar panels were sized such that they would assist in the generation of the major axis being coincident with the axial direction. Due to Poinsot's Solution, in torque-free motion, or in space, a spacecraft will decay from a minor axis spin, through intermediate axis spin, to major axis spin [68]. This is connected with the geometric visualization of the momentum and energy ellipsoid. The highest energy state for a spinning body is around its minor axis, or about the smallest moment of inertia. A spacecraft will decay, due to dissipative effects, to a spin about its major axis. This major axis spin has been seen as an irrecoverable attitude failure in missions such as Explorer 1, where a prolate satellite (imagine a long cylinder) began to spin about its major axis after being spun up about its minor axis. The following definitions show the principal directions and principal moments of inertia of the spacecraft. These were generated using the complete SolidWorks assembly with materials defined for all parts. These could be used for future control and dynamic analysis. The principal directions are relative to the coordinate system in 82.

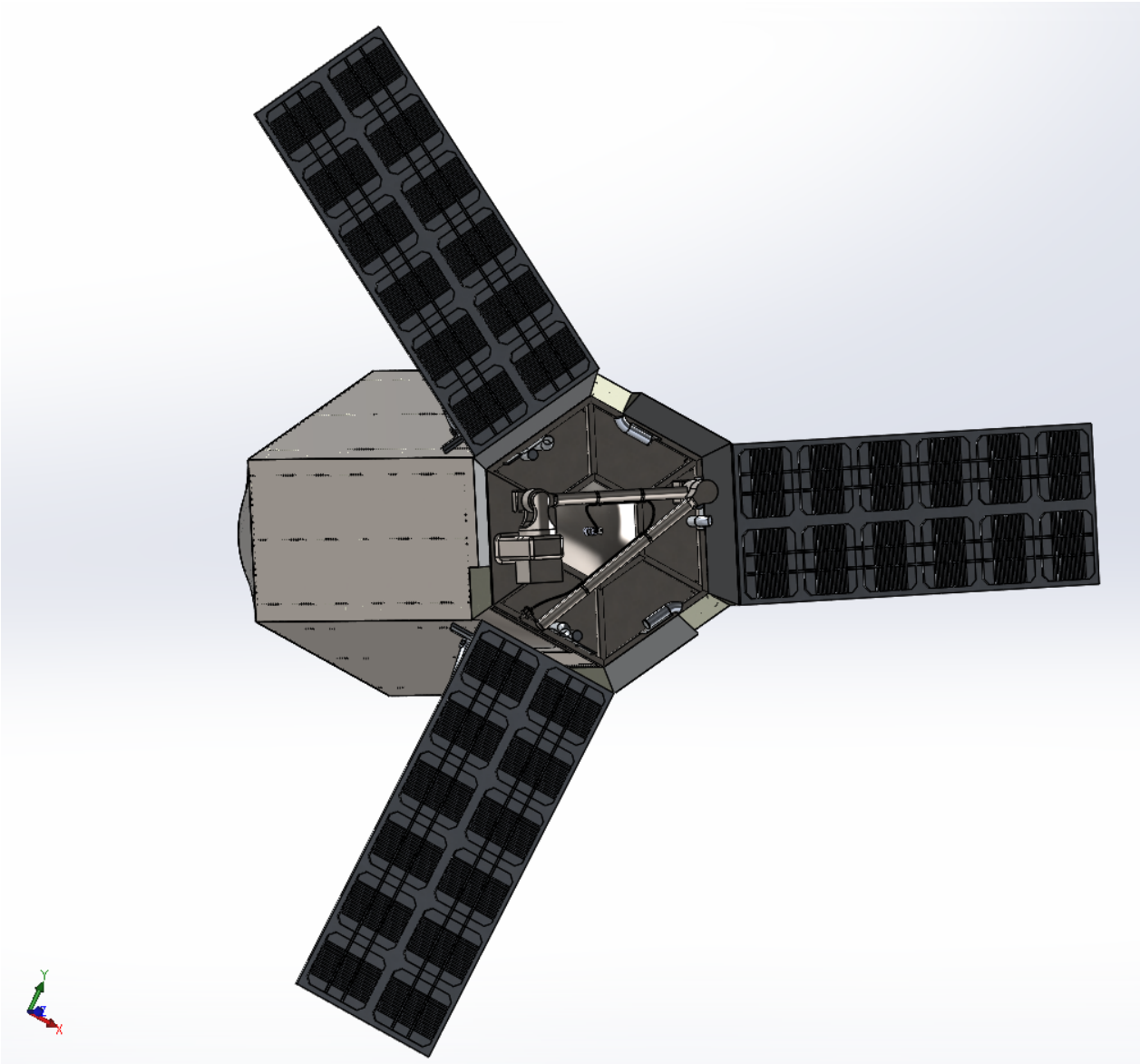

Figure 82: Deployed state of spacecraft.

$$\hat{e}_x = [0.784, 0.620, 0.030], \quad I_{xx} = 30575.493 \text{ kg-m}^2 \tag{44}$$

$$\hat{e}_y = [-0.620, 0.785, -0.022], \quad I_{yy} = 30817.962 \text{ kg-m}^2 \tag{45}$$

$$\hat{e}_z = [-0.037, -0.001, 0.999], \quad I_{zz} = 43490.762 \text{ kg-m}^2 \tag{46}$$

It can be observed that the difference in the I_{xx} and I_{yy} moments of inertia is less than 1%, which allows for an axisymmetric assumption to hold. The I_{zz} moment of inertia is the largest in this deployed position, and therefore the refueling arm will, in the spacecraft's lowest energy state, generally point in the axial direction when extended. The main advantages of

axisymmetry are the dynamical effects in torque-free motion discussed earlier, as well as the simplification of a control scheme such that the spacecraft can be defined in a coordinate frame that precesses and nutates with the body but does not spin. This removes the complication of including the spin angle in the analysis since the spacecraft will always be symmetric about that axis.

13.2 Thruster Six Degree of Freedom Simulation

To simulate the dynamics of the satellite, quaternions are used to four-dimensionally describe a three-dimensional attitude. For a given rotation matrix $\mathbf{C}$, for this specific case, an Euler 3-1-3 analysis was used. The quaternions $\beta_0,\ \beta_1,\ \beta_2,\ \beta_3$ can be found using the Equations below (4.2.6) [68].

$$\beta_0^2 = \frac{(1 - tr(\mathbf{C}))}{4} \tag{47}$$

$$\beta_0\beta_1 = \frac{(C_{23} - C_{32})}{4} \tag{48}$$

$$\beta_0\beta_2 = \frac{(C_{31} - C_{13})}{4} \tag{49}$$

$$\beta_0\beta_3 = \frac{(C_{12} - C_{21})}{4} \tag{50}$$

Somewhat inversely, the Euler 3-1-3 matrix $\mathbf{C}$ can be shown as a matrix of these quaternions (4.2.6) [68]. This matrix is necessary for angle recovery.

$$C(\beta) = \begin{bmatrix} \beta_0^2 + \beta_1^2 - \beta_2^2 - \beta_3^2 & 2(\beta_1\beta_2 + \beta_0\beta_3) & 2(\beta_1\beta_3 - \beta_0\beta_2) \\ 2(\beta_1\beta_2 - \beta_0\beta_3) & \beta_0^2 - \beta_1^2 + \beta_2^2 - \beta_3^2 & 2(\beta_2\beta_3 + \beta_0\beta_1) \\ 2(\beta_1\beta_3 + \beta_0\beta_2) & 2(\beta_2\beta_3 - \beta_0\beta_1) & \beta_0^2 - \beta_1^2 - \beta_2^2 + \beta_3^2 \end{bmatrix} \tag{51}$$

It can be shown, that a seven-by-seven system of equations with four quaternions and three body fixed angular velocities is equivalent to the system developed with Euler's equations, but lacking a singularity detriment known as gimbal lock. This system of equations is rewritten here in Equations 52 and 53.

$$\begin{aligned} \dot{\beta}_0 &= \frac{1}{2}\left[-\omega_1\beta_1 - \omega_2\beta_2 - \omega_3\beta_3\right] \\ \dot{\beta}_1 &= \frac{1}{2}\left[\omega_1\beta_0 - \omega_2\beta_3 + \omega_3\beta_2\right] \\ \dot{\beta}_2 &= \frac{1}{2}\left[\omega_1\beta_3 + \omega_2\beta_0 - \omega_3\beta_1\right] \\ \dot{\beta}_3 &= \frac{1}{2}\left[-\omega_1\beta_2 + \omega_2\beta_1 + \omega_3\beta_0\right] \end{aligned} \tag{52}$$

$$\begin{aligned} \dot{\omega_1} &= \left(\frac{I_2 - I_3}{I_1}\right)\omega_2\omega_3 + \frac{M_1}{I_1} \\ \dot{\omega_2} &= \left(\frac{I_3 - I_1}{I_2}\right)\omega_3\omega_1 + \frac{M_2}{I_2} \\ \dot{\omega_3} &= \left(\frac{I_1 - I_2}{I_3}\right)\omega_1\omega_2 + \frac{M_3}{I_3} \end{aligned} \tag{53}$$

These seven equations define the system and are perfectly formatted to input into ODE45. The workflow for integration is that a function file is defined that carries out the derivative definition in the above equations. Then, the simulation script calculates the initial conditions, and processes and plots the results.

For the state vector $\vec{x} = (\beta_0, \beta_1, \beta_2, \beta_3, \omega_x, \omega_y, \omega_z)$, the results for the quaternions are plotted in Figure 83. An interesting property of quaternions is that $\beta_0^2 + \beta_1^2 + \beta_2^2 + \beta_3^2 = 1$, this check is employed in the code. These quaternions oscillate based on the initial conditions, and they evolve over time.

For two 90 N Monarch thrusters positioned 1.4 m away from the CG, assuming that control is in both directions, an impulse is applied to the satellite inertias outlined in the previous section. This impulse has its time calculated such that the total rotation of the satellite is $\theta = 90°$. Figure 83 shows how the zeroth and first quaternions meet each other over time as the moment is applied.

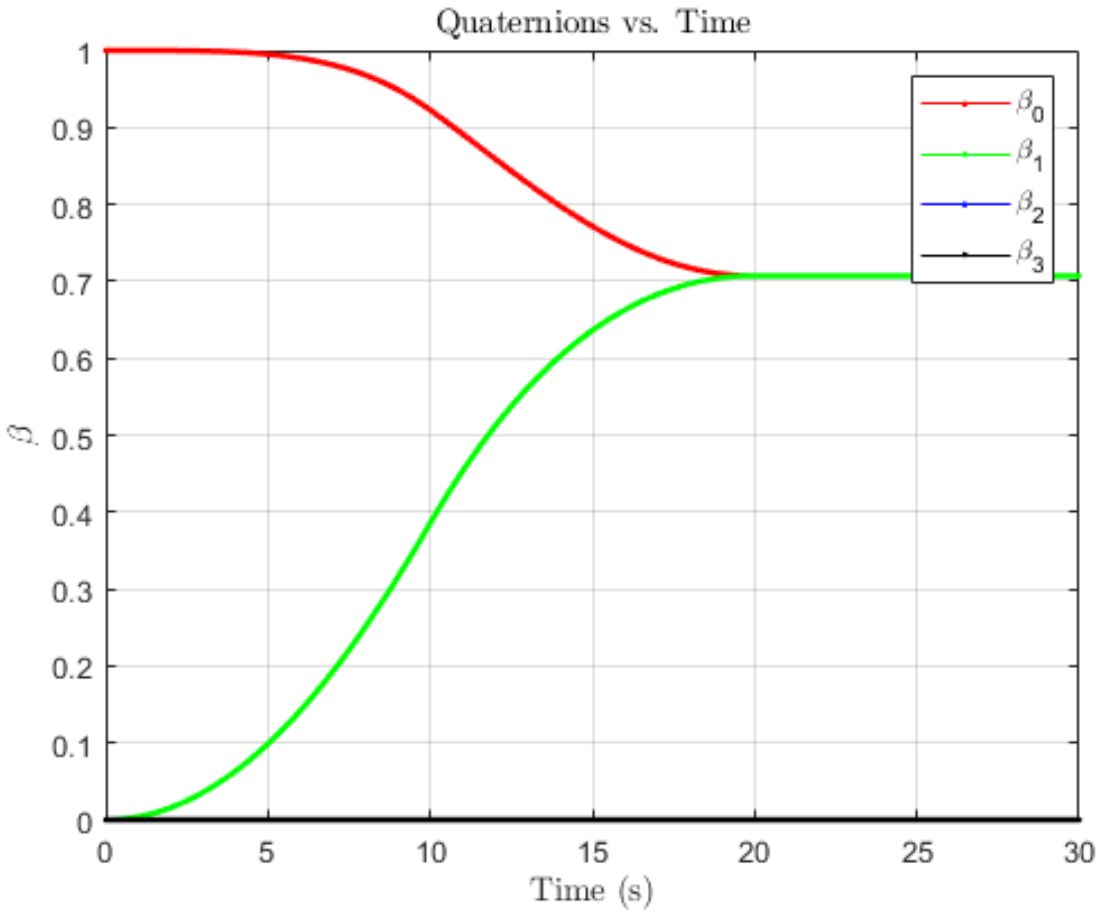

Figure 83: Quaternion variables versus time during the burn.

Figure 84 shows the nutation angle θ that increases to 90° in about 20 seconds.

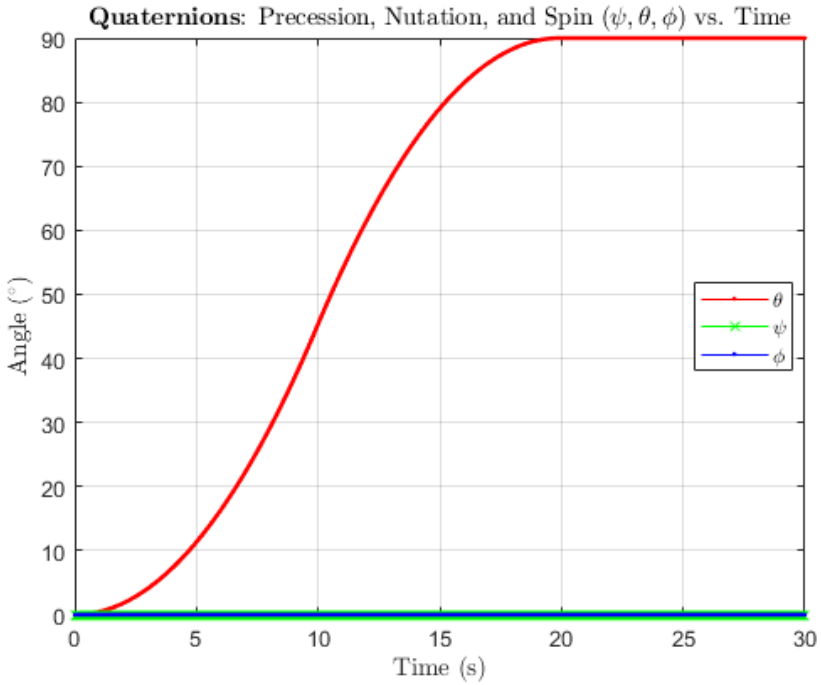

Figure 84: Nutation angle over time of the burn.

Figure 85 shows how the x-axis angular velocity changes at a specific point where the moment is applied in the opposite direction for the remainder of the burn.

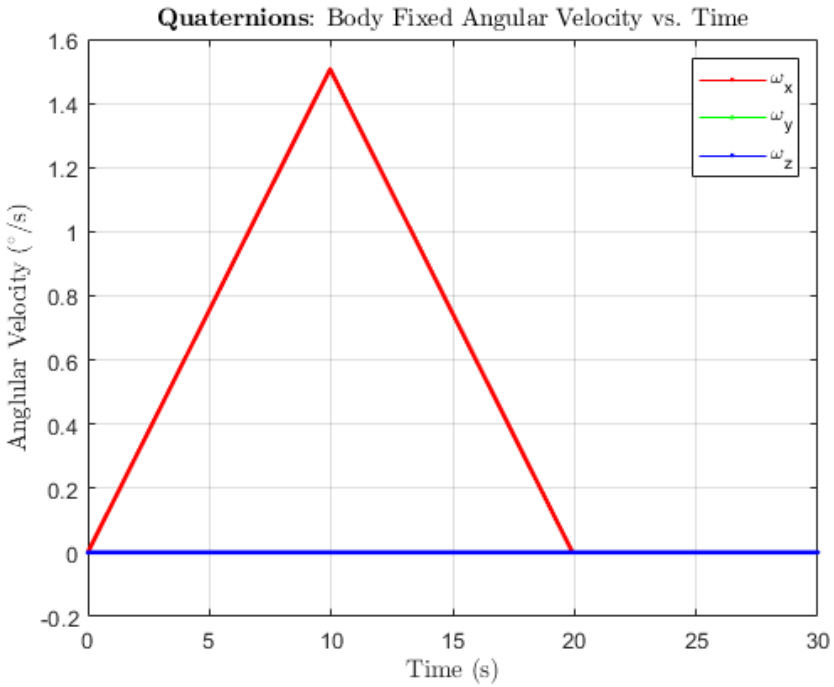

Figure 85: Body fixed angular velocities over time.

In conclusion, a rotation of $\theta = 90^\circ$ about the spacecraft x-axis is simulated for the inertia gathered in SolidWorks and using the impulse of two 90N Monarch thrusters. Code for this section is included in Section 19.3.

14 Fluid System

Calculations on the fluid system are required in order to ensure that the hydrazine fuel can be delivered to not only refuel other satellites but also the propulsion system. The goal of the calculations was to determine the temperature, pressure, density, mass flow rate, and velocity of the fluid at each state throughout the fluid system. After each of the states is set, the final goal of the fluid system calculations is to determine the volume and pressure needed for the pressurant tank. The calculations required will be finding head loss due to various components and connections, equations of state, and fluid mechanics; all using EES.

14.1 Plumbing Schematic

To size the helium tank, a plumbing schematic had to be made to roughly determine the location, sizing, and lengths of pipes, valves, and tanks. After iterating the schematic to account for the numbers of bends and lengths of connections, the schematic shown below in Figure 86 depicts the diagram used for laying out the different state locations used to aid in breaking down the satellites hydrazine plumbing calculations.

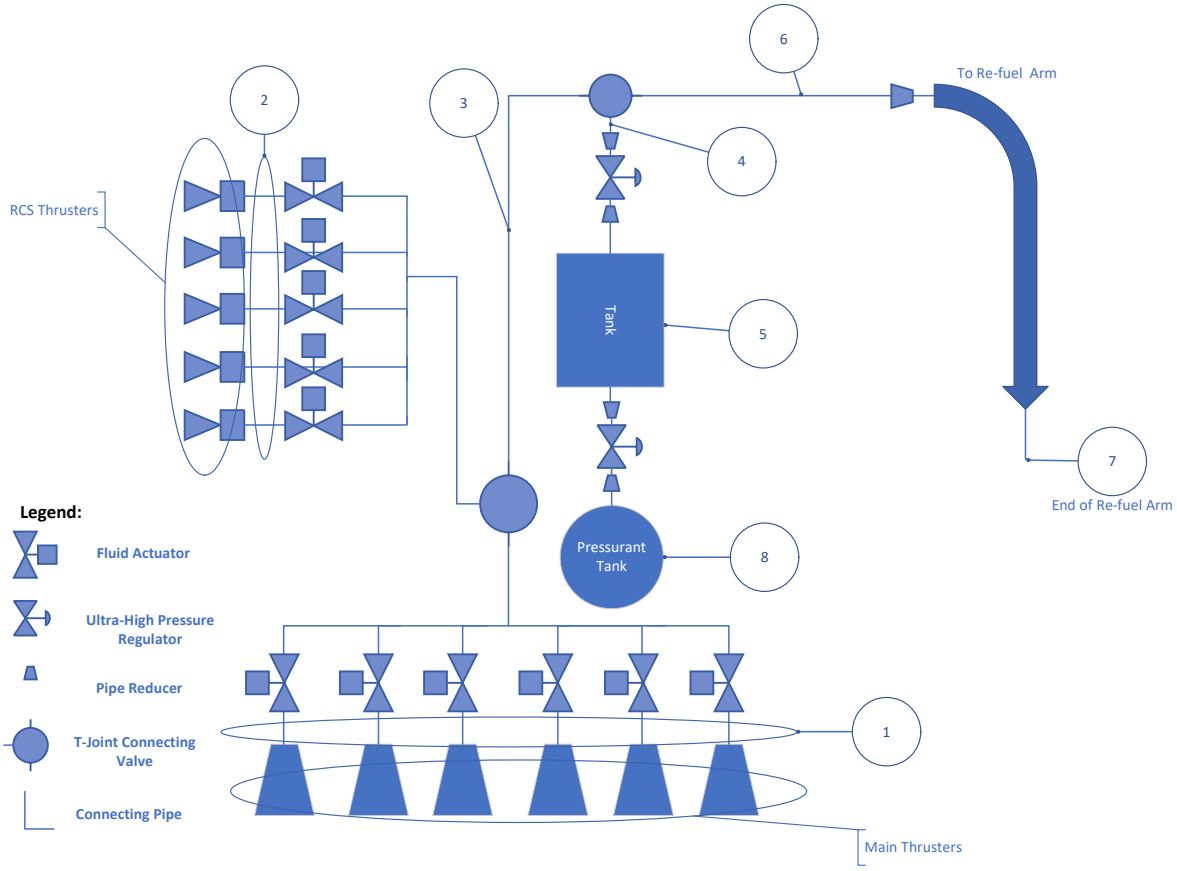

Figure 86: Satellite plumbing schematic.

States 1 and 2 are each located right before the injection point of the main thrusters and Reaction Control System respectively. State 3 is located above the lower connecting valve. State 4 is located at the point after the hydrazine tank above the valve. State 5 is located inside the hydrazine tank. State 6 is located at the point to the right of the upper connecting valve and positioned before the start of the fuel delivery arm. State 7 is located at the end of the arm before the injection point of the RAFTI delivery system. Lastly, state 8 is located within the helium pressurant tank, the main piece to be sized with these resulting calculations.

14.2 Assumptions and Equations

When working through the plumbing calculations it was important to start at the points where the fuel would be used: at the main thrusters, the RCS thrusters, and most importantly the fuel delivery arm. Starting with the combined thruster and RCS system, each specific impulse (I_{sp}) combined with the force delivered by each type of thruster, with Equation 54, yielded a mass flow rate needed from the hydrazine storage tank.

$$I_{sp} = \frac{F}{\dot{m} g_o} \tag{54}$$

The value for g_o was found related to the average altitude the refueler would be orbiting in resulting in a gravitational constant of 9.6 $\frac{m}{s^2}$. The relation in Equation 54 between specific impulse (ISP) and the force provided for a thruster can be used to determine the inlet pressure for the thrusters because when compared with data for similarly sized main and RCS thrusters and interpolating the given inlet pressures to match the force provided; the discrepancy between the ISP yielded inlet pressures and the interpolated values. There was a percent difference of 0.25% and 2.25% for the Main and RCS thrusters respectively. Therefore, the inlet pressures found using Equation 54 were deemed correct.

The flow velocity of each section of piping could then be found using Equation 55 relating mass flow, velocity, cross-sectional area, and density.

$$V = \frac{\dot{m}}{\rho A_c} \tag{55}$$

Next, the layout for the main thrusters and the RCS had to be planned out for how it would roughly fit in the satellite structure. Therefore, the number of piping bends and types of connections were determined. Then, after setting all temperatures within the satellite to a steady-state atmosphere of 10°C, the head loss and resulting pressure changes were calculated between each state using Equations 56 and 57, where "f" is the friction factor from each section's Reynolds and Relative Roughness values.

$$H_f = f(\frac{L}{D} + \sum K)(\frac{V^2}{2g_o}) \tag{56}$$

$$\Delta P = H_f g_o \rho \tag{57}$$

The summation of K values is a non-dimensional value related to "the multiple of velocity heads that will be lost by the fluid passing through the fitting" [69]. Therefore, each section has a K value associated with each bend, valve, length of piping, etc. that has to be summed to properly calculate each section's total head loss and its resulting pressure drop.

After working back to reach the connecting valve right outside of the hydrazine tank, the analysis had to "halt" and go out again to now work backward from the mass flow rate required by the fuel delivery arm. Using Orbit Fab's RAFTI Valve Service Manual, the low-pressure Maximum Expected Operating Pressure (MEOP) at the inlet was found. Unfortunately, the typical mass flow rate was yet to be determined, therefore a reasonable mass flow rate of 0.10 kg/s was used for the ongoing calculations [5]. Following the same procedure as outlined above, the head loss from the delivery arm was determined up to the T-joint just outside of the hydrazine tank.

Once arrived at the point before entering the tank, calculations must be used to size the fluid regulator to be used to maintain the pressure and control of the fuel to be dispersed throughout the rest of the system just described above. Using Equation 58 the max pressure can be related to the outside of the tank, shown as state 4 in Figure 86, and the pressure inside the hydrazine tank, shown as state 5 [70].

$$C_v = Q\sqrt{\frac{SG}{\Delta P}} \tag{58}$$

Where C_v is the flow coefficient and SG is the specific gravity of the fluid of concern. C_v is a value that as a standard represents the amount of fluid that can flow through a valve

when fully opened, and therefore a higher C_v the more fluid that can flow gives a pressure differential. One aspect of sizing pressure regulators is that when solving for the "unitless" coefficient, it is necessary to transfer from metric to the specific English units that were used when deriving the original equation above. Therefore, pressure must be changed to units of psia, and volumetric flow to units of standard cubic feet per minute (SCFM). This must be done to get value for C_v that is comparable with other C_v sizing indexes available online, otherwise, the meaningless units that were originally just disregarded due to no significance get even more jar-bled and yield incomparable data to other theoretical calculations provided by Swagelok C_v calculators [71]. The C_v value used for the hydrazine tank pressure regulator was collected from a database provided by Swagelok for aerospace pressure regulators that are currently manufactured. As seen in Figure 87 is a table used to size up the C_v.

Technical Data—Performance

Series	Maximum Inlet Pressure① psig (bar)	Maximum Outlet Control Pressure① psig (bar)	Flow Coefficient (C_v)	Sensing Type	Flow Data on Page
RS2	5 800 (400)	5 075 (350)	0.05	Piston	11
RSH2	10 150 (700)	10 150 (700)			
RS4	1 015 (70.0)	406 (28.0) diaphragm 5 800 (400) piston	1.84	Diaphragm or piston	15
RSH4	5 800 (400)				

Figure 87: C_v Sizing Technical Data [72]

As can be seen from Figure 87 and the maximum inlet pressure for the RSH4 piston regulator is 5800 psig (psi gauge, same as psi) and the maximum outlet pressure is 5800 psig. Since the proof pressure of the Hydrazine tank is 35 Bar (3.5 $\times 10^6$ Pa), the aim of the regulator was to ensure that the inlet pressure from the tank to the system would be obviously less than the proof pressure. Since the outlet pressure was known to be 2.90 $\times 10^6$ Pa, as seen by state 4 in Table 10, the inlet pressure just had to be under 36.8 Bar, which was already very attainable. Next looking at Figure 87 and already knowing the maximum inlet and outlet pressures, the only C_v that would guarantee the system's pressure range was the RSH4 piston pressure regulator. After using this regulator to be modeled in the system EES code the following observations were collected. The inlet pressure at State 5, as can be seen in Table 10 had a pressure of 2.921 $\times 10^6$ Pa, equivalent to 423.6 psig; and the outlet pressure can be seen at state 4 as 2.905 $\times 10^6$ Pa, equivalent to 421 psig. Therefore, to have a very healthy factor of safety (FS) for the pressure regulator of 13.7, the C_v value rested at 1.84. The resulting pressure in the hydrazine tank yielded a factor of safety of 1.68 with respect to the burst pressure of 49 Bar (4.9 $\times 10^6$ Pa).

Next, in a similar manner to the process for sizing a liquid C_v as just described, the process for sizing a gas pressure regulator uses a very similar equation with a few adjustments. Equation 59 shows the adjusted C_v relation used in determining the size desired for the helium pressurant tank and the desired C_v value [70].

$$C_v = Q\sqrt{13.61 * P_{Inlet} * \frac{1}{SGT_{Inlet}}} \tag{59}$$

This time it was decided since the helium pressurant tank could withstand a large internal proof pressure of around 3.88×10^7 Pa, the tank pressure did not need to be limited much. The amount of helium needed to be able to fill both the helium tank and the hydrazine tank and also be at a pressure larger than that of the hydrazine tank. The helium pressure was elevated to 200 psi more than that of the hydrazine tank to ensure guaranteed pressure difference to ensure maintenance pressure throughout the system for the respective mass flows. Additionally, the volume of the helium tank was iterated to land at the volume of 2 m^3 to result in a safe pressure for the tank. Then the next action was to size up the gas pressure regulator using Equation 59. Once again values had to be transferred over to their respective English units to ensure the correct C_v result. Additionally, the temperature of the inlet had to be changed to units of Rankine as shown in the EES script results in Section 19.6 as $T_{press,adjust}$. The resulting pressure of the helium Pressure vessel was 4.301 $\times10^6$ Pa, yielding an FS of 10.81 with respect to the burst pressure of 465 Bar (4.65×10^7 Pa) [73].

Table 10: EES plumbing results.

	Re_i [−]	A [kg/m3]	$\mathbf{T}_i$ [K]	v_i [m/s]	del_{Pj} [Pa]	$\mathbf{H}_r$ [m]	$\dot{m}_i$ [kg/s]	P_i $[I'_a]$	Q_i [m/s]
1	5525	1005	283.2	0.1004	22.48	0.002332	0.1981	1.896E + 06	
2	1127	1005	283.2	0.02048	1.05	0.0001089	0.04039	1.620E + 06	
3	38784	1005	283.2	0.705	77.04	0.007989	1.391	3.516E + 06	
4	41573	1005	283.2	0.7557	4.722	0.0004896	1.491	2.905E + 06	.001444
5		1060	283.2	0				2.921E + 06	
6	2789	1005	283.2	0.0507	0.408	0.00004231	0.1	2.293E + 06	
7	11157	1005	283.2	0.8112	1754	0.1819	0.1	$2.292E + 06$	
8		7.313	283.2					$4.301E + 06$	.001444

14.3 Results

Throughout this section the thickness of the hydrazine tank was consistent with the analysis done earlier in the report in Section 8.3.2 and held at a thickness of 2.23 millimeters. After having completed the extensive observation of the effects created by the various head losses throughout the plumbing system and accounting for failure stipulations and uniform system assumptions the following observations were collected. Under the worst-case scenario of running the hydrazine delivery system at maximum capability by having all three delivery routes running at the same time; the hydrazine tank and helium pressurant tank would operate at a maximum operating pressure to yield factors of safety of 1.68 and 16.43 respectively. Both ratios indicate that the system operates safely even in a worst-case loading of the scenario, therefore, suggesting that much would have to malfunction with the refueler for the hydrazine delivery system to be a result of catastrophic failure. In the end, the helium pressurant tank was iterated to fall on its final volume due to iteration through the provided EES code system analysis and due to how it would be compatible with the rest of the structure. The main result of this entire plumbing analysis was to account for as many issues as possible that could be present in a real-life plumbing system and ensure that the system would be sound when applied to different uses as outlined. All of the EES script and supporting intermediary results and array tables are available in Section 19.6.

15 Final Computer-Aided Design

From the preliminary FEA that was completed, the CAD needed to be updated. The cross sections of all the structural elements needed to be changed in order to meet stress and weight requirements. Additionally, many components of the spacecraft needed to be added that had not been modeled yet. For example, the Whipple shielding was modeled and significantly changed the layout of the components of the spacecraft. Also, the size of the pressurant tank was updated as well as the mounting method of both the hydrazine tank and pressurant tank, which changed the overall size of the structure. Additionally, factors such as manufacturability and the assembly of the spacecraft were considered that had an impact on the final design. Many of the connections between the parts and subassemblies of the spacecraft had not been thought out at the time of preliminary CAD. However, many of the fastening techniques, such as welds, bolts, and rivets, are included in the final CAD. A rendering of an isometric view of the final design is shown in Figure 88. This displays the added Whipple shielding as well as the updated solar panels, robotic arm, and RCS thruster assemblies.

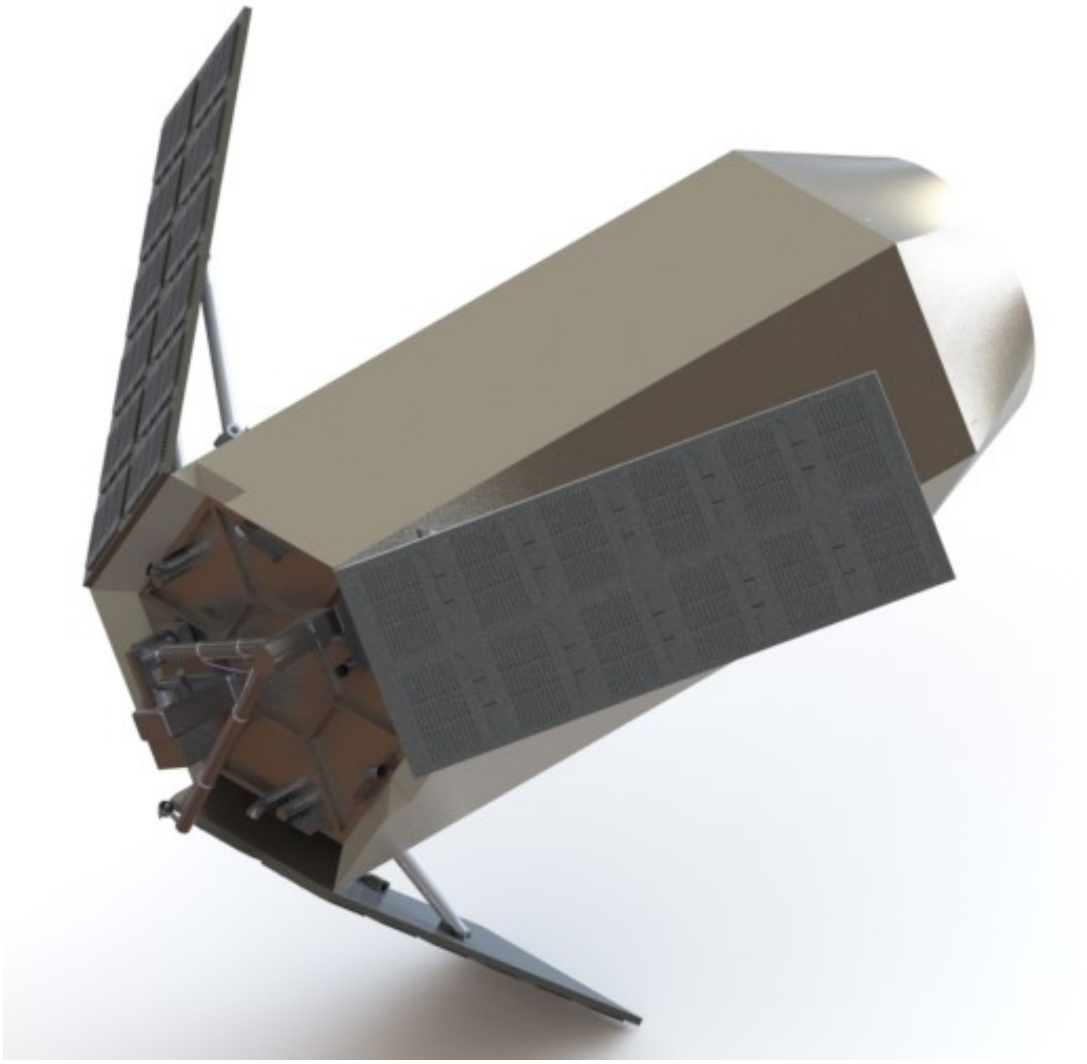

Figure 88: Final CAD rendering of an isometric view.

A rendered view of the top portion of the final CAD is shown in Figure 89. This view gives a better view of the updated arm, and the added cutouts for the RCS thrusters, as well as giving a glimpse into the updates to the structure.

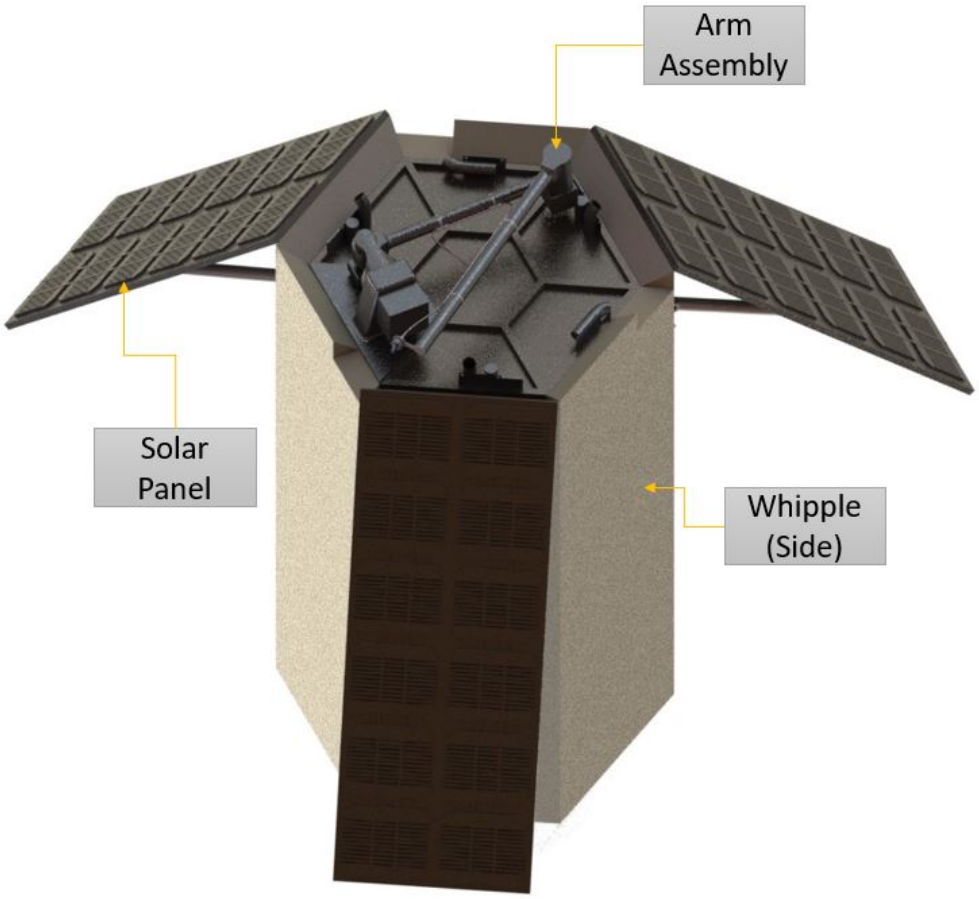

Figure 89: Final CAD rendering of a top view.

Figure 90 displays a view of the bottom of the final CAD rendering, showing the updated geometry for the bottom portion of the structure. It also displays the updated connections for the main thrusters, which are bolted to the bottom plate of the structure. Note that the fasteners are not shown but there are holes for the specified fasteners. The updated payload adapter is also shown.

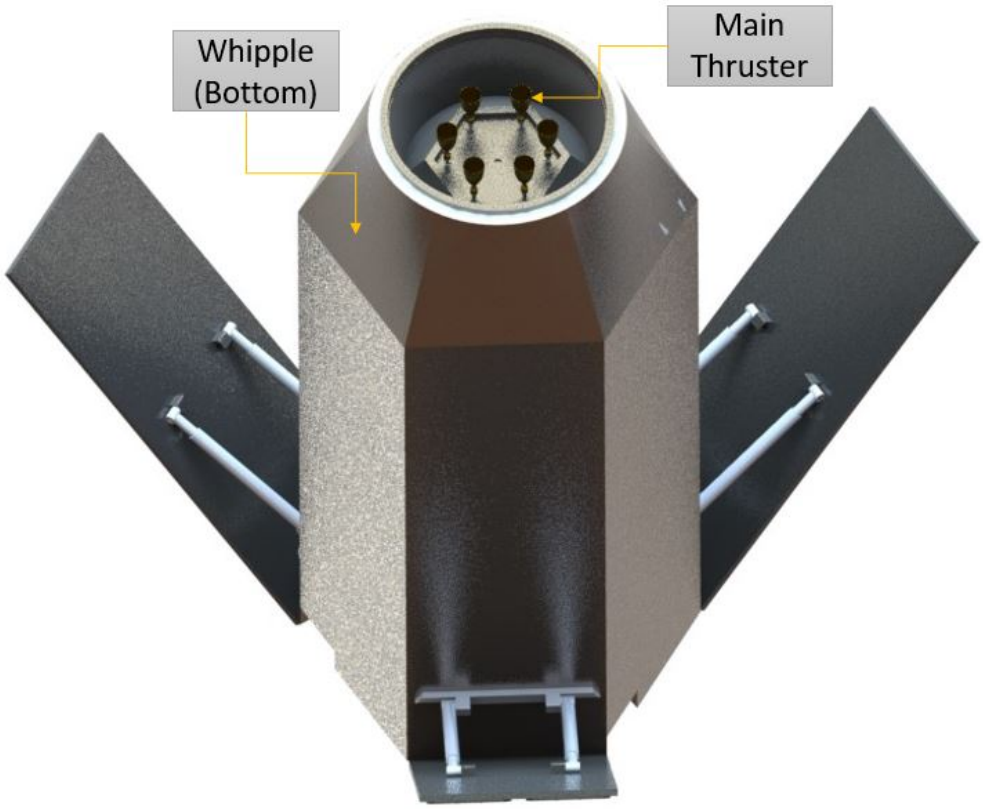

Figure 90: Final CAD rendering of a bottom view.

Another rendering of the final CAD is shown in Figure 91. This rendering is an isometric view of the final CAD with the Whipple shielding and solar panels hidden. This allows for the structure and all other internal components to be seen. The updated pressurant tank size, tank mounting plates, GNC pack, RCS mounts, valves, and more can all be seen with the Whipple shielding and solar panels hidden.

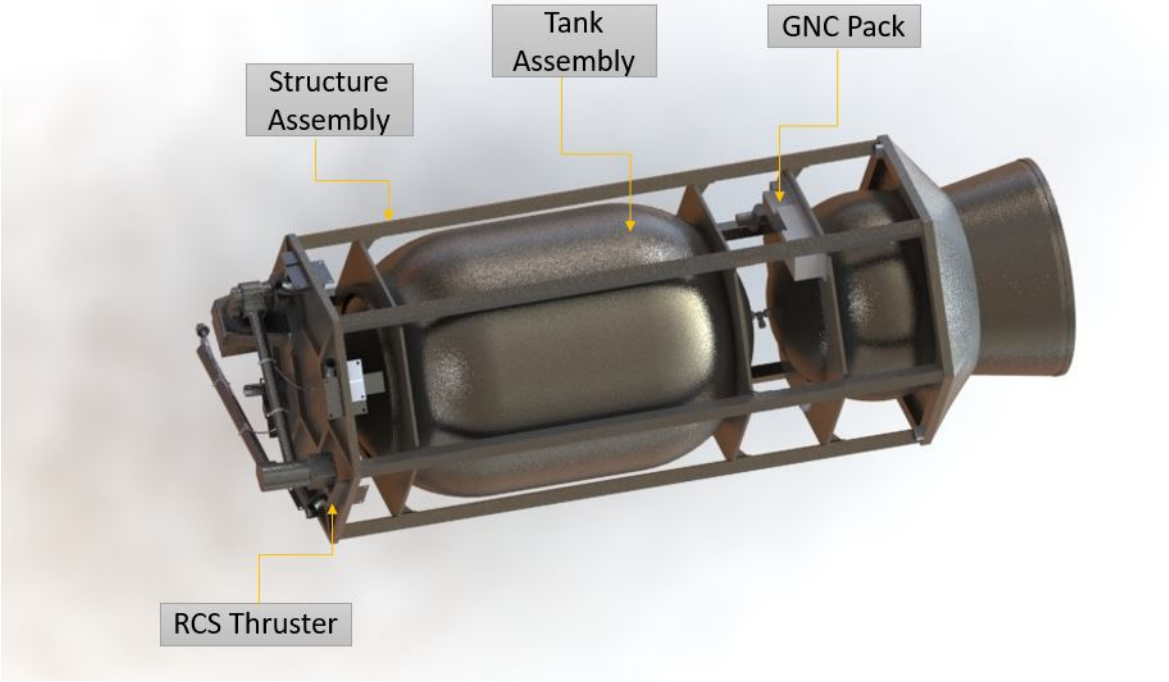

Figure 91: Final CAD rendering with solar panels and Whipple shielding hidden.

Details of each of the main subassemblies within the final CAD are outlined in the following sections. This will cover the changes from preliminary CAD, connections, as well as manufacturing techniques. Additionally, a detailed table of all the parts and subassemblies included in the final design and their numbers are shown in Section 18.

15.1 Structural Assembly

A rendering of the final CAD structure subassembly is shown in Figure 92. This displays the updated structure as well as the tank subassembly.

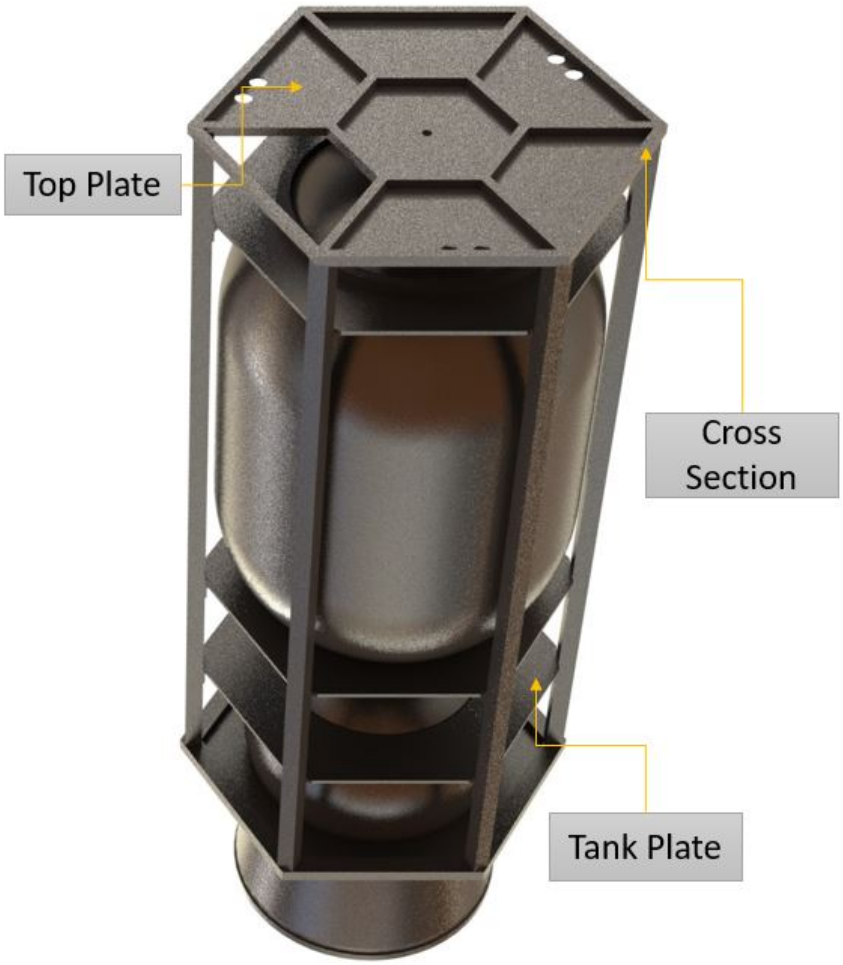

Figure 92: Final CAD structure rendering.

The material of the final structure is specified as Ti-6Al-4V. Every part of the final structure is manufactured out of this material to allow for the structure to be welded together. There are no fasteners in the final structure subassembly as every part will be welded together. This manufacturing technique is not the most repeatable, but this is a realistic assembly method for a one-off satellite. The tank subassembly must be included in the final structure subassembly in order to obey the order of assembly. The tank subassembly would first be put together and then the structure would be assembled around it.

Some of the main differences between the preliminary CAD structure and the final CAD structure are the cross sections of the bars, the geometry of the bottom portion of the structure, and using plates to mount the tank. The cross-section and sizing of the bars in the final CAD follow the specified dimensions in Table 6, which come from the initial FEA

results. The geometry of the payload adapter changed due to the changing cross-section of the tapered beams, and the size of the pressurant tank also changed due to plumbing calculations. Both caused the geometry of the bottom portion of the structure to change to match the new pressurant tank and tapered beams. Holes were also added for the mounting of the main thrusters. Plates were also added to the top and bottom of the structure assembly. The top plates also include holes for the RCS thrusters to fit into. The method of attaching the tank to the structure was changed from beams in the preliminary CAD to plates in the final CAD. Brackets were also added to support the plates and allow for a greater area to weld to. A rendered side view of the final CAD structure subassembly is shown in Figure 93.

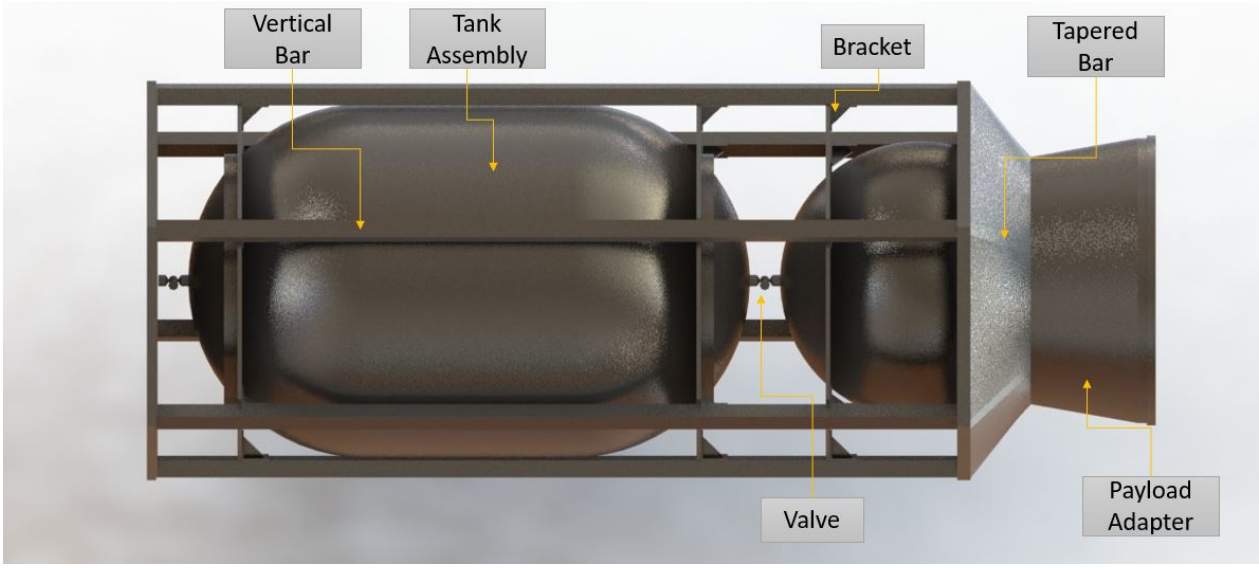

Figure 93: Final CAD structure rendering side view.

15.2 Arm Assembly

A rendering of the final CAD for the robotic arm is shown in Figure 94. This displays all the arm parts as well as the tubing which would be connected to the structural assembly and hydrazine tank as seen in Figures 88 and 89.

Figure 94: Final CAD rendering isometric view of the arm with example tubing shown

The material of the final arm is specified as Ti-6Al-4V. The material used for the tubing should be Teflon tubing - the most commercially accessible flexible non-metal that was found to be compatible in Table 3. This will allow for the structure to be welded together at multiple points, and most notably the arm base is to be welded with the structure which is also made of Ti-6Al-4V. The arm will be manufactured in separate steps. The arm contains a mixture of purchased parts and one-off parts which allows flexibility in manufacturing, however, when possible the cheapest and fastest manufacturing solution is preferred.

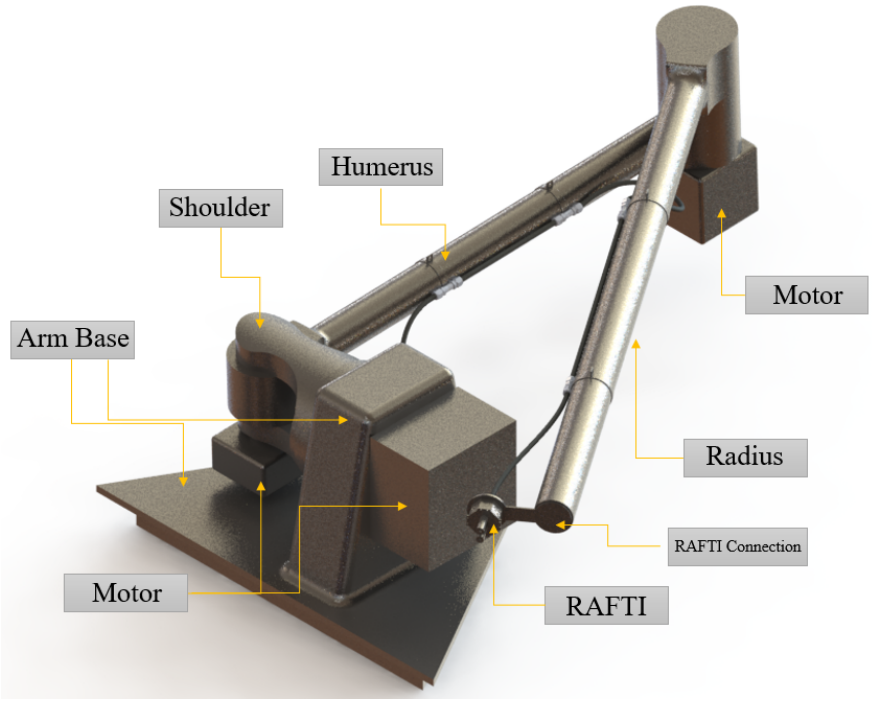

Figure 95: Final CAD arm nomenclature.

To best explain the manufacturing considerations, Figure 95 shows the nomenclature used for each arm part.

15.2.1 Arm Base

Figure 96 is shown as a part of the main arm assembly.

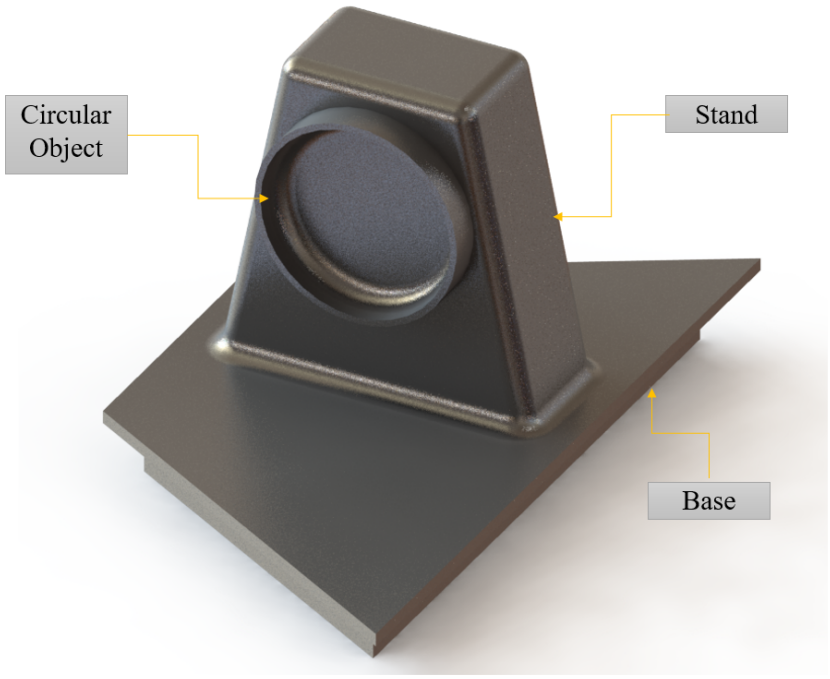

Figure 96: Final CAD structure labeled arm base.

The arm base is composed simply of a plate base, a stand, and a circular object to connect fit with the joints. The base could be manufactured by starting with a block of titanium and band sawing out the larger trapezoidal shape. Then, the smaller trapezoidal shape could be milled into the specification size and also the larger trapezoidal shape can be milled to exact dimensions. The inside of the base could be further milled by milling out the inside from the bottom end as seen in Figure 96.

The stand should be manufactured with thinner walls to save weight. An optimization could be done in the future to specify a thickness that maximizes sturdiness and weight loss. The stand could start as a plate and be bent into its shape - however, this piece is a one-off and the circular object would have to be welded. To avoid this, the stand and circular object could be manufactured with a CNC milling machine.

The stand and base could either be attached with fasteners or welded together. The top edges of the base as seen in Figure 96 will be welded to the structure. Alternatively, the base could be connected with the structural tubing with a rivet nut tool.

The shoulder could similarly be CNC milled to specifications because it is a one-off. The circular object in Figure 96 could be fitted with a bearing on the inside and the shoulder could be press fitted into the bearing to provide extra structural stability as compared to if there was no circular object. It would be important to cover the bearing thereafter. The shoulder would be connected to the motor with purchased robotic joints and the axle that connects them that would go through the stand. The hole for the axle is not shown in Figure 96. Future work should go into making all robotic arm connections such as the arm base

from simple geometry such as cylindrical members to avoid welding so many connections and for easier manufacturing.

15.2.2 Humerus

The humerus of the arm is shown in Figure 97 to show a part of the full assembly.

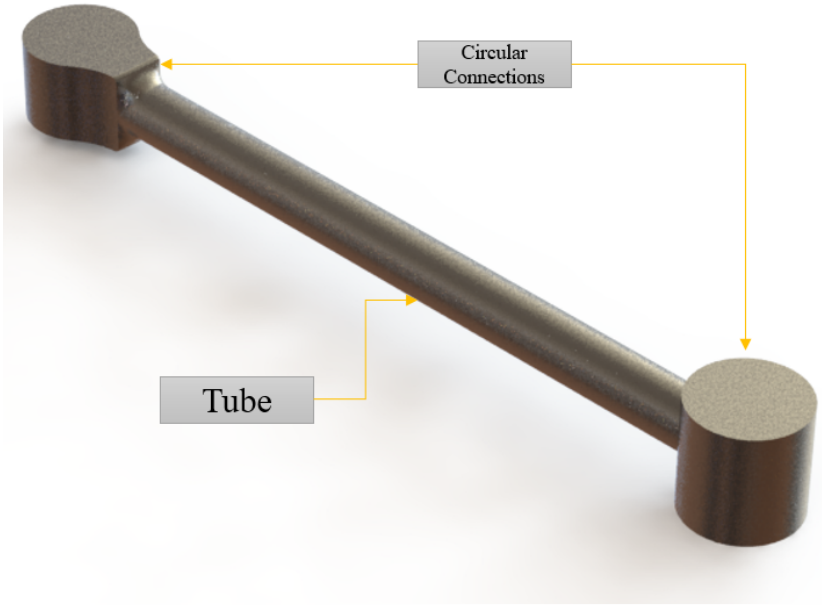

Figure 97: Final CAD structure labeled for the humerus.

15.2.3 Radius

The humerus and radius are very similar and can be manufactured similarly. The hollow tubing could be purchased. The circular connections could be manufactured using a mill to achieve the exact dimensions and also to tap the holes that allow space for the robotic joint which will be connected with fasteners and the axle that connects the joints to the motor. The tubing and circular connections should be welded together; there is great weight optimization comes from a tubed member rather than a solid rod.

15.2.4 RAFTI Valve and RAFTI Connection

The RAFTI part is a purchased part from Orbit Fab. For the time being, the dimensions of the RAFTI are fixed. An example of how SpacExxon plans to incorporate it bolted the outer RAFTI structure to the RAFTI connector. It was designed according to [5].

15.2.5 Motors

The spacecraft's arm is using frameless servo motors because they are highly reliable, have a high ratio of torque to inertia and can be used in constant torque cases with high accuracy [74]. Servo motors also provide the advantage of low power requirements when combined with a large gear ratio. It would be easiest to purchase a high-quality servo motor that meets the geometric and torque specifications and minimizes average power requirements

and weight - there are plenty available on the market and for high-end uses, one could even purchase a custom-specified motor from a company such as Maxon, a motor and robot joint manufacturer [75]. In space, temperature limits are also important when considering a motor.

15.2.6 Robot Joint Overview

Figure 98 shows an exploded view of the parts that go into a robot joint that can be custom-ordered from the joint manufacturer, Maxon [75].

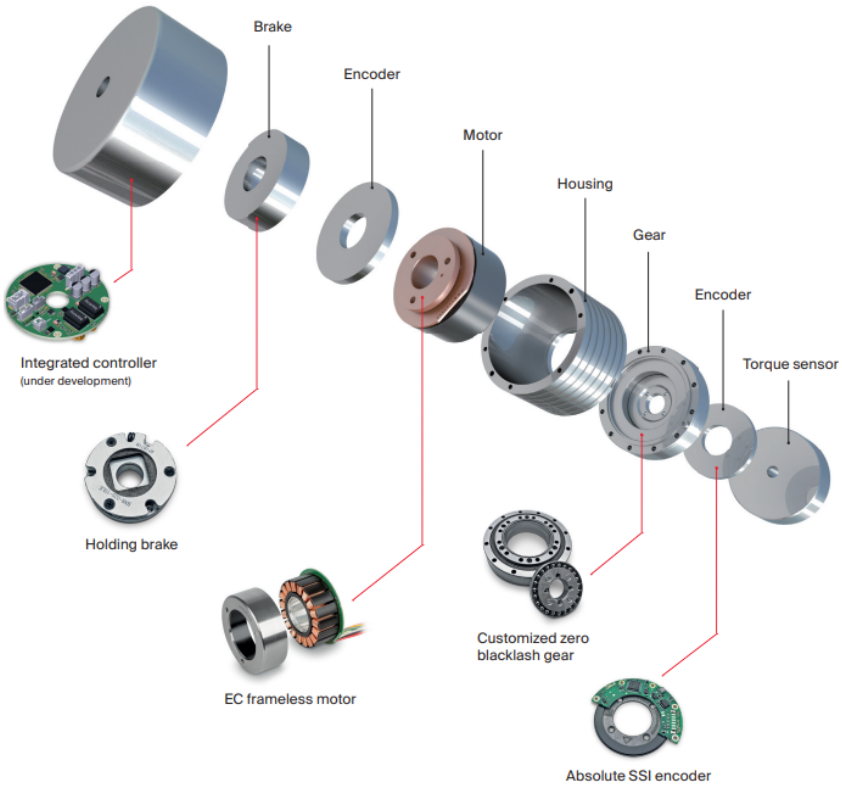

Figure 98: Robot joint exploded view [75].

An integrated robotic joint controller is vital for a compact assembly that requires high accuracy and reliability [76]. It is a growing design trend in robotic applications to use an integrated robot joint not only for axial coupling purposes but also to drive a high-ratio gear set [76]. SpacExxon has not decided on a specific robotic joint for joint connection, but the following subsections will describe the considerations for the robotic joint. To briefly describe, an encoder provides high resolution on the output, the brake is useful to control unwanted motion, and the controller can be specified to be driven by movement or torque output. Precision gearing can also help provide zero backlash, something that is very important in a motor that has a high gear ratio because of the potential inertial obstacles that can cause positioning faults [76]. In summary, the robot joint choice will be one of the most important factors in controlling the motion of the robotic arm.

15.2.7 Robot Joint Braking

One of the largest headaches in robotic movement is an uncontrolled motion by a robot. Therefore, robots that incorporate servomotors need brakes to hold torque once the motor moving the joint has stopped. This could also help provide a safety stop in case of an emergency [77]. The key parameters to choosing a brake type depend on the torque, speed, backlash, response time, weight (of the brake and the arm), the diameter of the shaft, mounting configuration, maintainability, and price [77] [78]. Set brakes typically have advantages over permanent magnet brakes in the case of machine safety, maintainability, dynamic stop, and cost factors. Permanent magnets are favored for zero backlashing, smaller footprint, speed, or rapid cycling [78]. In the case of SpacExxon's arm, the desired brake would be one that has low speed and torque favorability, zero backlash, minimizes any need for maintenance, and a smaller footprint and weight are desired. For these cases, the permanent magnet brakes provide the greatest advantage. A permanent magnet brake would be purchased as a feature of the selected integrated robot joint. Figure 99 shows a visual of the braking mechanism for a permanent-magnet friction brake that SpacExxon would plan to use in the robot joint.

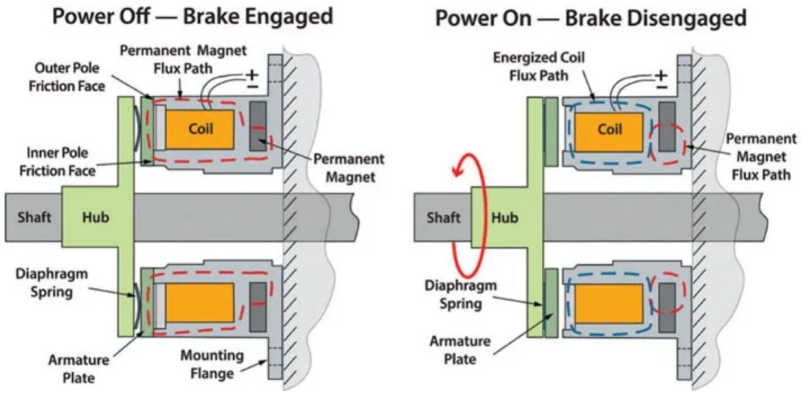

Figure 99: Mechanism visualization of a permanent-friction magnet brake [75].

15.3 Tank Assembly

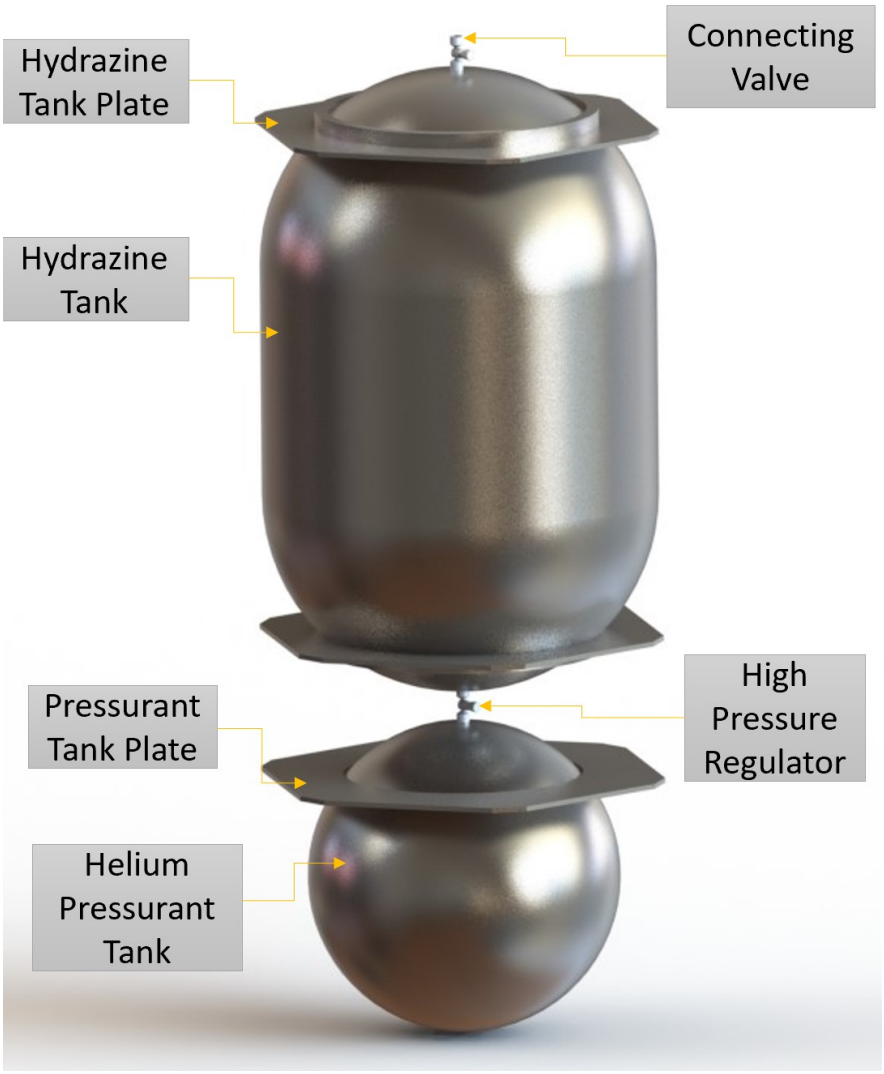

Figure 100: Final CAD structure rendering tank assembly.

The tank assembly is one of the most important sub-assemblies in this entire satellite as it is the main holding that the entire refueling mission is structured around. The tank assembly consists of 11 parts total as detailed in the drawings packet. Before the hydrazine tank and the pressurant tank are attached together the hydrazine tank plates are welded with titanium to the collars on each side of the tank that were welded on by the manufacturer. Then the pressurant tank plate is put on the side of the sphere with the connecting nipple. Next, the hydrazine tank and the pressurant tank are attached together with two pipe-reducing connecting valves, one valve reducing down from each tank towards each other and fastened to the high-pressure regulator via threaded holes. The reducers are then welded with titanium to the nipple of each tank to prevent any pressure losses. Once connected together, the two tanks are mostly assembled. The last portion of the assembly is to weld on more reducer-regulator-reducer assembly onto the end of the hydrazine tank that would lead to the rest of the delivery system.

Once manufactured, the tank assembly is placed in the main assembly and attached with brackets on the hydrazine and pressurant plates to the main structure. Therefore, the helium pressurant tank is held stably in place by the bottom plate of the main frame and the pressurant plate that is bolted to the frame as just described. All components other than the high-pressure regulators are made from the same grade of titanium which allows for them all to be welded and adhere correctly to one another. This final rendition of the CAD sub-assembly varies from the preliminary CAD with the addition of the correctly sized helium pressurant tank and the respective connection points between the two tanks via the regulators. Additionally, instead of having crossbars support the hydrazine tank on top and bottom, the hydrazine and pressurant tank plates were swapped in with the collars added to the hydrazine tank and secured with brackets to the main structural frame adding more integrity to the refueler.

15.4 Solar Panel Assembly

The solar panel assembly is integral to the power generation and stowed profile of the spacecraft. To not exceed the diameter of the payload volume, the solar panels must be extended after deployment. The specifications for the solar cells are given in 8.6.1.

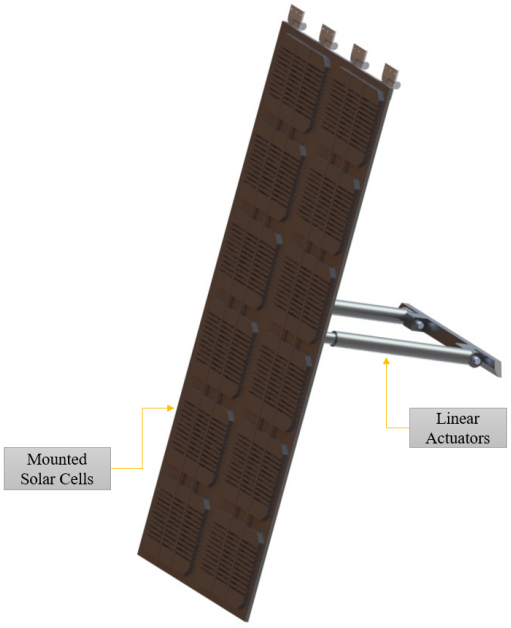

Figure 101: Final CAD solar panel assembly front view.

The main solar arrays have an area of 4.725 m^2, which is mainly actuated by two linear actuators. These actuators could potentially be electrically extended through the conversion of rotation to linear motion by a worm gear and motor, or alternatively, the use of the helium pressurant tank could pressurize these actuators. The full integration of the linear actuators into an electrical or hydraulic subsystem remains future work. To allow for the fixed rotation of the solar panels about a single plane, interference fit bearings are housed within the solar panel and a 40 mm axle. This assembly is then repeated four times, for each rotation point. The actuators interface with a mounting bar, that has attachment points to bolt through

the Whipple shielding. Though the Whipple shielding is not heavily structural, it is assumed that the stresses on the assembly during extension will be low.

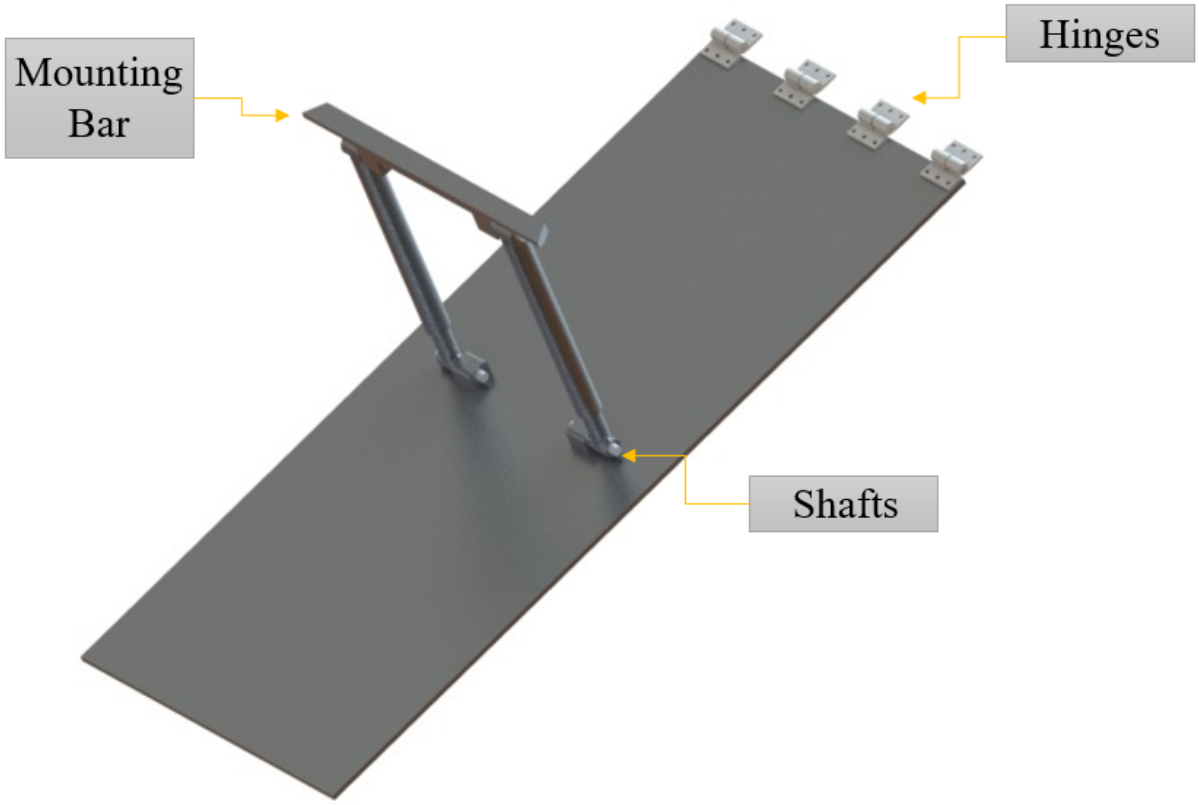

Figure 102: Final CAD solar panel assembly back view.

For constraining the axis of rotation for the array, four heavy-duty hinges were obtained from McMaster-Carr, each with a maximum bearing capacity of 1814 kg. The entire solar panel assembly is 532.9 kg, where the solar panel, actuator parts, and mounting bar are all Al-6061 T6. This was chosen because there is no welded connection to the spacecraft, and the aluminum alloy presented a strong and lightweight alternative to titanium. Three of these assemblies are present upon the spacecraft, giving a 120° axisymmetric design. The hinges and the mounting bar are fastened to the spacecraft with M14 and M10 bolts respectively.

15.5 Propulsion Elements

The thrusters used on the refueler are all purchased from Moog, as mentioned in Section 8.1. No CAD models were provided, so best approximations on nozzle shape were taken using given data sheets [35]. A Rao parabolic nozzle shape from [36], was used for the MONARC445 thrusters. The six main thrusters are fastened to a hexagonal plate to reduce stress on the lower structural components. This plate is 10 mm thick specified from the structural analysis. This plate also has a 0.05 m diameter hole for fuel pipes. Figure 103 shows their placement.

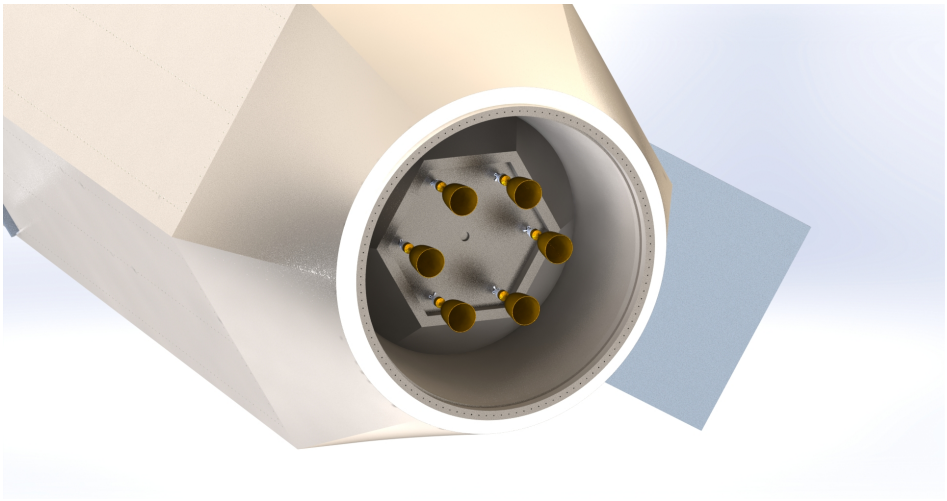

Figure 103: Six MONARC445 thrusters on the bottom of the Refueler.

The MONARC90-LT thrusters had similar data available and assumptions were made about their design as well. The nozzle shape of the RCS thrusters was approximated to have a constant radius throughout, with a 30° bend. The five RCS thrusters are fastened to custom brackets at the top of the satellite to avoid whipple shielding contact. The custom bracket is CNC-milled from the same titanium alloy, Ti-6Al-4V, to allow for welding to the structural beams shown in Figure 104. An alternating pattern of outward-facing and upward-facing thrusters was used due to the placement of solar panels. An outward-facing RCS thruster would have destroyed the upper hinges of the solar panels. Cuts were made in the Whipple shielding to allow for the outward-facing RCS thrusters to work properly without Whipple shielding interference. Another outward-facing thruster would have been used but was removed to make room for the arm base which occupies a section of the structural beams. This is a comparable decision because the satellite will rarely need to rotate about its central axis due to the large reach of the arm. Figure 104 shows their placement and orientation.

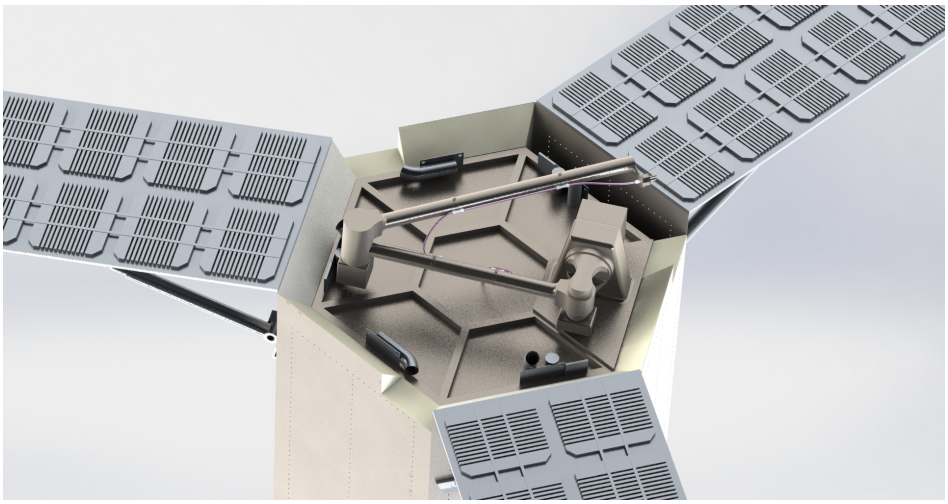

Figure 104: Five MONARC90-LT thrusters on the top of the spacecraft.

16 Future Work

Though the previous sections attempt to describe the design of the components, subsystems, mission, and more, there is still heavy iteration and redesign to complete in order to be confident in a mission proposal to a true launch provider like SpaceX, NASA, or black Origin. Design iteration would be necessary to complete in parallel for the orbital mechanics calculations, the FEA, fluids calculations, and the CAD, such that all contain accurate masses and depictions of the system at their specified level.

The orbital mechanics would be iterated with the structural mass, such that the propellant mass contains the required amount for orbital transfers for the mass of the structure. The general mission would need to be modeled in mission analysis software like STK or GMAT to have a secondary check for the orbital mechanics calculations.

The structural design would require further optimization, likely modeling subassemblies and making smaller models that agree with analytical calculations. Fasteners would have to be implemented and iterated with a spacecraft fastener analysis standard like NASA 5020 [79]. This current analysis is bottlenecked by the analysis software that does not provide complete control of elements in the graphical interface, for example, RBE2, RBE3, CBAR, CBUSH, and other elements are not quickly available for selection. Ansys also does not contain a professional CAD to work in parallel. Therefore it is likely that a new FEA package would be necessary for complete analysis.

A transient thermal analysis would be necessary to completely model the stresses within the spacecraft as a function of the orbital position around the sun, though these stresses would likely be small. The thermal analysis would also ensure that all electrical components could withstand the temperature gradients within the spacecraft. Also, an acoustic analysis would also be necessary to simulate the launch environment.

General electrical component sizing, connections, power draw, and wire harnessing would need to be defined further such that the integration of the avionics could be documented. Communication bands and antenna positioning is also of concern. Motors and actuators for control devices, like the CMGs and the solar panel linear actuators, would need to be defined. Along with those control actuators, additional RCS thrusters will also likely be necessary to provide rotation in both directions for each primary axis, which would likely result in 12 total RCS thrusters. The CMGs would need to be analyzed such that their gyroscopic moments can be oriented in the primary axes. The development of a tuned classical control system would need to be defined to allow for the dynamics of the spacecraft to be modeled with control. Navigation algorithms with optical or uplink systems would need to be used for the spacecraft to reckon with its own position.

The arm would need to be modeled in a robotic software like ROS or Simulink Simscape, with a specific control system for the motors. Autonomy with a computer vision system and correction for relative motion between spacecraft during refueling will need to be modeled. Additionally, much of the arm would need to be finalized. These include finalized specific motors, robotic joints, and dimensions for the humerus and radius. The arm base would potentially need to be re-designed to fit the structure if any changes are made to the structure. The piping for fluid flow from the tank to the arm and RCS would also be necessary to model in CAD, such that their relative positions are known.

Manufacturing methods for all parts would need to be optimized such that welding is not the primary method of part connection, and multi-axis CNC milling is not the main method of manufacturing. A prime example of this is in the current design of the arm.

Material specifications will also need to be iterated such that the strength-to-weight ratio of un-welded parts is optimized, rather than simply choosing Ti-6Al-6V. Further analysis on the tank would need to be iterated in conjunction with the fluid calculations such that the welds, plates, and thickness of the tanks are all converged upon. It is also likely that instead of using EES, a large thermodynamic system should be implemented into MATLAB such that further understanding of the method of iterative solution can be understood.

In general, it takes an entire company of electrical specialists, aerospace engineers, analysts, software developers, technicians, machinists, and managers to organize the successful production of a satellite. Though this is a conceptual design, it has been unclear the true requirements of five undergraduate engineers such that they could provide a meaningful design of this mission without leaving a large portion of the project up to interpretation or referring to the system as a "black box". Ultimately, there is a large amount of work done before SpacExxon launches on an orbital SpaceX Starship launch vehicle, but the concept of saving satellites in orbit that are failing due to loss of propellant is a novel and exciting idea that should be pursued further.

17 Conclusion

In summary, this report contains preliminary design, component selection, orbital specifications, subsystem specifications, fluid system design, structural analysis, and final iteration CAD for the refueling spacecraft. This report is an addition to a preliminary sizing and structural analysis report where all changes made to the previous report are changed to black text. Previously, preliminary CAD, orbital mechanics calculations, component sizing, and preliminary structural analysis were included. This report contains further information on the final design of the CAD and updated fluid, structural, dynamic, and orbital analyses.

The structural analysis was iterated to take into account a random vibration launch profile for lateral and axial excitation. This ultimately increased the stresses in the model, requiring iteration of the structure further than what is defined in the CAD. Similar static analyses were redone with the new changes to the structure. Stresses were found to be below yield for all analyses besides singular point PSD normal stress responses at their resonant peaks. The fluid system calculations were also iterated upon to more completely model the number of outlets and fluid interfaces in the system, and exact dimensions for the pressurant tank were acquired which were ultimately used in the structural model for the pressurant tank.

The orbital mechanics calculations were also improved to include a remodeled 10-stop mission for SpacExxon, where propellant and burnout masses were computed at every stage. The destinations for the missions were also changed. The final iteration of CAD that is included with this report was also completed, where 20 of the most significant subassemblies and parts are drawn to ANSI standards. These manufacturing drawings are the most detailed manufacturing and dimensional description of the satellite. Overall, a complete preliminary design of a spacecraft is included in this report.

18 Table of Part Numbers

Table 11: Part Numbers.

Subassembly	Sub-subassembly	Filename	Part Number
Spacecraft Assembly			001
Propulsion			
		MONARC-90LT	104
		MONARC-90LT (Mirrored)	105
		MONARC-445 Nozzle	101
		MONARC-445 Injector	102
		RCS Base	108
		RCS Subassembly	109
Tank Assembly			200
		Hydrazine Tank	201
		Pressurant Tank	202
		Hydrazome Tank Plate	203
		Pressurant Tank Plate	204
		Connecting Valve	205
		4289T212 Valve	206
GNC Pack			300
		Flight Computer	301
		IMU	302
		SPOThermal	303
		Avionics Plate	304
		Avionics Pack	305
		CMG	306
		Star Tracker	307
Structure			400
	Vertical Bar Assembly		401
		Vertical Bar	422
		Vertical Bar Caps	423
		Tapered Beam	402
		Payload Adapter Attachment	403
		Payload Adapter	404
		Top Plate	405
		Top Plate with RCS Cutout	406
		Bottom Plate	420
		Top Central Plate	421
		Bottom Tapered Plate	424
	Cross Section		407
		Inside Bar	408
		Outside Bar	409
		Cross Bar	410

Table 12: Part Numbers Continued.

Subassembly	Sub-subassembly	Filename	Part No.
	Cross Section Bottom		411
		Inside Bar	408
	Plate assembly		412
		Plate divider	413
		Outside Bar	409
		Brackets	414
		Top Hex Slice Plate	430
Solar Panels			500
		Solar Panel	501
		Solar Panel Actuator	502
		Solar Panel Actuator Female	503
		Solar Panel Actuator Mount Bar	504
		4668K261 - Ball Bearing	505
		40mm Shaft	506
		1828A57 - Heavy Duty Hinge	507
Robotic Arm			600
	Arm Base		601
		Base Attachment	610
		Base	611
		Servo Motor	612
		Shoulder	602
		Humerus	603
		Radius	604
		RAFTI Valve	605
		Connector RAFTI	606
		Bottom Pipe Clamp	607
		Top Pipe Clamp	608
		Tubing	609
Whipple Shield (Side)			700
		Whipple Front Plate	701
		Whipple Aluminium Foam	702
		Whipple Back Foam	703
Whipple Shield (Bottom)			800

19 Appendix - Source Code

19.1 Orbital Mechanics Code (MATLAB)

```
%% EMA569 - Orbital Mechanics
% Aidan Butula

clear all; clc; clf; close all;

%% Earth Conditions

% constants
g_const     = 6.6743e-11;                                    % [
   m^3 kg^-1 s^-2]
mu          = 3.986e14;                                      % [
   m^3/s^2]
m_earth     = 5.972e24;                                      % [
   kg]
r_earth     = 6371e3;                                        % [
   m]
g_e         = 9.807;                                         % [
   m*s^2]
isp         = 300;                                           % [
   s]
%alt         = linspace(300e3, 1000e3, 8);                    %
   [m]
%r1          = r_earth + alt;                                 %
   [m]
%delta       = linspace(0, 180, 19);                          %
   [deg]

% velocity (circular)
%v_circ = sqrt(mu./r1);                                      % [m/
   s]

% semi-major axis
% for i = 1:length(r1)
%     for j = 1:length(r1)
%         a(i,j) = 0.5*(r1(i) + r1(j));                       % [m]
%     end
% end



%% Plane Change Maneuver

% for i = 1:length(v_circ)
```

```
%     for j = 1:length(delta)
%         dv_pc(i,j) = 2*v_circ(i)*sind(delta(j)/2);
%             % rows are with different changes in angle
%             % cols are with different circular velocities
%         dv_pc_norm(i,j) = dv_pc(i,j)/v_circ(i);
%     end
% end
%
% figure;
% plot(delta, dv_pc_norm)
% xlabel('\delta [deg]')
% ylabel('\Deltav/v [-]')
% % title('Plane Change Orbit Maneuver')
% grid on


%% Hohmann Transfer Maneuver

% for i = 1:length(v_circ)
%     for j = 1:length(v_circ)
%         dv1_h(j,i) = sqrt(mu/r_leo(i))*(sqrt(r_leo(j)/a(i,j))
   -1);
%         dv2_h(j,i) = sqrt(mu/r_leo(j))*(1-sqrt(r_leo(i)/a(i,j
   )));
%     end
% end
%
% dv_h = dv1_h+dv2_h;
% % rows are initial altitude
% % cols are final altitude
%
% time_h = 2*pi*a.^(3/2)/sqrt(mu);
%
% figure;
% plot(alt,dv_h)
% xlabel('final altitude [m]')
% xtickformat("auto")
% ylabel('\Deltav [m/s]')
% % title('Hohmann Transfer Orbit Maneuver')
% grid on
% legend('initial alt = 300 km','initial alt = 400 km','initial
    alt = 500 km','initial alt = 600 km', ...
%     'initial alt = 700 km','initial alt = 800 km','initial
   alt = 900 km','initial alt = 1000 km',Location='Best')


%% Hohmann w Optimally Split Plane Change
```

```
% for i=1:length(r_leo)
%     for j=1:length(r_leo)
%         vp = sqrt(mu*(2/r_leo(i)-1/a(i,j))); %km/s
%         va = sqrt(mu*(2/r_leo(j)-1/a(i,j))); %km/s
% %         if vp < 0
% %             vp = NaN;
% %         end
% %         if va < 0
% %             va = NaN;
% %         end
%         for k=1:length(delta)
%             syms alpha1 dv1_opt dv2_opt
%
%             eqn1 = dv1_opt == sqrt(vp^2+v_circ(i)^2-2*v_circ(
   i)*vp*cosd(alpha1));
%             eqn2 = dv2_opt == sqrt(va^2+v_circ(j)^2-2*v_circ(
   j)*va*cosd(delta(k)-alpha1));
%             eqn3 =
%
%             sol = vpasolve([eqn1, eqn2, eqn3], [alpha1,
   dv1_opt, dv2_opt]);
%             alpha(i,j,k) = sol.alpha1;
%             if alpha(i,j,k) <= -180
%                 alpha(i,j,k) = alpha(i,j,k) + 360;
%             elseif alpha(i,j,k) < 0
%                 alpha(i,j,k) = alpha(i,j,k) + 180;
%             elseif alpha(i,j,k) >= 180
%                 alpha(i,j,k) = alpha(i,j,k) - 180;
%             elseif alpha(i,j,k) > 90
%                 alpha(i,j,k) = alpha(i,j,k) - 90;
%             end
%             dv1_opt(i,j,k) = sol.dv1_opt;
%             dv2_opt(i,j,k) = sol.dv2_opt;
%         end
%
%     end
% end


%% Example Mission

N = 10;                             % number of runs
mass_stage = zeros([11, N]);
legend_text = zeros([1, N]);
m_bo = 1500;                          %
for i=1:N
```

```
    % Generate random r1, r2, and delta values
        r1 = randi([300e3 1000e3],1,10) + r_earth;
        r2 = r1(2:end);
        r2(end+1) = randi([300e3 1000e3],1) + r_earth;
        delta = 2*rand(1,10);
        delta = sort(delta);

    mass_stage(:,i) = hohmann_planechange(r1, r2, delta, m_bo);
    legend_text(i) = "Run " + num2str(i);

end

%average of each run at x stage, appended to mass_stage matrix
mass_stage(:,N+1) = mean(mass_stage, 2);
legend_text(N+1) = "Average";

%% plotting
figure;
hold on
bar(mass_stage)
ylabel('Mass [kg]')
xlabel('Stage')
grid on
hold off


%% Hohmann-SplitAngle function

function m_stage = hohmann_planechange(r1, r2, delta, m_bo)

% constants
g_const     = 6.6743e-11;                                    % [
   m^3 kg^-1 s^-2]
mu          = 3.986e14;                                      % [
   m^3/s^2]
m_earth     = 5.972e24;                                      % [
   kg]
r_earth     = 6371e3;                                        % [
   m]
g_e         = 9.807;                                         % [
   m*s^2]
isp         = 300;

% Hohmann w Optimally Split Plane Change
a = 0.5*(r1+r2);                                             % [
   m]
v_circ1 = sqrt(mu./r1);                                      % [
```

```
   m/s]
v_circ2 = sqrt(mu./r2);                                          % [
   m/s]
vp = sqrt(mu*(2./r1-1./a));                                      % [
   m/s]
va = sqrt(mu*(2./r2-1./a));                                      % [
   m/s]

for i=1:(length(r1))
%     varLimits = [0,90.0; 0,2e3; 0,2e3];
    syms alpha1 dv1 dv2
        eqn1 = dv1 == sqrt(vp(i)^2+v_circ1(i)^2-2*v_circ1(i)*vp
           (i)*abs(cosd(alpha1)));
        eqn2 = dv2 == sqrt(va(i)^2+v_circ2(i)^2-2*v_circ2(i)*va
           (i)*abs(cosd(delta(i)-alpha1)));
        eqn3 = vp(i)*v_circ1(i)*abs(sind(alpha1))/dv1 - va(i)*
           v_circ2(i)*abs(sind(delta(i)-alpha1))/dv2 == 0;

    sol = vpasolve([eqn1, eqn2, eqn3], [alpha1, dv1, dv2]);
    dv1_opt(i) = sol.dv1;
    dv2_opt(i) = sol.dv2;
    alpha(i) = sol.alpha1;

end

dv_opt = dv1_opt+dv2_opt;


% Rocket Propulsion
m_stage = zeros([length(dv_opt)+1,1]);
m_stage(1) = m_bo;
for i=1:length(dv_opt)
    m_stage(i+1) = m_stage(i)*exp(dv_opt(i)/(g_e*isp))+100;
end
m_stage = flip(m_stage);

end
```

19.2 Orbital Mechanics Sample Mission Results

Results from Section 19.1 are shown where the rows are each stage and the columns are each test run. The last column is the average of every value in the row. Units are in $[kg]$.

Table 13: Sample Test Run Data

		Test Run										
		1	2	3	4	5	6	7	8	9	10	Avg.
Stage	1	8264	6092	6900	5975	6377	8409	6836	7736	6887	8245	7172
	2	7046	5272	6229	5365	5782	7620	6052	7001	6196	6011	6257
	3	5075	4744	5370	3958	5258	6413	4625	6460	4627	5500	5203
	4	4559	3796	4069	3547	4023	4841	4155	5012	4079	5114	4320
	5	4194	3443	3221	3185	3684	4382	3800	4433	3235	4212	3779
	6	3231	2894	2960	2805	3375	3998	3461	3548	2977	3458	3271
	7	2537	2659	2725	2513	3088	3078	2653	3292	2725	2731	2800
	8	2359	2456	2425	2251	2458	2438	2374	2726	2501	2470	2446
	9	1984	2005	2224	2035	1921	1969	2132	2105	2295	2226	2090
	10	1685	1745	1831	1648	1635	1630	1649	1817	1949	1908	1750
	Final	1500	1500	1500	1500	1500	1500	1500	1500	1500	1500	1500

19.3 Satellite Dynamics 6 Degree of Freedom Simulation

19.3.1 Simulation Script File

```
%% EMA 569 Project - Thruster Simulation

clear; clc; close all;

%% Global Variables
th = pi/2;
th_by_2 = th/2;
% To rotate through 2 theta, aka 90 deg, burn thrusters for
   this long

global Ixx Iyy Izz Mx tx

% Intertias
Ixx = 30575; %lb-s^2-ft
Iyy = 30817; %lb-s^2-ft
Izz = 43490;

% Moments
Mx = 2*90*(5.79-3.1); %N-m %1.25 for spacecraft

tx = sqrt(th_by_2*2*Ixx/Mx); %s
%ty = sqrt(th_by_2*2*Iyy/Mx); %s

%% Initial Conditions
psi = 0;
psid = 0;
th = 0;
thd = 0;
phi = 0;
phid = 0; %rad/s

% Initial body fixed angular velocities (3-1-3)
w1 = psid*sin(th)*sin(phi)+thd*cos(phi);
w2 = psid*sin(th)*cos(phi)-thd*sin(phi);
w3 = phid+psid*cos(th);

% Initial quaternions
b0 = cos(th/2)*cos((phi+psi)/2);
b1 = sin(th/2)*cos((phi-psi)/2);
b2 = sin(th/2)*sin((phi-psi)/2);
b3 = cos(th/2)*sin((phi+psi)/2);

% Initial state vector for Euler Equations and Quaternions
```

```
x0q = [b0; b1; b2; b3; w1; w2; w3];

%% Differential Equation Solver

% Set ODE options and solve Euler and Quaternion systems
odeOpts = odeset('RelTol',1e-10,'AbsTol',1e-10,'MaxStep',1e-2);
[tq, solq] = ode45('eom_axisymmetric_sat_quaternions', [0,30],
   x0q, odeOpts);

%% Process Quaternion Solutions

% Check if quaternions squared sum to one
%test = solq(:,1)'.^2+solq(:,2)'.^2+solq(:,3)'.^2+solq(:,4)
   '.^2;

% Unpack quaternions as a function of time
b0t = solq(:,1);
b1t = solq(:,2);
b2t = solq(:,3);
b3t = solq(:,4);

% Iterate to solve rotation matrix for each time point
C_mat = zeros(3,3,length(tq));
psiq = zeros(1,length(tq));
thetaq = zeros(1,length(tq));
phiq = zeros(1,length(tq));

for i=1:length(tq)
    b0 = b0t(i); b1 = b1t(i); b2 = b2t(i); b3 = b3t(i);
    % Kammer 4.2.4
    C_mat(:,:,i) = [b0^2+b1^2-b2^2-b3^2, 2*(b1*b2+b0*b3), 2*(b1
       *b3-b0*b2);
        2*(b1*b2-b0*b3), b0^2-b1^2+b2^2-b3^2, 2*(b2*b3+b0*b1);
        2*(b1*b3+b0*b2), 2*(b2*b3-b0*b1), b0^2-b1^2-b2^2+b3^2];

    Ci = C_mat(:,:,i);

    % Angle recovery
    thetaq(i) = acos(Ci(3,3));
    psiq(i) = atan2(Ci(3,1), -Ci(3,2));
    phiq(i) = atan2(Ci(1,3),Ci(2,3));
end


%% 2B Quaternion Solution Plotting

% Quaternion
```

```
figure(1)
plot(tq, solq(:, 1),'r.-','displayname','\beta_0'); hold on;
plot(tq, solq(:, 2),'g.-','displayname','\beta_1'); hold on;
plot(tq, solq(:, 3),'b.-','displayname','\beta_2'); hold on;
plot(tq, solq(:, 4),'k.-','displayname','\beta_3'); hold off;
legend; grid on;
xlabel('Time (s)',"interpreter","latex");
ylabel('$$\beta$$',"interpreter","latex");
title('Quaternions vs. Time',"interpreter","latex");

% Angular velocity plot for quaternions
figure(2)
%colororder({'k','b'})
%yyaxis left
plot(tq, solq(:, 5)*30/pi,'r.-','displayname','\omega_x'); hold
    on;
plot(tq, solq(:, 6)*30/pi,'g.-','displayname','\omega_y'); hold
    on;
ylabel('Anglular Velocity ($$^\circ$$/s)',"interpreter","latex
   ");
%yyaxis right
plot(tq, solq(:, 7)*30/pi,'b.-','displayname','\omega_z'); hold
    off;
%ylim([0,60])
legend; grid on;
xlabel('Time (s)',"interpreter","latex");
%ylabel('Spin Anglular Velocity ($$^\circ$$/s)',"interpreter","
   latex");
title('\textbf{Quaternions}: Body Fixed Angular Velocity vs.
   Time',"interpreter","latex");

% Quaternion angle recovery
figure(3)
%colororder({'k','b'})
%yyaxis left
plot(tq, unwrap(thetaq)*180/pi,'r.-','displayname','\theta');
   hold on;
plot(tq, unwrap(psiq)*180/pi,'gx-','displayname','\psi'); hold
   on;
ylabel('Angle ($$^\circ$$)',"interpreter","latex");
%yyaxis right
plot(tq, unwrap(phiq)*180/pi,'b.-',"displayname", '\phi');
legend('location','best'); grid on;
xlabel('Time (s)',"interpreter","latex");
%ylabel('Spin Angle ($$^\circ$$)',"interpreter","latex");
title("\textbf{Quaternions}: Precession, Nutation, and Spin
   ($$\psi, \theta, \phi$$) vs. Time","interpreter","latex");
```

19.3.2 Equation of Motion Function File

```
function [dxdt] = eom_axisymmetric_sat_quaternions(t,x)

% Read global variables
global Ixx Iyy Izz Mx tx

% Unpack state vector
b0=x(1); b1=x(2); b2=x(3); b3=x(4); w1=x(5); w2=x(6); w3=x(7);

% Set inertia matrix
I = [Ixx 0 0; 0 Iyy 0; 0 0 Izz];

% Lecture 10 Slide 5
b = [(-w1*b1-w2*b2-w3*b3)/2;
    (w1*b0-w2*b3+w3*b2)/2;
    (w1*b3+w2*b0-w3*b1)/2;
    (-w1*b2+w2*b1+w3*b0)/2];

% Moment smooth ramp to Mx in one second
if t<=tx
    Momx=Mx;
end
if t>=tx
    Momx = -Mx;
end
if t>2*tx
    Momx = 0;
end


% Euler Equations solved for angular velocity
w = [(I(2,2)-I(3,3))*w2*w3/I(1,1)+Momx/I(1,1);
    (I(3,3)-I(1,1))*w3*w1/I(2,2)+0/I(2,2);
    (I(1,1)-I(2,2))*w1*w2/I(3,3)+0/I(3,3)];

% Pack output vector
dxdt = [b;w];

end
```

19.4 Arm Analysis Code - Constant Acceleration (MATLAB)

```
% Analysis Where Both Arms are moving at the same time (minimum
    torque
% required analysis).. Assumes constant acceleration.
close all;
clear;
m = 1.17*1.64;                % Mass in kg of each rod
L = 1.25;                     % Length of each rod
theta_dd = 0.003491;          % Angular acceleration in each rod
t = linspace(0,60,61);       % half the total time of rotation
Beta = 1/2*m*L^2;             % Beta constant
Iz = 1/3*m*L^2;               % mass moment constant
delta = Iz+1/4*m*L^2;         % delta constant
alpha = 2*Iz + 1.5*m*L^2;     % alpha constant

% For torque analysis at two joints
halftime = t(ceil(length(t)/2)) % Total time of acceleration
for i = 1:length(t)
    if(i <= ceil(length(t)/2))
        theta_dd_plot(i) = theta_dd; % For plotting purposes
        theta_d(i) = theta_dd*t(i);         % Angular velocity
           of each rod during acceleration
        theta(i) = 1/2*theta_dd*t(i).^2;  % Angle of rotation
        theta_2(i) = pi/2;  % Angle difference between the two
           rods
    else
        nt = t(i) - halftime; % New relative time of
           decelleration
        theta_dd_plot(i) = theta_dd; % For plotting purposes
        theta_d(i) = theta_dd*halftime-theta_dd*nt; % Angular
           velocity of each rod during deceleration
        theta(i) = 1/2*theta_dd*halftime.^2 - 1/2*theta_dd*nt
           .^2;  % Angle of rotation
        theta_2(i) = pi/2; % Angle difference between the two
           rods
    end
    % Equations related to torque at joint 1
    tau1Term = (alpha+2*Beta*cos(theta_2(i)))*theta_dd;  %
       first term for tau
    tau2Term = (delta+Beta*cos(theta_2(i)))*theta_dd;    % 2nd
       term in equation
    tau3Term = -1*Beta*sin(theta_2(i))*theta_d(i)*theta_d(i);
         % 3rd term in equation
    tau4Term = -1*Beta*sin(theta_2(i))*(theta_d(i)+theta_d(i))*
       theta_d(i); % fourth term in equation
    tau_1(i) = tau1Term + tau2Term +tau3Term + tau4Term; %
```

```
        Torque around joint 1

    % Equations related to torque at joint 2
    Twotau1Term = (delta + Beta*cos(theta_2(i)))*theta_dd; %
       first term for tau
    Twotau2Term = delta*theta_dd;                          % 2nd
       term for tau 2
    Twotau3Term = Beta*sin(theta_2(i))*theta_d(i)*theta_d(i);
         % 3rd term for tau 2
    tau_2(i) = Twotau1Term+Twotau2Term+Twotau3Term; % Torque
       around joint 1
end

figure(1)
plot(t,tau_1)
title('Torque Versus Time in Full Rotation At Joint 1 and 2', '
   Interpreter',...
    'latex');
xlabel("Time [s]")
ylabel("Torque Required [Nm]")

hold on
plot(t,tau_2)
legend('Joint 1', 'Joint 2','Interpreter'...
    ,'latex', 'fontsize', 14)
%ylim([0.01,0.05])
hold off
figure(3)
plot(t,theta)
title('Constant Angular Velocity Analysis - $\theta$, $\dot{\
   theta}$ and $\ddot{\theta}$ vs t'...
    , 'Interpreter', 'latex')
xlabel("Time [s]", 'FontSize', 14)
ylabel('\theta [rad]', 'FontSize', 14)

yyaxis right
hold on
plot(t,theta_d)
ylabel('$\dot{\theta} [\frac{rad}{s}]$  and  $\ddot{\theta} [\
   frac{rad}{s^2}]$'...
    , 'Interpreter', 'latex', 'fontsize', 14)
%ylim([0,0.15])
plot(t,theta_dd_plot)
legend({'$\theta$', '$\dot{\theta}$', '$\ddot{\theta}$'}, '
   Interpreter',...
    'latex', 'fontsize', 14);
```

19.5 Arm Analysis Code - Constant Torque (MATLAB)

```
% Analysis Where Both Arms are moving at the same time when the
    motor is
% applying a constant torque.
close all;
clear;
m = 1.17*1.640;                 % Mass in kg of each rod
L = 1.25;                       % Length of each rod
t = linspace(0,30,150);         % half the total time of rotation
dt = 30/length(t);              % Small timesteps used in analysis
% Following constants are used to simplify torque equations.
Beta = 1/2*m*L^2;               % Beta constant
Iz = 1/3*m*L^2;                 % mass moment constant
delta = Iz+1/4*m*L^2;           % delta constant
alpha = 2*Iz + 1.5*m*L^2;       % alpha constant
% To make these move *approximately* parallel if they start so
   you can
% actually use the values from the previous analysis!!! :)
%tau_1 = 0.15*1.640;
%tau_2 = 0.075*1.640;
tau_1 = 0.0444824;
tau_2 = 0.017441;
% For torque analysis at two joints
for i = 1:length(t)
    % Updating angles and angular velocity based on theta_dd.
    syms theta_dd_2 theta_dd_1
    if( i == 1)
        % The first timestep the angles and angular velocities
           are all
        % zero (unless the arms start angled apart! Then you
           need to
        % change these initial values of theta_a, theta_b).
            theta_a(i) = 0;
            theta_b(i) = 0;
            theta_d_a(i) = 0;
            theta_d_b(i) = 0;
            eqn_tau_2(i) = tau_2 == (alpha + 2*Beta)*theta_dd_1
                + delta*theta_dd_2;
        % Then, solve for the first angular accelerations.
           These equations
        % are slightly modified because all angular
           acceleration terms and
        % sin terms are equal to zero.
            theta_dd_b_temp(i) = solve(eqn_tau_2, theta_dd_2);
            eqn_tau_1(i) = tau_1 == (alpha+2*Beta*cos(theta_b(i
               )))*theta_dd_1...
```

```
            + (delta+Beta*cos(theta_b(i)))*theta_dd_2;
        % Because both equations rely on eachother, and matlab
           has no easy
        % way to automatically solve it we must substitute one
           equation
        % into the other.
            eqn_solve_tdd_1(i) = subs(eqn_tau_1(i), theta_dd_2,
                theta_dd_b_temp(i));
            theta_dd_a(i) = solve(eqn_solve_tdd_1(i) ,
               theta_dd_1);
            eqn_solve_tdd_2(i) = subs(eqn_tau_1(i),theta_dd_1,
               theta_dd_a(i));
            theta_dd_b(i) = solve(eqn_solve_tdd_2(i),
               theta_dd_2);
    else
        % With small timesteps, the change in angles and
           angular velocity
        % can be solved as an approximation of a finite sum
           instead of a
        % continuous solution, which would not be possible with
            the given
        % equations.
            theta_a(i) = theta_a(i-1) + theta_d_a(i-1)*dt;
            theta_b(i) = theta_b(i-1) + theta_d_b(i-1)*dt;
            theta_diff(i) = theta_b(i)-theta_a(i);
            theta_d_a(i) = theta_d_a(i-1)+theta_dd_a(i-1)*dt;
            theta_d_b(i) = theta_d_b(i-1)+theta_dd_b(i-1)*dt;
        % Again, because both equations rely on eachother, the
           solutions
        % must be solved by substitution.
            eqn_tau_2(i) = tau_2 == (delta + Beta*cos(
               theta_diff(i)))*theta_dd_1...
                + delta*theta_dd_2 + Beta*sin(theta_diff(i))*
                   theta_d_a(i)*theta_d_a(i);
        % Using tau_2 to solve theta_dd_2 in terms of
           theta_dd_1
            theta_dd_b_temp(i) = solve(eqn_tau_2(i),theta_dd_2)
               ;
            eqn_tau_1(i) = tau_1 == (alpha+2*Beta*cos(
               theta_diff(i)))*theta_dd_1...
                + (delta+Beta*cos(theta_diff(i)))*theta_dd_2...
                - Beta*sin(theta_diff(i))*theta_d_a(i)*
                   theta_d_b(i)...
                - Beta*sin(theta_diff(i))*(theta_d_a(i)+
                   theta_d_b(i))*theta_d_b(i);
        % Substituting theta_dd_2 in terms of theta_dd_1 to
           solve
```

```
        % for theta_dd_1 with equation for tau_1.
            eqn_solve_tdd_1(i) = subs(eqn_tau_1(i), theta_dd_2,
                theta_dd_b_temp(i));
            theta_dd_a(i) = solve(eqn_solve_tdd_1(i),theta_dd_1
               );
        % Substituting found value of theta_dd_1 to solve for
        % theta_dd_2.
            eqn_solve_tdd_2(i) = subs(eqn_tau_1(i),theta_dd_1,
               theta_dd_a(i));
            theta_dd_b(i) = solve(eqn_solve_tdd_2(i),
               theta_dd_2);
    end
end

figure(1)
plot(t,theta_a)
ylim([0,1.6])
title('Constant Torque Analysis $\theta$, $\dot{\theta}$ and $\
   ddot{\theta}$ for Joint 1 vs t'...
    , 'Interpreter', 'latex')
xlabel("Time [s]", 'FontSize', 14)
ylabel('\theta [rad]', 'FontSize', 14)

yyaxis right
hold on
plot(t,theta_d_a)
ylabel('$\dot{\theta} [\frac{rad}{s}]$  and  $\ddot{\theta} [\
   frac{rad}{s^2}]$'...
    , 'Interpreter', 'latex', 'fontsize', 14)
%ylim([0,0.4])
plot(t,theta_dd_a)
legend({'$\theta$', '$\dot{\theta}$', '$\ddot{\theta}$'}, '
   Interpreter', 'latex', 'fontsize', 14);
hold off
figure(2)
plot(t,theta_b)
title('Constant Torque Analysis -  $\theta$, $\dot{\theta}$ and
    $\ddot{\theta}$ for Joint 2 vs t'...
    , 'Interpreter', 'latex')
xlabel("Time [s]", 'FontSize', 14)
ylabel('\theta [rad]', 'FontSize', 14)

yyaxis right
hold on
plot(t,theta_d_b)
ylabel('$\dot{\theta} [\frac{rad}{s}]$  and  $\ddot{\theta} [\
   frac{rad}{s^2}]$'...
```

```
    , 'Interpreter', 'latex', 'fontsize', 14)
plot(t,theta_dd_b)
legend({'$\theta$', '$\dot{\theta}$', '$\ddot{\theta}$'}, '
   Interpreter', 'latex', 'fontsize', 14);
hold off
```

19.6 Plumbing Analysis Script (EES)

```
$Load Component Library
$Load Mechanical Design
$Load NASA

"Structural Analysis Final Plumbing"

"want P, T, m_dot, V"
T_atm=converttemp(C,K,10[C])

"state 1: before thruster"
P[1]=275 [psi]*convert(psi,Pa)
ISP_1=234 [s]
F_1=445 [N]
g_o=9.6 [m/s^2]
{avg of grav constant due to range of alt.}

ISP_1=F_1/(m_dot[1]*g_o)
"proved with sizing up a similar thruster,
and exprapolating thrust curve to match flow"

D_1=0.05[m]
A_thrust=pi*(D_1/2)^2
T[1]=T_atm   "found in NASA source: 19780016335"

rho[1]=1004.5 [kg/m^3]
{low compressibility factor, so density remains pretty
   consistent throughout}
{modeled as incompressible}

m_dot[1]=rho[1]*A_thrust*V[1]
L_thrust=4.5 [m]
mu_1=0.000913 [Pa*s]
Re[1]=rho[1]*V[1]*D_1/mu_1
ff_1=0.045   {from moody chart triple axis with rel rough}
RelRough_alum=0.002 [-]

K_branch_flow=k_tee_branched(RelRough_alum)
{Tee branching flow for connecting RCS and main thrust}

K_elbow=k_90deg_elbow(RelRough_alum)
fo=1 [-]
K_GV=k_gatevalve(RelRough_alum, fo)
K_sum1=6*K_elbow+3*K_branch_flow+K_GV
H_f[1]=ff_1*(L_thrust/D_1+K_sum1)*(V[1]^2/(2*g_o))     "Darcys
   Eqn"
```

```
del_P[1]=H_f[1]*g_o*rho[1]

"state 2: before RCS"
P[2]=235 [psi]*convert(psi,Pa)
ISP_2=232.1 [s]
F_2=90[N]

ISP_2=F_2/(m_dot[2]*g_o)
"update to interpolated value due to 2.204% discrepancy!"

D_1=D_2
T[2]=T[1]
rho[2]=1004.5 [kg/m^3]
m_dot[2]=rho[2]*A_thrust*V[2]
L_RCS=4[m]
mu_2=mu_1
Re[2]=rho[2]*V[2]*D_2/mu_2
ff_2=64/Re[2]   {Laminar flow eqn for friction factor}
K_sum2=2*K_elbow+4*K_branch_flow+4*K_GV
H_f[2]=ff_2*(L_RCS/D_2+K_sum2)*(V[2]^2/(2*g_o)) "Darcys Eqn"
del_P[2]=H_f[2]*g_o*rho[2]

"state 3: before 3-way connector"
T[3]=T[2]
P3_thrust=P[1]+del_P[1]
P3_RCS=P[2]+del_P[2]
P[3]=P3_thrust+P3_RCS
rho[3]=1004.5 [kg/m^3]
m_dot[3]=6*m_dot[1]+5*m_dot[2]
m_dot[3]=rho[3]*A_thrust*V[3]
L_b4_pump=0.5[m]
mu_3=mu_2
D_3=D_2
Re[3]=rho[3]*V[3]*D_3/mu_3

ff_3=0.02706 [-]
{from moody chart triple axis with rel rough}

K_RCS_thrust=k_tee_branched(RelRough_alum)
{joins RCS and main thrust piping before valve}

K_sum3=K_RCS_thrust
H_f[3]=ff_3*(L_b4_pump/D_3+K_sum3)*(V[3]^2/(2*g_o))
del_P[3]=H_f[3]*g_o*rho[3]

"state 4: after tank before T-joint"
T[4]=T[3]
```

```
P[4]=((P[6]+del_P[6])+(P[3]-del_P[3]))/2
rho[4]=1004.5 [kg/m^3]
mu_4=mu_3
D_4=D_3
A_4=(pi*(D_4/2)^2)
gamma=1.2 [-]  {ratio of c_v/c_p}
R=8.3144598 [J/(mol*K)]
MM_hyd=0.0320452 [kg/mol]
R_spec=R/MM_hyd
m_dot[4]=m_dot[3]+m_dot[6]
m_dot[4]=rho[4]*A_4*V[4]
L_tank_thrust=0.5[m]
Re[4]=rho[4]*V[4]*D_4/mu_4

ff_4=0.02396 [-]
{from moody chart triple axis with rel rough}
{used moody chart onlin calc}

K_tank_out=k_sudden_contraction(D_tank,D_4)
K_sum4=K_tank_out+K_GV
H_f[4]=ff_4*(K_sum4)*(V[4]^2/(2*g_o))
del_P[4]=H_f[4]*g_o*rho[4]

"Regulator from tank to state:4"
Q[4]=A_4*V[4]
C_v=1.84

Q_4_unitadjusted=Q[4]*2188.88
{units adjusted to SCFM for CV unit issue}

del_p_hyd_tank=P[5]-P[4]
del_p_hyd_adjusted=del_p_hyd_tank*convert(pa,psia)
sg_hy=0.82 [-]   {specific Gravity for Liquid Hydrazine}
C_v=Q_4_unitadjusted*sqrt(sg_hy/del_p_hyd_adjusted)

"state 5: in Tank"
T[5]=T_atm
Vol_tank=7.33 [m^3]
Ac_tank=Pi*(D_tank/2)^2
V[5]=0 [m/s]
D_tank=2[m]
m_h=7769 [kg]
rho[5]=m_h/Vol_tank

"state 6:point leading up to arm start from tank T-joint"
P[6]=P[7]+del_P[7]
D_6=D_3
```

```
A_6=Pi*(D_6/2)^2
T[6]=T[3]
rho[6]=1004.5 [kg/m^3]
m_dot[6]=m_dot[7]
m_dot[6]=rho[6]*A_6*V[6]
L_toarmstart=0.5[m]
mu_6=mu_3
Re[6]=rho[6]*V[6]*D_6/mu_6
ff_6=0.0316 [-]
H_f[6]=ff_6*(L_toarmstart/D_6)*(V[6]^2/(2*g_o))
del_P[6]=H_f[6]*g_o*rho[6]

"state 7: from pump to arm end, AKA at arm end"
P[7]=332.35 [psi]*convert(psi,Pa)
{low pressure MEOP value from RAFTI valve service guide}

D_7=D_1/4
A_7=Pi*(D_7/2)^2
T[7]=T_atm
rho[7]=1004.5 [kg/m^3]
m_dot[7]=0.10[kg/s]
{Value TBD for RAFTI valve service guide}

m_dot[7]=rho[7]*A_7*V[7]
L_arm=2.5[m]
mu_7=mu_2
Re[7]=rho[7]*V[7]*D_7/mu_7
ff_7=0.0262 [-]
K_armsqueeze=k_sudden_contraction(D_6,D_7)
K_sum7=3*K_elbow+K_armsqueeze
H_f[7]=ff_7*(L_arm/D_7+K_sum7)*(V[7]^2/(2*g_o))     "Darcys Eqn
   "
del_P[7]=H_f[7]*g_o*rho[7]

"state 8: press at He Pressurant tank"
T[8]=T[5]
T_press_adjust=converttemp(K,F,T[8])+460
{absolute temperature (Rankine), so convert to deg F add 460}

P_HEadjust=200[psi]*convert(psi,Pa)
P[8]=P[5]+P_HEadjust
P_press_adjust=P[8]*convert(pa,psia)
rho[8]=density(He,T=T[8],P=P[8])
Vol_press=2 [m^3]

m_p=(Vol_tank+Vol_press)*rho[8]
{mass of helium needed to fill tankS w/ needed pressure}
```

```
Q[8]=Q[4]
del_p_press_tank=P[8]-P[5]
sg_he=0.137 [-]   {specific gravity of Helium}
Q_8_unitadjusted=Q[8]*2188.88   {units adjusted to SCFM for CV
   unit issue}
del_p_adjusted=del_p_press_tank*convert(pa,psia)
C_v_p=Q_8_unitadjusted/(13.61*P_press_adjust*sqrt(1/(sg_he*
   T_press_adjust)))
$
```

	Re_i [-]	ρ_i [kg/m^3]	T_i [K]	V_i [m/s]	$del_{P,i}$ [Pa]	$H_{f,i}$ [m]	$\dot{m}_i$ [kg/s]	P_i [Pa]	Q_i [m^3/s]
1	5525	1005	283.2	0.1004	22.48	0.002332	0.1981	1.896E+06	
2	1127	1005	283.2	0.02048	1.05	0.0001089	0.04039	1.620E+06	
3	38784	1005	283.2	0.705	77.04	0.007989	1.391	3.516E+06	
4	41573	1005	283.2	0.7557	4.722	0.0004896	1.491	2.905E+06	0.001484
5		1060	283.2	0				2.922E+06	
6	2789	1005	283.2	0.0507	0.408	0.00004231	0.1	2.293E+06	
7	11157	1005	283.2	0.8112	1754	0.1819	0.1	2.291E+06	
8		7.313	283.2					4.301E+06	0.001484

Unit Settings: SI K Pa J mass rad

Ac_{tank} = 3.142 [m^2]
A_4 = 0.001963 [m^2]
A_6 = 0.001963 [m^2]
A_7 = 0.0001227 [m^2]
A_{thrust} = 0.001963 [m^2]
C_v = 1.84 [-]
$C_{v,p}$ = 0.003198 [-]
$del_{p,adjusted}$ = 200 [psia]
$del_{p,hyd,adjusted}$ = 2.555 [psia]
$del_{p,hyd,tank}$ = 17617 [Pa]
$del_{p,press,tank}$ = 1.379E+06 [Pa]
D_1 = 0.05 [m]
D_2 = 0.05 [m]
D_3 = 0.05 [m]
D_4 = 0.05 [m]
D_6 = 0.05 [m]
D_7 = 0.0125 [m]
D_{tank} = 2 [m]
ff_1 = 0.045 [-]
ff_2 = 0.05681 [-]
ff_3 = 0.02706 [-]
ff_4 = 0.02396 [-]
ff_6 = 0.0316 [-]
ff_7 = 0.0262 [-]
fo = 1 [-]
F_1 = 445 [N]
F_2 = 90 [N]
γ = 1.2 [-]
g_o = 9.6 [m/s^2]
ISP_1 = 234 [s]
ISP_2 = 232.1 [s]
$K_{armsqueeze}$ = 0.4688 [-]
$K_{branch,flow}$ = 1.405 [-]
K_{elbow} = 0.7024 [-]
K_{GV} = 0.1873 [-]
$K_{RCS,thrust}$ = 1.405 [-]
K_{sum1} = 8.616 [-]
K_{sum2} = 7.773 [-]
K_{sum3} = 1.405 [-]
K_{sum4} = 0.687 [-]
K_{sum7} = 2.576 [-]
$K_{tank,out}$ = 0.4997 [-]
L_{arm} = 2.5 [m]
$L_{b4,pump}$ = 0.5 [m]
L_{RCS} = 4 [m]
$L_{tank,thrust}$ = 0.5 [m]
L_{thrust} = 4.5 [m]
$L_{toarmstart}$ = 0.5 [m]
MM_{hyd} = 0.03205 [kg/mol]
μ_1 = 0.000913 [Pa*s]
μ_2 = 0.000913 [Pa*s]
μ_3 = 0.000913 [Pa*s]
μ_4 = 0.000913 [Pa*s]
μ_6 = 0.000913 [Pa*s]
μ_7 = 0.000913 [Pa*s]
m_h = 7769 [kg]
m_p = 68.23 [kg]
$P3_{RCS}$ = 1.620E+06 [Pa]
$P3_{thrust}$ = 1.896E+06 [Pa]
$P_{HEadjust}$ = 1.379E+06 [Pa]
$P_{press,adjust}$ = 623.9 [psia]
$Q_{4,unitadjusted}$ = 3.248 [SCFM]
$Q_{8,unitadjusted}$ = 3.248 [SCFM]
R = 8.314 [J/(mol*K)]
$RelRough_{alum}$ = 0.002 [-]
R_{spec} = 259.5 [J/(kg*K)]
sg_{he} = 0.137 [-]
sg_{hy} = 0.82 [-]
T_{atm} = 283.2 [K]
$T_{press,adjust}$ = 510 [R]
Vol_{press} = 2 [m^3]
Vol_{tank} = 7.33 [m^3]

20 References

[1] N. Scharping. "The Future of Satellites Lies in the Constellations." (2021), [Online]. Available: https://astronomy.com/news/2021/06/the-future-of-satellites-lies-in-giant-constellations.

[2] "All the Satellites in Space Could Crack Open the Ozone Layer." (2021), [Online]. Available: https://www.popularmechanics.com/space/satellites/a36651845/satellite-pollution-starlink-ozone/.

[3] "Air Pollution from Reentering Megaconstellation Satellites could cause Ozone Hole 2.0." (2021), [Online]. Available: https://www.space.com/starlink-satellite-reentry-ozone-depletion-atmosphere.

[4] Y. Borthomieu. "Satellite Lithium-Ion Batteries." (2014), [Online]. Available: https://www.sciencedirect.com/topics/engineering/low-earth-orbit#:~:text=Satellites%5C%20in%5C%20LEO%5C%20are%5C%20affected,or%5C%20space%5C%20observation%5C%20and%5C%20science.

[5] I. Orbit Fab. "Orbit Fab Products and Hardware." (2022), [Online]. Available: https://www.orbitfab.com/products.

[6] V. Tangermann, "NASA Awards SpaceX $53 Million for Orbital Starship Refueling Test," *The Byte*, 2020.

[7] "Starship User's Guide." (2020), [Online]. Available: https://www.spacex.com/media/starship_users_guide_v1.pdf.

[8] F. L. Whipple, "The Theory of Micro-Meteorites," *Harvard College Observatory*, 1951. [Online]. Available: https://www.pnas.org/doi/pdf/10.1073/pnas.37.1.19.

[9] J. Plante, "Environmental Conditions for Space Flight Hardware – a Survey," *NASA Electronic Parts and Packaging*, 2004.

[10] M. R. Nichols. "What Materials Keep Satellites Safe in Space?" (2019), [Online]. Available: https://www.realclearscience.com/articles/2019/09/23/what_materials_keep_satellites_safe_in_space.html#:~:text=Aluminum%5C%20or%5C%20Titanium%5C%3F,of%5C%20aluminum%5C%20and%5C%20its%5C%20alloys..

[11] S. Wiki. "Hydrazine." (2023), [Online]. Available: http://www.sciencemadness.org/smwiki/index.php/Hydrazine.

[12] "Orbital Propulsion Center: Hyrdazine Propellant Tanks." (2022), [Online]. Available: https://www.space-propulsion.com/spacecraft-propulsion/hydrazine-tanks/index.html.

[13] Dunmore. "Mulitlayer Insulation Films." (2023), [Online]. Available: https://www.dunmore.com/products/multi-layer-films.html?gclid=CjwKCAiArY2fBhB9%20EiwAWqHK6j17Ptq2bOpBoo0441E43Zq_CYxrC5wiH1lfs2DsSZnRqBK7WjthoJPoQAvD_BwE.

[14] C. Henry. "Companies are Flying Old Satellites Longer, Study Finds." (2020), [Online]. Available: https://spacenews.com/companies-are-flying-old-satellites-longer-study-finds/#:~:text=Geostationary%5C%20satellites%5C%20are%5C%20typically%5C%20designed,commercial%5C%20comsats%5C%20in%5C%20geostationary%5C%20orbit..

[15] "Where Do Old Satellites Go When They Die?" (2022), [Online]. Available: https://spaceplace.nasa.gov/spacecraft-graveyard/en/.

[16] I. Iridium NEXT. "Hydrazine – Toxic for Humans, but satellites love it." (2017), [Online]. Available: https://www.iridium.com/blog/hydrazine-toxic-for-humans-but-satellites-love-it/.

[17] "Hydrazine - Environmental Protection Agency." (2000), [Online]. Available: https://www.epa.gov/sites/default/files/2016-09/documents/hydrazine.pdf.

[18] G. T. Coll. "Nasa's Exploration and In-Space Services (NExIS) Division OSAM-1 Propellant Transfer Subsystem Progress 2020." (2020), [Online]. Available: https://ntrs.nasa.gov/citations/20205004116.

[19] S. D. Potter. "A Cryogenic Propellant Production Depot for Low Earth Orbit." (2001), [Online]. Available: https://ntrs.nasa.gov/citations/20010039031.

[20] B. F. Kutter. "A Practical, Affordable Cryogenic Propellant Depot Based on ULA's Flight Experience." (2008), [Online]. Available: https://ntrs.nasa.gov/citations/20130010201.

[21] Howard and Nguyen. "Magnetic Capture Docking Mechanism." (2010), [Online]. Available: https://ntrs.nasa.gov/citations/20110000805.

[22] J. Kahn. "Docking System for Spacecraft." (1988), [Online]. Available: https://ntrs.nasa.gov/citations/19900002482.

[23] J. Choy. "Astrodynamics Class Notes, EMA 550." (2021).

[24] J. E. Prussing, "A Simple Proof of the Global Optimality of the Hohmann Transfer," *Journal of Guidance, Control, and Dynamics*, vol. 15, no. 4, pp. 1037–1038, 1992.

[25] K. Oakes. "Making Satellites Safer: The Search for New Propellants." (2020), [Online]. Available: https://ec.europa.eu/research-and-innovation/en/horizon-magazine/making-satellites-safer-search-new-propellants#:~:text=The%5C%20current%5C%20standard%5C%20propellant%5C%20for%5C%20satellites%5C%20is%5C%20hydrazine%5C%2Dbased%5C%20fuel,kidneys%5C%20and%5C%20central%5C%20nervous%5C%20system..

[26] S. Caldwell. "3.0 Power - State of the Art of Small Spacecraft Technology." (2023), [Online]. Available: https://www.nasa.gov/smallsat-institute/sst-soa/power#_Toc118790664.

[27] P. Hill and C. Peterson, *Mechanics and Thermodynamics of Propulsion, 2nd Edition*. Pearson, 1962, ISBN: 9780201146592.

[28] "Falcon: Capabilities and Services." (2022), [Online]. Available: https://www.spacex.com/media/Capabilities&Services.pdf.

[29] "Falcon User's Guide." (2021), [Online]. Available: https://www.spacex.com/media/falcon-users-guide-2021-09.pdf.

[30] "Space Launch System Mission Planner's Guide." (2016), [Online]. Available: https://ntrs.nasa.gov/citations/20170005323.

[31] P. Rincon. "What is Elon Musk's Starship." (2020), [Online]. Available: https://www.bbc.com/news/science-environment-55564448.

[32] "ISS Main Systems," [Online]. Available: https://www.nasa.gov/pdf/167129main_Systems.pdf.

[33] G. D. Mauro. "General GNC System Architecture." (2017), [Online]. Available: https://www.researchgate.net/figure/General-GNC-system-architecture_fig6_321539579.

[34] "Satellite Component Catalog." (2023), [Online]. Available: https://www.satcatalog.com/.

[35] "Monopropellant Thrusters." (), [Online]. Available: https://satcatalog.s3.amazonaws.com/components/874/SatCatalog_-_Moog_-_MONARC-90LT_-_Datasheet.pdf?lastmod=20210710011332.

[36] C. P. Philip Hill, *Mechanics and Thermodynamics of Propulsion*.

[37] D. A. Fester. "Material compatability with space storable propellants." (1972), [Online]. Available: https://ntrs.nasa.gov/api/citations/19720019028/downloads/19720019028.pdf.

[38] "Ptd-222 monopropellant diaphram tank - cots." (), [Online]. Available: https://www.mt-aerospace.de/files/mta/tankkatalog/PTD-222.pdf.

[39] "Density, compressibility, thermal conductivity, and mechanical movement of solid hydrazine." (1976), [Online]. Available: https://apps.dtic.mil/sti/pdfs/ADA042039.pdf.

[40] A. M. S. Richard G. Budynas, *Rourke's Formulas for Stress and Strain*, Ninth. McGraw Hill, 2020, ISBN: 978-1-26-045376-8.

[41] "Thin-Walled Pressure Vessels." (), [Online]. Available: https://www.efunda.com/formulae/solid_mechanics/mat_mechanics/pressure_vessel.cfm.

[42] "Titanium ti-6al-4v (grade 5), sta." (), [Online]. Available: https://www.matweb.com/search/datasheet_print.aspx?matguid=b350a789eda946c6b86a3e4d3c577b39.

[43] "Space - propellant tanks." (), [Online]. Available: https://www.sbi.at/en/applications/aeronautics/space-fuel-tanks.

[44] "Control moment gyroscopes." (), [Online]. Available: https://storage.googleapis.com/blue-canyon-tech-news/1/2022/04/BCT_DataSheet_Components_ControlMomentGyroscope.pdf.

[45] "1N Monopropellant Hydrazine Thruster." (), [Online]. Available: https://satcatalog.s3.amazonaws.com/components/1355/SatCatalog_-_Rafael_-_1N_Monopropellant_Hydrazine_Thruster_-_Datasheet.pdf?lastmod=20221228054950.

[46] "Satellite frequency bands." (), [Online]. Available: https://www.esa.int/Applications/Telecommunications_Integrated_Applications/Satellite_frequency_bands.

[47] "Sagitta Star Tracker." (), [Online]. Available: https://www.satcatalog.com/component/sagitta-star-tracker/.

[48] S. Antunes. "DIY Satellite Platforms." (2011), [Online]. Available: https://www.oreilly.com/library/view/diy-satellite-platforms/9781449312756/ch01s05.html.

[49] L. Smith. "The ABCs of Multi-Layer Insulation for Spacecraft." (2019), [Online]. Available: https://www.designnews.com/materials-assembly/abcs-multi-layer-insulation-spacecraft.

[50] T. M. Technologies. "Standard Passive Orbital Thermal-control (SPOT) Structures." (2019), [Online]. Available: https://www.tmt-ipe.com/small-spacecraft-structures.

[51] E. K. Stansbery. "Hypervelocity impact technology." (2023), [Online]. Available: https://hvit.jsc.nasa.gov/shield-development/.

[52] E. L. C. Shannon Ryan Troy Hedman. "Honeycomb vs. Foam: Evaluating a Potential Upgrade to ISS Module Shielding for Micrometeoroids and Orbital Debris." (2009), [Online]. Available: https://ntrs.nasa.gov/api/citations/20100017497/downloads/20100017497.pdf.

[53] "ZTJ-Omega Solar Cell." (2019), [Online]. Available: https://www.rocketlabusa.com/assets/Uploads/RL-SolAero-Data-Sheet-ZTJ-Omega.pdf.

[54] "New solar cell is more efficient, costs less than its counterparts." (2016), [Online]. Available: https://energy.mit.edu/news/new-solar-cell-efficient-costs-less-counterparts/.

[55] "About Canadarm2." (2018), [Online]. Available: https://www.asc-csa.gc.ca/eng/iss/canadarm2/about.asp.

[56] "Canadarm2 and the Mobile Servicing System: Subsystems." (2013), [Online]. Available: https://www.nasa.gov/mission_pages/station/structure/elements/subsystems.html.

[57] M. M. Finckenor. "Materials for Spacecraft." (), [Online]. Available: https://ntrs.nasa.gov/api/citations/20160013391/downloads/20160013391.pdf.

[58] M. K. E. al. "New approach on robotic arm design: Fully modular arm architecture utilizing novel space interface." (), [Online]. Available: https://www.hou.usra.edu/meetings/isairas2020fullpapers/pdf/5059.pdf.

[59] A.-N. S. P. N. Koustoumpardis. "Dynamics and computed-torque control of a 2-dof manipulator: Mathematical analysis." (), [Online]. Available: https://hal.science/hal-03598924/document.

[60] ResearchGate. "5dof robot arm model." (), [Online]. Available: https://www.researchgate.net/figure/Five-degrees-of-freedom-robot-arm-model_fig2_319127421.

[61] P. Sracic, *EMA 542 - Advanced Dynamics Notes*.

[62] "Stepperonline high torque nema 23 cnc stepper motor 114mm 425oz.in/3nm cnc mill lathe router." (), [Online]. Available: https://www.amazon.com/Torque-Stepper-Motor-425oz-Router/dp/B00PNEPW4C/ref=asc_df_B00PNEPW4C/?tag=hyprod-20&linkCode=df0&hvadid=309793588525&hvpos=&hvnetw=g&hvrand=5071281253144135992&hvpone=&hvptwo=&hvqmt=&hvdev=c&hvdvcmdl=&hvlocint=&hvlocphy=9018948&hvtargid=pla-571641189318&psc=1&tag=&ref=&adgrpid=60862048759&hvpone=&hvptwo=&hvadid=309793588525&hvpos=&hvnetw=g&hvrand=5071281253144135992&hvqmt=&hvdev=c&hvdvcmdl=&hvlocint=&hvlocphy=9018948&hvtargid=pla-571641189318.

[63] T. B. I. Eugene Avallone, *Marks' Standard Handbook For Mechanical Engineers 10th Edition*.

[64] C. W. Aaron Deutschman Walter Michels, *Machine Design - Theory and Practice*.

[65] W. C. Young, *Rourke's Formulas for Stress and Strain*, Sixth. McGraw Hill, 1989, ISBN: 0-07-072541-1.

[66] "Nasa-std$_5$001b: Structural Design and Test Factors of Safety for Spaceflight Hardware," [Online]. Available: https://standards.nasa.gov/sites/default/files/standards/NASA/B-w/CHANGE-3/3/2022-10-24-NASA-STD-5001B-w-Change-3-Approved.pdf.

[67] N. M. S. F. Center. "Development of vibroacoustic and Shock Design and Test Criteria Standard." (), [Online]. Available: https://standards.nasa.gov/sites/default/files/standards/MSFC/B/0/msfc-std-3676b.pdf.

[68] D. C. Kammer, *EMA 642 - Satellite Dynamics Notes*.

[69] Neutrium. "Pressure loss from fittings - excess head (k) method." (), [Online]. Available: https://neutrium.net/fluid-flow/pressure-loss-from-fittings-excess-head-k-method/#:~:text=The%5C%20K%5C%2Dvalue%5C%20represents%5C%20the,conditions%5C%20(i.e.%5C%20Reynold%5C%20Number)..

[70] G. Sensors and Controls. "How to Calculate Flow Rate Through a Valve." (), [Online]. Available: https://www.gemssensors.com/resource-center/troubleshooting-technical-help/valve/how-to-calculate-flow-rate-through-valve.

[71] Swagelok. "Cv Calculator For Valve Sizing." (), [Online]. Available: https://www.swagelok.com/en/toolbox/cv-calculator.

[72] Swagelok. "Pressure Regulators RHPS Series." (), [Online]. Available: https://www.swagelok.com/downloads/webcatalogs/en/ms-02-430.pdf.

[73] N. Grumman. "Pressurant Tanks Data Sheets." (), [Online]. Available: https://www.northropgrumman.com/space/pressurant-tanks-data-sheets-sorted-by-volume/.

[74] H. Group. "Advantages of servo motors." (), [Online]. Available: https://www.heason.com/news-media/technical-blog-archive/advantages-of-servo-motors.

[75] M. Group. "Modular integrated robot joint high torque and low cogging for excellent performance." (), [Online]. Available: https://www.maxongroup.com/medias/sys_master/root/8841653288990/Brosch-Robot-Joint-0520.pdf.

[76] C. M. Group. "A guide to robot joint design." (), [Online]. Available: https://www.azorobotics.com/Article.aspx?ArticleID=237.

[77] J. L. Pieri. "An inside look at electromechanical power-off braking options." (), [Online]. Available: https://www.techbriefs.com/component/content/article/tb/supplements/mcat/features/articles/25417#:~:text=Spring%5C%20set%5C%20brakes%5C%20have%5C%20advantages%5C%20over%5C%20permanent%5C%20magnet,smaller%5C%20footprint%5C%2C%5C%20speed%5C%2C%5C%20or%5C%20rapid%5C%20cycling%5C%20is%5C%20needed..

[78] R. V. Dragone. "Choosing the right brake for robotic applications." (), [Online]. Available: https://www.techbriefs.com/component/content/article/tb/supplements/md/features/articles/28812.

[79] R. R. R. Jr. "Requirements For Threaded Fastening Systems In Spaceflight Hardware." (), [Online]. Available: https://standards.nasa.gov/sites/default/files/standards/NASA/B/0/2021-08-06-nasa-std-5020b_final.pdf.